

**Advanced Techniques for Single Molecule
Experiments and Their Applications**

by

Mehdi Yavuz Yüce

**A Thesis Submitted to the
Graduate School of Engineering
in Partial Fulfillment of the Requirements for
the Degree of**

**Doctor of Philosophy
in
Physics**

Koc University

September 2012

Koç University
Graduate School of Sciences and Engineering

This is to certify that I have examined this copy of a doctoral dissertation by

Mehdi Yavuz Yüce

and have found that it is complete and satisfactory in all respects,
and that any and all revisions required by the final
examining committee have been made.

Committee Members:

Assoc. Prof. Alper Kiraz (Advisor)

Prof. Adem Levent Demirel

Assoc. Prof. Özgür Esat Müstecaplıođlu

Assoc. Prof. Alper Tunga Erdođan

Assoc. Prof. Selçuk Aktürk

Date:

ABSTRACT

In this work, fluorescence properties and video-based tracking of single molecules were studied using time-resolved far field optical detection techniques.

A room temperature setup with both wide-field microscopy and sample-scanning confocal detection systems, and a cryostat setup for low temperature experiments were developed. The range of possible measurements includes time correlated single photon counting (TCSPC), fluorescence correlation spectroscopy (FCS), analysis of fluorescence spectra, and wide-field- and confocal microscopies. Proper operation of the setups was verified by sample data acquired from model systems. The room temperature setup was then put into use to address original topics.

As the first study, a well-known dye molecule terrylene was doped into a relatively unexplored host anthracene, and characterized using confocal detection techniques. Fluorescence lifetime, molecular orientation, detection rate at saturation, intersystem crossing rate, and photostability of terrylene were investigated on single molecule level. This dye-host combination was shown to be a promising sample for future room temperature single molecule experiments.

The second study was about single molecule tracking. A new imaging model was developed that takes into account the motion of a molecule during the exposure time of a frame. This extended imaging model better represented the actual data generation process and improved the accuracy of position estimates. It also allowed molecules' velocity to be estimated from an individual frame. The position and velocity data were further processed in a Kalman filter to recover the trajectory of a single molecule.

The last part of the thesis involved characterization of avalanche photodiode detectors (APD), which are commonly used in single molecule experiments. APDs with different brands and/or manufacturers were compared in terms of their dynamic range, dark count rate, linearity, and stability. Evaluation boards were used to study signal to noise ratio as functions of temperature and bias voltage.

ÖZET

Bu çalışmada, tek moleküllerin fulorasan özellikleri ve video-tabanlı izlenmesi zaman çözünürlüklü uzak alan optik algılama teknikleri kullanılarak incelenmiştir.

Geniş alan mikroskopisi ve örnek taramalı eşodaklı agılama yapılabilen bir oda sıcaklığı düzeneği ile düşük sıcaklık deneyleri için düşünülmüş bir kriyostat düzeneği geliştirilmiştir. Mümkün olan ölçümler arasında zaman bilgili tek foton sayımı (TCSPC), fulorasan korelasyon spektroskopisi (FCS), fulorasan tayfların analizi, ve geniş alan- ve eşodaklı mikroskopileri yer almaktadır. Düzeneklerin doğru çalıştığı model sistemlerden alınan örnek verilerle doğrulanmıştır. Sonrasında, oda sıcaklığı düzeneği orjinal araştırma konuları için kullanılmıştır.

İlk çalışma olarak iyi bilinen bir boya molekülü olan terilen nispeten az çalışılmış bir matris olan antrasin içine katılanmış, ve eşodaklı agılama teknikleri kullanılarak karakterize edilmiştir. Terilenin fulorasan ömür süresi, moleküler yönelim, doyunluk algılama hızı, sistem arası geçiş hızı, ve fotostabilite özellikleri tek molekül düzeyinde incelenmiştir. Bu boya-matris eşlemesinin gelecekteki oda sıcaklığı tek molekül deneyleri için ümit verici bir örnek olduğu gösterilmiştir.

İkinci çalışma tek molekül izlemeyle ilgili olmuştur. Molekülün bir kare zamanı içindeki hareketini dikkate alan yeni bir görüntüleme modeli geliştirilmiştir. Bu genişletilmiş model gerçek veri oluşma işlemini daha iyi temsil etmiş, ve konum tahminlerinin doğruluğunu iyileştirmiştir. Bu model aynı zamanda moleküllerin hızlarının tek bir kareden tahmin edilebilmesini de mümkün kılmıştır. Konum ve hız verileri daha sonra bir Kalman filtresinde işlenerek molekülün izlediği yol çıkarılmıştır.

Tezin son bölümü tek molekül deneylerinde sıklıkla kullanılan çığ fotodiyot algılayıcıların (APD) karakterizasyonunu içermiştir. Değişik marka ve/veya modellerdeki APDler dinamik aralık, karanlık sayı, doğrusallık, ve kararlılık yönünden karşılaştırılmıştır. Model devreler kullanılarak sinyal gürültü oranının sıcaklık ve ters gerilime bağlı değişimi incelenmiştir.

ACKNOWLEDGEMENTS

I would like to express my gratitude to Professor Kiraz for his guidance throughout this study, his honesty, and the comfortable working environment he has provided to me. With separation imminent, I wish him a peaceful life.

I would also like to thank my thesis monitoring committee members Professor Demirel and Professor Müstecaplıođlu, and my thesis defense committee members Professor Erdoğan and Professor Aktürk for the time they spent during evaluating my progress and thesis.

My sincere thanks are extended to past and present friends, colleagues, and staff at Koç University, whose names I list alphabetically: M. Aas, R. Asif, N. Atađ, C. Aydođmuş, A. Baş, E. Beyatlı, S. Çakmak, H. Çankaya, M. Eryürek, U. S. Gökay, M. Güler, M. Gündođan, A. Jonas, Y. Karadađ, İ. Karakaş, B. Kaya, A. Kurt, İ. Küçükkara, M. Mestre, F. Solđun, N. Taşaltın, Y. Uysallı, N. Vardar, N. Yılmaz, H. Yılmaz, H. Yılmaz, İ. Yorulmaz, and M. Yorulmaz. I apologize in advance to those whose names were forgotten in this list.

I also thank F. Hacızade, A. Hasekiođlu, and M. A. Can from TÜBİTAK BİLGEM for their collaboration. Their continued interest has been a source of motivation for me.

This work was partially supported by the Ministry of Development under Grant No. 2009K120200, and TÜBİTAK Ph.D. scholarship BİDEB-2211.

TABLE OF CONTENTS

List of Tables	viii
List of Figures	ix
Nomenclature	xiv
Chapter 1: Introduction	1
1.1 Overview	1
1.2 Transitions in a Molecule	3
1.3 Single Emitters	7
Chapter 2: Realization of Single Molecule Experiments	11
2.1 Introduction	11
2.2 Room Temperature Setup	13
2.3 Programming Tasks for Confocal Detection	16
2.3.1 Imaging	17
2.3.2 Time Trace Recording	19
2.3.3 Coincidence Counting	24
2.3.4 FCS	28
2.4 Cryostat Setup	33
2.5 Conclusion	37
Chapter 3: Terrylene – Anthracene as a New Dye – Host System	48
3.1 Introduction	48
3.2 Experimental	49
3.3 Results and Discussion	50

3.4	Conclusion	56
Chapter 4:	Single Molecule Tracking Based on a New Imaging Model	62
4.1	Introduction	62
4.2	Imaging Model	63
4.3	Algorithm	64
4.3.1	Maximum Likelihood Approach for In-frame Parameter Estimation	65
4.3.2	Kalman Filtering for Tracking	71
4.4	Testing the Algorithm	73
4.4.1	Generating Simulated Images	73
4.4.2	Piezo Stage Experiments	74
4.4.3	Results and Discussions	75
4.5	Conclusion	81
Chapter 5:	Characterization of APD Detectors	88
5.1	Introduction	88
5.2	Experimental	90
5.3	Dynamic Range	91
5.4	Stability	92
5.5	Effects of Temperature and Bias Voltage on Detection Rate	93
5.6	SNR in Detection with APDs	95
5.7	Conclusion	97
Chapter 6:	Conclusion	104
Appendix A:	User's Manual for the Confocal Setup Software	107
Appendix B:	Derivatives of the Log-Likelihood Function	143
Bibliography		147

LIST OF TABLES

Table 1.1:	Typical timescales of transitions in a fluorescent dye molecule. . . .	5
Table 2.1:	Comparison of synchronous and asynchronous acquisition modes. . .	23
Table 2.2:	Results obtained from fitting eq. (2.2) to the TAC histograms in Figure 2.7.	27
Table 2.3:	Results obtained from fitting eq. (2.5) to the FCS curve in Figure 2.9.b.	32
Table 2.4:	Structure and relevant physical properties of common matrices used in low temperature single molecule experiments [86].	36
Table 4.1:	Parameters of the described imaging model and their units in the sample and image spaces.	64
Table 5.1:	APDs used in measurements, and some of their properties.	90
Table 5.2:	Comparison of the characterized APDs and the analog photodiode in terms of their dark counts, dynamic range and linearity.	91
Table 5.3:	Noise present in detection rates of IDQ-D2 diode at different temperatures, and PE-1 APD at its fixed operation conditions. Measurement time was 12 minutes for all cases.	96

LIST OF FIGURES

Figure 1.1:	Jablonski diagram showing molecular energy levels and transitions between them. Approximate timescales for these transitions are given in Table 1.1.	10
Figure 1.2:	Schematic drawing showing how the zero phonon transition and the phonon side band would appear in a fluorescence spectrum (height and width of the peaks are not drawn to scale).	10
Figure 2.1:	General overview of the room temperature setup.	38
Figure 2.2:	Schematic drawing showing components in the room temperature setup (BP: band pass filter; NF: notch filter; PH: pinhole; SP: short pass filter; BS: beamsplitter). BP 605/90 and NF 532 are used interchangeably between wide-field and confocal detection parts.	38
Figure 2.3:	Wide field images of terrylene-doped p-terphenyl crystals taken under parallel- (a), and TIRF excitations (b). The vertical orientation of terrylene molecules to the substrate plane (parallel to the optical axis) prevents their excitation in (a), and makes them appear as doughnut shapes in (b).	39
Figure 2.4:	Hardware connections for the confocal detection part of the room temperature setup. APDs can be connected either to the card or the TAC (indicated by dashed lines).	39
Figure 2.5:	(a) Confocal image of DBT crystals on coverglass, recorded from a $15\mu\text{m}\times 15\mu\text{m}$ area with 300×300 pixels, and $0.5\text{ms}/\text{pixel}$ integration time. Colorbar indicates photons detected per pixel. (b) Detail cropped and rotated from a wide-field image, showing the same region as in (a).	40
Figure 2.6:	Fluorescence time trace of a single terrylene molecule in PMMA that exhibits blinking at $t \approx 19\text{s}$, and photobleaches at $t \approx 26\text{s}$	41
Figure 2.7:	Representative TAC histograms recorded from single terrylene molecules in p-terphenyl. Blue line is a fit according to the exponential rise function of eq. (2.2) (see Table 2.2). The FSTL,	

	acquisition time, and TAC rate were 100ns, 183.4s, and 382.2 Hz for the measurement of (a), and 200ns, 302.1s and 594.5Hz for that of (b).	42
Figure 2.8:	(a) TAC histogram showing the pulses of the subpicosecond Toptica laser. 80MHz repetition rate of the laser appear as 12.5ns separation between histogram peaks. The histogram was plotted with 500 bins. (b) One of the peaks in (a) fitted with a Lorentzian function reveals the IRF as 555ps. TAC rate was 344Hz; APD rates were 79.7 and 50.4kHz; acquisition time was 104s.	43
Figure 2.9:	(a) 1s section from a 120s-long FCS time trace, recorded from a 0.1nM Rhodamine B solution in water. Passing of molecules through the confocal probe volume appear as spikes in the time trace. The typical width of the spikes is expressed by τ_D of eq. (2.5). (b) $g^{(2)}(\tau)$ (blue line) calculated from the time trace in (a), and a fit according to eq. (2.5) (green line). Owing to asynchronous acquisition, the analysis can address events occurring on a wide timescale starting from 10ns.	44
Figure 2.10:	(a) Chamber built for FCS analysis of dye molecules in organic solvents. The upper half of a cut vial and a standard glass coverslip are fused together by water glass. (b) FCS curve (blue line) from dilute terrylene in toluene solution. Time trace was recorded with a 1.49 NA oil objective, 2-3 μ m above the coverslip. Acquisition time was 120s, with APD rates 10.26kHz and 10.80kHz. The same fitting procedure as in Figure 2.9.b yields $T = 0.14$, $\tau_T = 80$ ns, $A = 1.00$, $\tau_D = 32.9\mu$ s, $\kappa = 5.22$, and $g_\infty = 1.00$	45
Figure 2.11:	Schematic drawing of the cryostat setup.	46
Figure 2.12:	A photograph from inside the sample chamber showing copper wire connections.	47
Figure 2.13:	Low temperature fluorescence spectrum of dilute terrylene molecules embedded in p-terphenyl, recorded at 6K.	48
Figure 3.1:	Confocal image of individual terrylene molecules in anthracene, recorded from a 4 μ m \times 4 μ m area with 100 \times 100 pixels, and 1ms/pixel integration time. Excitation power was 10 μ W. Inset shows the intensity profile (black squares) taken along the center of the upper left molecule, and a Gaussian fit (blue line) to it. Width of the Gaussian function is 223nm, in agreement with the	

	diffraction limited resolution. The colorbar designates the number of photons detected per pixel.	57
Figure 3.2:	(a) Fluorescence spectrum recorded from one of the bright features (marked by C) in the confocal image of Figure 3.1. (b) TAC histogram (red diamonds) recorded from the same position, and fitted with the exponential model described in the text (blue line). TAC rate was 537Hz.	58
Figure 3.3:	TAC histogram (red diamonds) recorded from a single terrylene molecule, fitted with the model of eq. (2.2) to yield $\tau_F = 2.8\text{ns}$ (blue line). TAC rate and acquisition time were 3228Hz, and 63s respectively.	59
Figure 3.4:	Detection rate as a function of the polarizer angle, recorded from a single Terrylene molecule (trace A; red), and an empty position within the anthracene crystal (trace B; green). The high modulation depth is an indicative of the parallel orientation of the transition dipole moment with respect to the substrate plane. Excitation power was $55\mu\text{W}$ for both measurements. Integration time of the original intensity versus time data was 10ms.	59
Figure 3.5:	Detection rates for the fluorescence of a single terrylene molecule (red squares) and the background (green circles) plotted as a function of the excitation power. The fluorescence signal is fitted to a standard saturation model to yield a detection rate at saturation of $S_\infty = 754\text{kHz}$ (blue line).	60
Figure 3.6:	Intensity autocorrelation function of a single terrylene molecule (red diamonds), fitted by an exponential decay function (blue line). Excitation power was $10\mu\text{W}$, corresponding to a total count rate of 137kHz on the APD's. A TAC histogram recorded from the same molecule is shown in the inset.	60
Figure 3.7:	Probability distribution of the number of photons detected before photobleaching, obtained from a set of 104 single molecule measurements (red squares), and fitted to a tri-exponential decay function (blue line). Excitation power was $19\mu\text{W}$	61
Figure 4.1:	Description of the assumed image formation model.	82
Figure 4.2:	Performance of the proposed estimation algorithm as a function of T for parameters v_x (green triangles), x_θ (blue squares), and x_c (red	

	circles). Tracking performance is evaluated on the basis of (a) CRLB limits, (b,c) bias and standard deviation of estimates from simulated images. For comparison, corresponding characteristics of x_m obtained from same set of simulated images are also shown (black diamonds). For all presented data, v_x is kept fixed at $3.11\mu\text{m/s}$ (7pixel/frame at $T=0.2\text{s}$).	83
Figure 4.3:	Performance of the proposed estimation algorithm as a function of v_x for parameters v_x (green triangles), and x_c (red circles), based on their (a) CRLB limits, (b,c) bias and standard deviation of estimates from simulated images. For comparison, corresponding characteristics of x_m obtained from same set of simulated images are also shown (black diamonds). T is kept fixed at 50ms for all presented data.	84
Figure 4.4:	A representative result from the piezo-stage experiments, showing (a) the overall linear trajectory, (b) the measurement error, and (c) v_x data for the actual (red line), measured (green pluses), and Kalman-filtered (blue circles) values.	85
Figure 4.5:	Result from the piezo-stage experiments with accelerated motion, showing (a) the overall sinusoidal trajectory, (b) the measurement error, and (c) v_y data for the actual (red line), measured (green pluses), and Kalman-filtered (blue circles) values.	86
Figure 4.6:	Two 15×15 pixel images of the molecule tracked in Figure 4.5, corresponding to representative maximum-velocity (left), and maximum-acceleration (right) instants that occurred at 19 th , and 25 th frames respectively.	87
Figure 5.1:	Detection rate as a function of normalized laser intensity for PE-1 APD. The green line is a fit to data points having count rates from 10^2 to 10^6 Hz. The graph reveals dynamic range, linearity, and dark counts of the APD. Each datapoint is obtained from a 20-s long measurement.	98
Figure 5.2:	Comparison of IDQ-20 and PE-1 APDs for stability.	98
Figure 5.3:	Comparison of (a) IDQ-20 and (b) PE-1 APDs for stability. Laser intensity was adjusted to yield similar count rates at both APDs.	99
Figure 5.4:	Detection rate as a function of bias voltage for IDQ-D1. Set temperature was at $\text{FB}+ = 560\text{mV}$, but discovered to have no effect	

	on the actual temperature (FB- fixed at $\approx 1500\text{mV}$).	100
Figure 5.5:	Detection rate as a function of bias voltage for IDQ-D2. Diode temperature was constant at $\text{FB-} = 501.98\text{mV}$. For all laser intensities, detection rate becomes 0 at $V_{\text{op}} = -22.6\text{V}$. The datapoints with 0 detection rate could not be shown due to logarithmic y-axis. Each datapoint is obtained from a 120s-long measurement.	100
Figure 5.6:	Dark count rate as a function of temperature for IDQ-D2. Bias voltage was constant at $V_{\text{op}} = -25.3\text{V}$.	101
Figure 5.7:	Detection rate as a function of temperature for IDQ-D2. Bias voltage was constant at $V_{\text{op}} = -25.3\text{V}$. Each datapoint is obtained from a 120s-long measurement.	101
Figure 5.8:	SNR as a function of detection rate for (a) IDQ-20, and (b) PE-1 APDs.	102
Figure 5.9:	SNR as a function of detection rate for IDQ-D2 APD operated with different bias voltages.	103
Figure 5.10:	SNR as a function of detection rate for IDQ-D2 APD operated with different diode temperatures. Bias voltage was constant at $V_{\text{op}} = -25.3\text{V}$.	103

NOMENCLATURE

ZPT	Zero phonon transition.
PSB	Phonon side band.
SNR	Signal to noise ratio.
TIRF	Total internal reflection.
NA	Numerical aperture.
PALM	Photo-activated localization microscopy.
STORM	Stochastic optical reconstruction microscopy.
APD	Avalanche photodiode detector.
TAC	Time to amplitude converter.
PMMA	Poly (methyl methacrylate).
FCS	Fluorescence correlation spectroscopy.
DBT	7,8,15,16-dibenzoterrylene.
IRF	Instrument response function.
FSTL	Full-scale time limit.
τ_F	Fluorescence lifetime.
τ	Delay time.
$g^{(2)}(\tau)$	Normalized intensity autocorrelation function.
PVA	Poly (vinyl alcohol).
FWHM	Full width at half maximum.
SMT	Single molecule tracking.
MLE	Maximum likelihood estimator/estimation.
T	Exposure time.
(x_0, y_0)	Initial position of a moving molecule.
(x_c, y_c)	Mid-frame-time position of a moving molecule.
(v_x, v_y)	Velocity components of a moving molecule.

λ_0	Rate of the Poisson process that models photon emission from a molecule.
λ_{bg}	Rate of the Poisson process that models photon emission from background.
$g(x,y)$	Point spread function.
L	Log-likelihood function.
$\hat{}$	Estimator, or a particular estimate.
CRLB	Cramer Rao lower bound.
FIM	Fisher Information Matrix.
\mathbf{x}	State vector for Kalman filter.
\mathbf{y}	Measurement vector for Kalman filter.
Q	Process noise covariance matrix.
R	Measurement error covariance matrix.

Chapter 1

INTRODUCTION

1.1 Overview

There are several techniques that offer sensitivity on the single molecule level¹. The experiments in this thesis are about a subset of these techniques that can be summarized as far field optical detection of fluorescent dye molecules. Other techniques capable of detecting, analyzing, and in some cases even manipulating individual molecules include scanning tunneling microscopy [1-3], atomic force microscopy [4,5], scanning near field optical microscopy [6-8], and surface enhanced raman scattering [9,10]. These go beyond the scope of this thesis and will not be mentioned in any further discussions.

The relevant part, i.e. far field optical detection of fluorescent dye molecules, attracts attention from various areas of research, owing to its high temporal resolution, and in situ application. On the fundamental science side, it offers the opportunity to observe numerous quantum optical effects; whereas on more applied areas such as materials science or molecular biology, it is used as a tool to reveal distinctions among an ensemble of molecules. While these applications are all very interesting topics on their own, they are unfortunately too diverse to be addressed in one doctoral study.

The main workload of the present thesis was about developing the necessary infrastructure for these experiments. Two original applications pertaining to quantum optical demonstrations and video-based tracking of single molecules were also accomplished along the way. These will be covered according to the following outline:

¹ The term “single molecule” used here refers to molecules that are at most a few nanometers in size. The formal definition of the word molecule otherwise puts no restriction on size.

Focusing on quantum optical effects, Chapter 1 first provides some background information about fluorescence and other competing transitions in a molecule. It then gives a brief comparison of single molecules to other systems that also show similar non-classical behavior. This comparison reveals advantages of single molecules in terms of performance and experimental convenience.

Chapter 2 discusses how single molecule experiments are realized in practice, explains the setups along with related programming tasks, and provides sample data acquired with them. These include a room temperature setup for both wide field imaging and confocal detection, and a cryostat setup for low temperature experiments. Unlike well established spectroscopic techniques, where turn-key commercial systems are readily available, single molecule experiments are usually done using custom built setups that have their unique problems and solutions. Technical details of these setups will thus be beneficial for future users or developers.

Chapter 3 presents a nice application of the room temperature confocal detection techniques, to characterize photo-physical properties of a well-known dye molecule terrylene in a new host matrix anthracene. This dye-host combination has not been explored at room temperature before. As will be discussed in more detail in Sections 1.3 and 3.1, single molecules are doped into solid hosts when used as model systems for studying quantum optical effects. The resulting properties such as fluorescence lifetime, molecular orientation, saturated emission rate, or photostability of the dye molecule are largely influenced by the host, and there are only few dye-host pairs that offer desirable properties. The results of Chapter 3 are therefore quite valuable in that they point out terrylene-anthracene as a promising dye-host pair for future single molecule experiments at room temperature. The higher conductivity of anthracene as compared to other host matrices makes this system even more attractive.

Chapter 4 presents another original application that uses the wide-field detection part of the room temperature setup. This study proposes a new data processing algorithm to improve accuracy of single molecule trajectories obtained from video microscopy. This analysis (i.e. extracting single molecule trajectories from recorded movies), known as

single molecule tracking (SMT), used to be carried with algorithms inherited from the similar analysis of particle tracking, where one recovers trajectories of fluorescent beads. While the two analyses share a lot in common, there are also some important distinctions originating from faster motion (due to smaller size) and limited fluorescence of a molecule. These differences result in the molecule traveling considerably within a frame's acquisition time that is long enough to acquire sufficient signal. Since particles move slower than molecules and provide much higher signal, the in-frame motion has never been considered in their tracking. The proposed algorithm for the first time incorporates the in-frame motion into the analysis to achieve a more realistic data generation model and hence a better accuracy of the resulting trajectories. Tests by simulations and model experiments with a piezo stage confirm significant improvement over traditional tracking algorithms that ignore in-frame motion.

Chapter 5 deals with avalanche photodiode detectors (APD), a type of semiconductor devices used in single molecule detection. Noise levels of several different APDs are characterized. This provides the opportunity to distinguish between different sources of noise and how they are affected by experimental conditions. Such insight about noise becomes important when working with low signal levels as in single molecule detection.

Finally, Chapter 6 concludes the thesis by summarizing the original contributions of this research.

1.2 Transitions in a Molecule

The absorption and emission of photons by a molecule are most conveniently explained over a schematic representation of the energy levels of the molecule, known as the Jablonski diagram [11]. The total energy of a molecule is made up of electronic, vibrational, and rotational contributions, resulting in a complicated energy level diagram. The energy difference between two adjacent electronic states is much greater than those of the vibrational or rotational ones. In the Jablonski diagram shown in Figure 1.1, the dark horizontal lines represent the energies that the molecule would have at the lowest-energy vibrational state of its various electronic states. Similarly, light horizontal lines show the

energies corresponding to various vibrational states of a particular electronic state. At ambient conditions, molecules are predominantly found in the lowest vibrational level of their ground electronic state (S_0). Upon absorbing a photon, a molecule undergoes an electronic transition from its ground state S_0 to a vibrational level of the upper excited electronic states (for example S_1 or S_2). The upper electronic states can be either a singlet or a triplet state, depending on the spins of the electrons. Direct excitation of the molecule from S_0 to triplet states is highly improbable. Therefore absorption involves only transitions from S_0 to upper singlet electronic states. These transitions take place in an extremely short time, on the order of a femtosecond. Following absorption, the molecule relaxes to the lowest vibrational level of the excited electronic state through a process known as vibrational relaxation. If the excited electronic state is above S_1 , transitions termed internal conversions accompany vibrational relaxations, until the molecule dissipates all of its excess energy and settles at the lowest vibrational state of S_1 . Both vibrational relaxation and internal conversion occur in around 1 picosecond, and nonradiatively. The molecule spends a relatively longer time of about few nanoseconds at the lowest vibrational state of S_1 , and this is followed by transitions back to the vibrational levels of S_0 either radiatively or nonradiatively. The radiative transitions from the lowest vibrational state of S_1 to various vibrational states of S_0 are termed fluorescence, and the time elapsed between absorption and emission of a photon is termed fluorescence lifetime. Since vibrational relaxations and internal conversions occur in only picoseconds, fluorescence lifetime is essentially the time spent at the lowest vibrational state of S_1 . Owing to the same reason, fluorescence always starts from the lowest vibrational state of S_1 , irrespective of where the molecule was excited initially. This makes fluorescence spectrum independent of the excitation wavelength. In addition to fluorescence, there are also nonradiative transitions from the lowest vibrational state of S_1 to vibrational states of S_0 . These are termed either as internal or external conversions, based on whether the decay process occurs over the own energy levels of the molecule (internal conversion), or also involves those of surrounding solute/host molecules (external conversion). For both cases, the transition occurs between states of the same spin multiplicity (singlet to singlet or

triplet to triplet). While there is no doubt about the existence of such nonradiative transitions, the actual mechanisms are not well understood. The important point here is that these nonradiative transitions also start from S_1 , and therefore can be regarded as processes competing against fluorescence. There is yet another type of nonradiative transition called intersystem crossing. It occurs between states of different spin multiplicity, and becomes more probable when their vibrational levels overlap. It is most commonly observed between S_1 and T_1 states, again competing with fluorescence. The radiative decay from T_1 to S_0 is called phosphorescence. Due to the low probability of a transition from T_1 to S_0 , phosphorescence lifetime is much higher than that of fluorescence (from 0.1ms to 10s). The typical times for transitions in a molecule are summarized in Table 1.1.

Transition	Typical time
Absorption	fs
Vibrational relaxation	ps
Internal conversion	ps
Fluorescence	ns
Intersystem crossing	μ s
Phosphorescence	ms

Table 1.1: Typical timescales of transitions in a fluorescent dye molecule.

As mentioned above, fluorescence occurs from the lowest vibrational state of S_1 to various vibrational states of S_0 . To which vibrational state of S_0 it will occur, is determined by the temperature of the surrounding medium (solute liquid or host crystal). At room temperature, the probability that the molecule fluoresces down to the lowest vibrational level of S_0 is negligible. It eventually settles at this level, but as a result of successive vibrational relaxations (not directly by fluorescence). On the other hand, as the temperature of the surrounding medium decreases, the probability of fluorescence to the lowest vibrational level of S_0 increases. This transition between the lowest vibrational levels of S_1 and S_0 is called zero phonon transition (ZPT), owing to the reason that it involves no vibrational relaxation afterwards (i.e. no coupling to phonons of the surrounding medium). It corresponds to the shortest wavelength in the fluorescence

spectrum. By the same token, the longer-wavelength emissions that correspond to transitions from the lowest vibrational state of S_1 to higher vibrational states of S_0 are called phonon side band (PSB).

The ZPT and the PSB would appear in the fluorescence spectrum as schematically shown in Figure 1.2. The peak corresponding to ZPT becomes narrower and more intense with decreasing temperature. Depending on the surrounding medium, this trend may reach to a Fourier transform limited case, where the linewidth of the ZPT becomes equal (within a proportionality constant) to the reciprocal of the fluorescence lifetime. This is a fundamental limit imposed by the energy – time uncertainty principle of quantum mechanics. After reaching this limit, the ZPT linewidth no longer narrows by decreasing temperature. This phenomenon has been observed for dye molecules embedded in a molecular crystal, at temperatures $\leq 4\text{K}$ [12-14]. The typical transform limited ZPT linewidths in these studies were $\Delta\nu \approx 10\text{MHz}$, which at an emission center of $\lambda_0 \approx 600\text{nm}$, corresponds to $\Delta\lambda \approx 1.2 \times 10^{-13}\text{m}$.

The lineshape of the ZPT can be determined with sufficient resolution. This is done by illuminating the molecule with a narrow linewidth ($\sim 100\text{kHz}$; narrower than the ZPT) tunable laser, making a frequency scan over a range where the ZPT is expected, and detecting fluorescence intensity at the PSB region as a function of excitation frequency [12-17]. The resulting fluorescence intensity versus excitation frequency relation reveals the lineshape of the ZPT, which is a Lorentzian function as expected for a two level system. The center frequency ν_0 , and the width $\Delta\nu$ of the ZPT obtained this way were shown to be sensitive probes of heterogeneities among the host matrix [14,17-20]. Repeating this procedure in a continuous fashion further enables monitoring abrupt spectral shifts in the ZPT of a molecule, known as spectral dynamics [21,22].

In studies cited in the above paragraph, molecules were excited through their ZPTs. While the narrow linewidth of the ZPT provides very high selectivity in excitation, and very high sensitivity in spectral resolution, there are also some drawbacks of this approach. For example, the resonance condition between the ZPT and the excitation laser is so tight that it can easily get lost by minute shifts in the ZPT. Only a few systems with

exceptionally stable ZPTs are suitable for this excitation scheme. For the remaining systems, the shifts in the spectral position of the ZPT may even fall outside the limited tuning range of the laser. As another drawback, since the ZPT is reserved for excitation, it is not possible to detect fluorescence occurring through this transition. The (red-shifted) PSB used in detection on the other hand offers poor signal to noise ratio (SNR) due to its much broader spectral width.

As an alternative approach, the molecule can be excited to higher vibrational states of S_1 , and its fluorescence can then be detected through the ZPT. In this case, the linewidth of the transition² used for excitation will not be as narrow as the ZPT. Although this causes much of the selectivity in excitation, and resolution in determining the ZPT lineshape to be lost, it also makes the excitation process almost unaffected from spectral shifts. This enables exploring systems with large spectral dynamics [23,24]. Furthermore, the opportunity to detect fluorescence from the transform limited ZPT opens up new roles for single molecules in quantum optical demonstrations based on indistinguishable photons [25-31].

1.3 Single Emitters

Single molecules are just one group of the model systems that reveal the discrete nature of light. A general name designating all groups of such systems is the phrase “single emitter”. Single emitters are the ultimate units (capable of emitting) in a light source. They emit one and only one photon at a time³. In other words, a single emitter cannot emit photons simultaneously: After emitting a photon, it takes some time -known as the excited state lifetime- for the emitter to recover back to the state where it can be excited again. This “separation in time” of photons is called photon antibunching.

² Such a transition is termed as “vibronic transition”, for it brings a change to both the electronic- and the vibrational state of the molecule.

³ For this reason, single emitters are also termed as single photon sources [31].

Observation of antibunching in a set of photons (or light) is considered as an unambiguous proof that this set of photons is coming from a single emitter.

Several systems were shown to be single emitters, based on the photon antibunching evidence. These include cold atoms [33,34] and trapped ions [35], which are perfect quantum emitters in their gas state. They possess extremely sharp transitions, well-known energy levels, and available emission at optical frequencies. However the cost and short measurement time of the experiments (on the order of milliseconds) severely limit their use for practical applications.

Single emitters from solid state are experimentally less demanding. These experiments are done using samples, in which the emitter of interest is found as a dopant. The dopant concentration is adjusted to ensure that only one emitter is excited in the probe volume. Excitation is mostly optical, but the more attractive electrical methods were also reported [36,37]. Experiment times are only limited by the photostability of the emitter, and can be as long as hours. Examples of solid state emitters include fluorescent dye molecules, color centers, and quantum dots.

Fluorescent dye molecules are probably the best candidates for a feasible single emitter. They have high quantum yield, short fluorescence lifetime, and good photostability when protected from atmospheric oxygen. Their emission spectra are wide at room temperature, but can be made narrower by cooling to cryogenic temperatures as mentioned in Section 1.2. Several molecule-host pairs were shown to yield excellent single emitter properties. The most prominent one of these is the terylene in p-terphenyl system, studied extensively at both cryogenic- [13,14,16,18] and room [38-41] temperatures. The p-terphenyl molecules are made up of three phenyl rings, and form a rigid crystalline matrix. Terylene molecules doped into this matrix are well isolated from quenching effects, and can fluoresce for sufficiently long times. Other dye-host pairs with comparable performance include 7,8,15,16-dibenzoterylene (DBT) in anthracene [19,29,42-45], 2,3,8,9-dibenzanthanthrene (DBATT) in methyl methacrylate [17], and pentacene in p-terphenyl [12,15].

Color centers are crystal defects in inorganic solids. Very few of these systems were found to be suitable as a single emitter. Nitrogen-vacancy center in diamond (NV center) [46], and nickel-nitrogen complex [47] are the most promising color centers. They have perfect photostability, high quantum yield, but they also exhibit a dark state that limits their photoluminescence [48]. The relatively high refractive index of diamond also causes difficulties in the collection efficiency.

Quantum dots are another major candidate for single emitters. They are semiconductor nanocrystals, grown either in solution by chemical synthesis [49], or on single crystalline substrates by molecular beam epitaxy [50,51]. These are also known as colloidal and self-assembled quantum dots respectively. The most widely studied quantum dots are CdSe in ZnSe, and InAs in GaAs. Self assembled quantum dots are better than most organic molecules in terms of their photostability, however their low-temperature operation, frequent blinking, and longer lifetimes hinder their use as a single emitter.

For all of these single emitters, coupling the emission to a resonant cavity is very desirable for practical applications. A cavity can decrease the fluorescence lifetime and improve photon emission rate, it can guide the emission to a well-defined spatial mode and increase collection efficiency, and it can also spectrally collect the emission to a narrow wavelength range. Although it was shown to be possible to obtain cavity structures with embedded dye molecules [45,52,53], the type of single emitters that is practically most feasible for this purpose [36, 54-56] and also for the next step of integrating them into electrical circuits [57] is self assembled quantum dots.

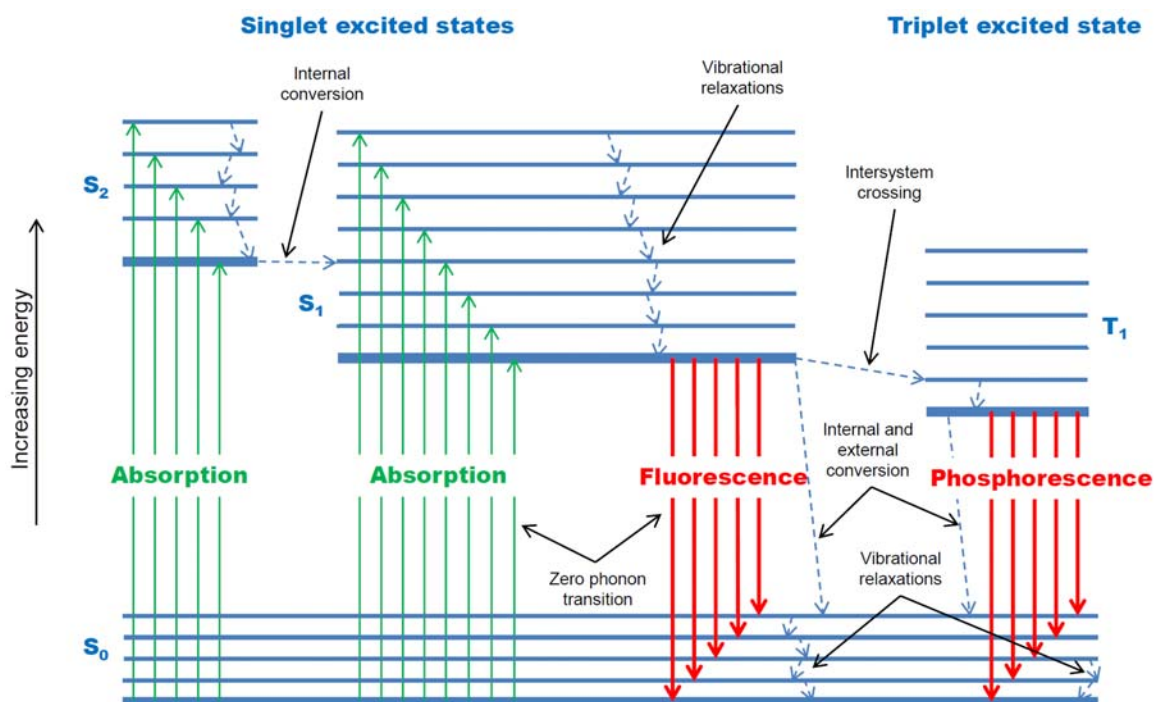


Figure 1.1: Jablonski diagram showing molecular energy levels and transitions between them. Approximate timescales for these transitions are given in Table 1.1.

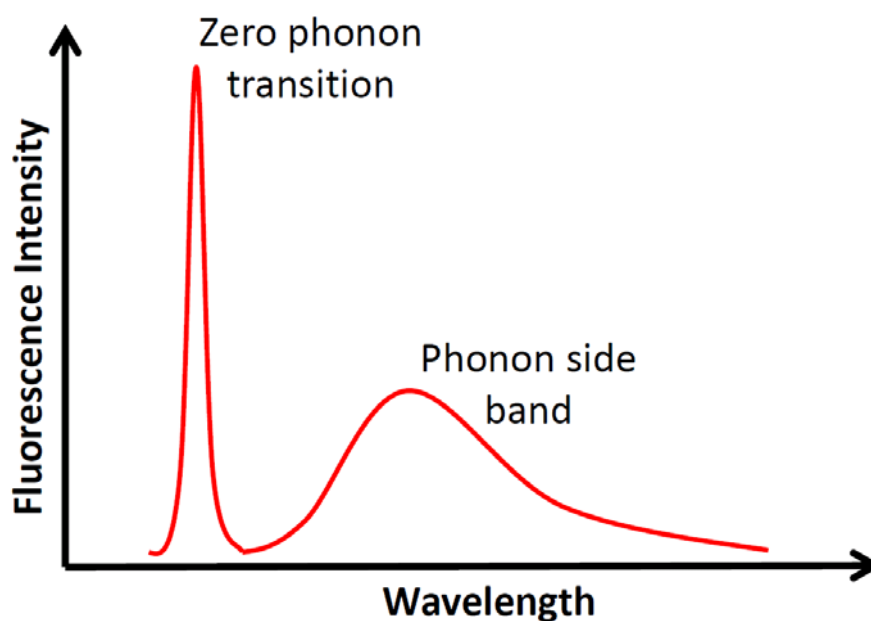


Figure 1.2: Schematic drawing showing how the zero phonon transition and the phonon side band would appear in a fluorescence spectrum (height and width of the peaks are not drawn to scale).

Chapter 2

REALIZATION OF SINGLE MOLECULE EXPERIMENTS

2.1 Introduction

The techniques for far field optical detection of fluorescent dye molecules are usually applied by bringing together some commercial equipment in a relatively custom design. An almost indispensable part in these setups is a laser light source used for exciting the dye molecules. Lasers provide a stable, collimated beam of light that can be directed to the sample with minimal losses. Their inherent polarization and spectrally narrow emission are additional benefits for single molecule experiments. Another important part commonly used in realizations of these techniques (mostly at ambient conditions) is an inverted microscope. Being already designed for fluorescence imaging, inverted microscopes provide convenience in approaching the sample, collecting its emission, and separating this from the excitation light. More importantly, they offer a variety of high numerical aperture (NA) color-corrected objectives, which are crucial for improving the collection efficiency. Other parts in single molecule setups include optical elements (filters, mirrors, beamsplitters, lenses, etc.), mechanical elements (mounts, adapters, microstages, etc.), spectrometers, data acquisition or device control electronics, and detectors. While lasers and microscopes are almost universal, the latter components may show considerable variations depending on the type of the experiment.

The techniques for far field optical detection of fluorescent dye molecules can be classified in two distinct groups as wide-field and confocal, based on the employed excitation and detection arrangement. In the wide-field arrangement, a large area of the sample is exposed to the excitation laser and imaged with a highly sensitive scientific camera. This technique is useful for capturing the motion of dye molecules over a wide

area of $\sim 50\mu\text{m} \times 50\mu\text{m}$, with moderate temporal resolution of $\sim 100\text{ms}$ [58-60]. Another application of wide-field single molecule detection that arose with the development of photo-switchable dyes is the super-resolution microscopy technique termed by the acronyms PALM (photo-activated localization microscopy) [61] or STORM (stochastic optical reconstruction microscopy) [62] by the two inventing groups. With this new technique, it was shown possible to image biological features that were selectively labeled with photo-switchable dyes, with a resolution of $\sim 20\text{nm}$. The alternative technique, confocal detection, on the contrary probes a very small region of $\sim 1\mu\text{m}^3$ of the sample, using point detectors. The point detectors allow for much better temporal resolution of $\sim 0.5\text{ns}$ as compared to a regular CCD camera. This technique is suitable for studying fast events associated with fluorescent dye molecules, such as transition rates, chain dynamics, or diffusion [63-65].

In addition to the above distinction in techniques, similar classifications can also be made for the measurements, based on some experimental conditions of interest. For example, they can be classified as room- or low temperature measurements, based on temperature; or they can be classified as spatially-, temporally- or spectrally-resolved measurements, based on the type of the collected data; or alternatively they can also be classified based on the sample of interest as measurements detecting molecules freely diffusing in a liquid, confined to move on a surface, or rigidly fixed in a solid.

The present chapter explains details of the infrastructure developed for the experiments in this thesis. These are a room temperature setup that can be used for either wide-field or confocal detection, and a cryostat setup that employs confocal detection for low temperature measurements. Section 2 describes the room temperature setup. A considerable part of the efforts regarding infrastructure in this study were about programming tasks required for confocal detection. These are described separately as Section 3. Section 4 then gives details of the cryostat setup. Sections 2-4 also provide sample data recorded with the setups for verification purposes. Section 5 finally concludes the chapter with a brief summary.

2.2 Room Temperature Setup

The room temperature setup offers both wide-field and confocal detection techniques. As presented in Figure 2.1, it has been built around a commercial inverted microscope frame (Nikon Eclipse TE2000-U). The box seen on the left side of the microscope contains the camera for wide-field detection (Hamamatsu C9100-13), whereas the one on the right encloses the confocal detection part. There is also another camera (Jena Optics) mounted on the front port of the microscope. This is used for general inspection of the sample, taking transmission images, or for other everyday tasks like finding the focus, aligning the excitation beam etc. A piezo scanner (Physical Instruments; stage: P-733.3DD; controller: E-509.C3A) has been mounted in place of the original x-y stage of the microscope, for use in confocal detection. Excitation light comes either from a 532nm continuous wave (cw) diode laser (Deal Extreme), or a tunable subpicosecond pulsed fiber laser (Toptica FSS) with tunability range from 520-700nm and repetition rate of 80MHz. A schematic drawing of the room temperature setup is presented in Figure 2.2.

In the standard wide-field arrangement, excitation laser is focused at the center of the back focal plane of the objective, and leaves the front end as a parallel beam of light that propagates through the sample, illuminating the whole field of view (hence the name wide-field). The fluorescence emission of the dye molecules within the illuminated area are then collected by the same objective, filtered from the excitation laser, and imaged onto the camera on the left side.

The cameras used in single molecule experiments are very special devices. They have back illuminated, cooled CCD chips that enable a high quantum efficiency of around 90% in the visible range. They also have an on-chip multiplying register that multiplies the signal charges (electrons) from the pixels, before being transferred to a current amplifier in the read-out circuitry. The main source of noise in a CCD camera is this current amplifier, and the noise level depends on frequency; i.e. number of pixels per time read-out from the chip (the faster the frame rate, the more noise is introduced by current amplification). By tuning the gain of the so-called electron multiplication, high sensitivity (on the level of

single photon) can be achieved against read-out noise, even with high frame rates (close to 50fps).

The back illuminated pixel design, and the on-chip multiplying register make these cameras so sensitive that they can hardly be deemed as the limiting part in single molecule detection. The main limitation comes from the background fluorescence of the sample that almost always has some component passing through the emission filters. In the above-described standard wide-field arrangement, since the excitation beam travels through the whole layer of the sample, the only remedy to reduce background fluorescence is to work with thinner samples.

An alternative excitation geometry employed in wide-field single molecule detection is the total internal reflection (TIRF) illumination, where the excitation laser is focused at the edge of the back focal plane of the objective. In this case the excitation beam meets the coverslip-sample interface at an angle allowing total internal reflection, and the molecules are excited by the evanescent field penetrating to the sample. The penetration depth is usually $\sim 100\text{nm}$, which results in an inherent reduction of the background fluorescence in thick samples. The TIRF excitation requires objectives that can support the critical angle. While an exact value depends on the refractive index of the film, the objective should typically have an NA of 1.45 or above. Although the background reduction is a great advantage of TIRF, the resulting field of view is usually smaller and less homogeneously illuminated as compared to the standard (parallel) excitation geometry. Therefore, the standard (parallel) excitation geometry can still be preferable for samples thinner than the penetration depth of the evanescent field.

In addition to background reduction, the standard (parallel illumination) and TIRF geometries may also result in different image patterns, depending on the orientation of the dye molecule. The image pattern of a dipole emitter that lies on the focal plane is given by the Airy function

$$I(r) = \frac{[J_1(ar)]^2}{\pi r^2}, \quad (2.1)$$

where J_1 is the Bessel function of the first kind, first order, r is the azimuthal distance from the center of the (symmetric) image pattern, and $a \equiv \frac{2\pi NA}{\lambda M}$, with λ and M denoting the emission wavelength and magnification. In practice the Airy-shaped intensity distribution is approximated by a 2-D Gaussian function. For molecules still at the focal distance but oriented such that their transition dipole moments also have component along the optical axis, eq. (2.1) becomes an insufficient representation. Image patterns of such molecules are calculated numerically. For the case when the dipole moment is vertical to the focal plane (parallel to the optical axis), the resulting pattern becomes a doughnut shape. The Airy-shaped intensity distribution and the doughnut shape correspond to two extreme orientations of the molecule's transition dipole moment with respect to the focal plane. In the standard wide-field configuration, predominantly the molecules with their transition dipole moments parallel to the focal plane (perpendicular to the optical axis) are excited. Therefore, one should not expect to see doughnut shapes with the standard configuration. The TIRF geometry on the other hand can excite all possible orientations.

Figure 2.3 shows two images acquired with the wide-field setup, describing these effects. The sample was crystals of p-terphenyl that were obtained on a glass coverslip via spin coating, and have terrylene dye molecules embedded in them. The crystalline structure of the matrix in this sample was shown to give terrylene molecules (and hence their transition dipole moments) a preferential orientation that is parallel to the optical axis [66]. When the sample was illuminated with the standard geometry, terrylene molecules could not be excited efficiently, which resulted in almost a dark image as shown in Figure 2.3.a. However, with the TIRF illumination, terrylene molecules were excited and appeared as doughnut-shaped features in the resulting image (Figure 2.3.b).

Besides wide-field microscopy, the room temperature setup also has a second part for confocal detection, located on the right side of the microscope (Figure 2.2). In this arrangement, the excitation laser arrives to the back aperture of the objective as a collimated beam, and gets focused to a diffraction limited spot on the focal plane. Emission from the sample is collected by the same objective, and focused onto a pinhole

with the microscope's tube lens. The pinhole acts as a spatial filter that passes an emission corresponding to $\sim 0.5\mu\text{m}$ layer of the sample, and blocks the remaining out of focus light. Light exiting the pinhole is then collimated again, passed through appropriate filters, split into two with a beamsplitter, and focused onto separate point detectors. The point detectors used in the room temperature setup are avalanche photodiode detectors (APD; Perkin Elmer, SPCM-AQR-13; dark counts: 250 cps), which are a type of single photon counters that deliver an electronic pulse per each detected photon. More information on these detectors will be provided in Chapter 5. A short-pass filter is put between the two APDs to prevent any IR photons generated on one APD from being detected by the other. The reason for using two detectors instead of one is to eliminate the dead time and afterpulsing of the APDs. Dead time is the minimum recovery time that has to pass between consecutive photon detections. Afterpulses are spurious counts generated by the avalanche process in an APD. Both of these limitations can be circumvented by the clever solution of using two detectors, known as Hanbury Brown and Twiss configuration. Using two detectors may also be advantageous in studying –via appropriate filtering– spectrally distinct events occurring at the same time and position. The confocal detection part of the room temperature setup offers versatile single molecule measurements. These will be briefly explained in the next section when discussing the programming details.

2.3 Programing Tasks for Confocal Detection

At the heart of the confocal detection part of the room temperature setup, lies a multi-purpose PCI express card (National Instruments, PCIe-6363), used for both data acquisition and device control. The card has 4 32-bit counters (2 of them are used), several analog and digital input/output channels, and a 100MHz internal clock. It was programmed in Matlab, using the associated development library NI-DAQmx. The program in Matlab not only controls the card, but also serves as a complete platform for doing measurements, storing retrieving or exporting data, and some basic analyses. It works through graphical interfaces, without any need for programming knowledge. A tutorial of this program can be found in Appendix A.

The devices that are connected to the card are the piezo scanner and the APDs mentioned in Section 2.2, and a time-to-amplitude converter (TAC; Ortec, 566) (Figure 2.4). These were brought together to realize different types of measurements such as imaging, time trace recording, coincidence counting, and fluorescence correlation spectroscopy (FCS). The following subsections describe technical details of these measurements.

2.3.1 Imaging

A piezo scanner is needed in confocal detection mainly for bringing one of the molecules within the sample onto the focal spot, and keeping it there during data recording. Although the main purpose of the scanner is just this positioning of the molecule, it requires in the first place to know where the molecules are. As a standard procedure in single molecule measurements employing confocal detection, one first records a fluorescence image of the sample by raster-scanning it over the excitation beam focus. The isolated bright features in the resulting image then become candidate positions to expect individual dye molecules. Therefore the first (but not main) task of the piezo stage is to scan the sample to develop a fluorescence image.

This image could be constructed in a “point by point” fashion using two nested for loops (inner one for the fast-, outer one for the slow axis), to command a pixel’s position to the stage, count APD pulses for a certain integration time, command the next pixel’s position, count APD pulses again, and repeat this procedure for all the pixels of the image. Considering that the stage’s rise time for a commanded position is around 10ms, acquiring a moderate size image of 200×200 pixels with this approach would cost an extra time of $200 \times 200 \times 10\text{ms} = 400\text{s}$, which is completely lost. Such an approach would be too slow to implement in practice. An alternative approach is to scan the sample using hardware-timed waveform commands (a triangular wave along the fast axis, and a staircase ramp along the slow axis). This brings a continuous motion along the fast axis and completely eliminates the dead time in the (software-timed) point by point approach. However, it also requires a critical synchronization between the piezo stage motion and the APD readings, which if

not maintained may cause to pixel/line shifts in the image. Although there may be some post-recording ways to correct for an offset between the two [67], a real-time visualization of the scanned region is much more preferable, as for example when slightly adjusting the focus of the microscope. For the equipment used in this study, the easiest strategy to maintain proper scanning with real-time visualization was proven to read the position sensors of the stage per each intensity reading from the detectors. This way, the intensity and position data could be associated with each other even when there is a discrepancy between the commanded waveform and the actual movement of the scanner.

Area scanning has been programmed as four synchronized tasks: two of them are counter input tasks (only one counter is allowed in a task), the third one is an analog output task with two channels, and the fourth one is an analog input task again with two channels. The clock shared by these tasks is determined by the number of data points per unit time used in the waveform. This is not always the same with the number of pixels per unit time: There is an oversampling parameter included in the program that determines the ratio of the number of data points in the waveform to the number of pixels in the image. This parameter is intended for maintaining a smoother motion. In the extreme case, the (common) maximum data transfer rate in these tasks becomes 200kHz. The limiting values for the number of pixels, the integration time, or the oversampling parameter are set by the size of the space to be allocated from the memory, rather than the maximum data transfer rate. In any case, the allowable ranges are far sufficient for single molecule studies. The typical detection rate that can be obtained with a good dye, when the dye molecule is saturated, is around 1MHz (i.e. 10^6 photons/s). Given this fact, an integration time shorter than 0.5ms would not be so useful due to reduced SNR. This also justifies the use of a piezo stage in these experiments instead of a commercial confocal microscope with the much faster beam scanning technology.

Figure 2.5.a shows an example confocal image of a region that is $15\mu\text{m}\times 15\mu\text{m}$ in size. The image is 300×300 pixels, and recorded with 0.5ms/pixel integration time in 48s. Figure 2.5.b shows another image of the same region taken by the wide-field imaging part

of the room temperature setup described in Section 2.2. The agreement between these two images verifies proper operation of the scanning program.

Although it was the most demanding part of the programming work, the whole purpose of scanning was to be able to locate single molecules. The next step is to bring one of the molecules onto the focal spot, and record some data of interest from it, as described in the following subsections.

2.3.2 Time Trace Recording

An intensity-versus-time data, also called “intensity time trace” or just “time trace”, is often times needed in single molecule studies. It is a versatile measurement used for following changes in the fluorescence intensity of a molecule as a function of time. The changes can be due to many different effects that are either introduced in a controlled fashion by the experimenter (such as increasing excitation power to observe saturation, or rotating excitation polarization to determine molecule’s orientation), or randomly by nature (such as going temporarily into a dark state; a phenomenon called blinking, or photobleaching). While a direct inspection of the data reveals changes in the milliseconds to seconds time scales, the data can also be correlated to obtain typical timescales of faster events on the microsecond range (see Subsection 2.3.4). The intensity time trace is also useful in determining background levels under various conditions, or in preparing the setup (e.g. aligning the pinhole/lenses or adjusting neutral density filters).

The time trace program was written as two synchronized counter input tasks, each using one of the counters on the card. In a simplified picture, these counters are electronic circuits with 3 terminals: source, sample, and output. They continuously count the electrical pulses arriving at their source terminal, and deliver the number of counts to the output terminal each time when they receive a pulse from their sample terminal. The signals on their source and sample terminals need not be periodic. As being 32-bit counters, they overrun at every 2^{32} pulse arriving their source terminal. If a counter has never been read within the course of these 2^{32} pulses, the overrun event results in an error that abandons the whole counter input task. On the other hand, if the counter has been read

at least once, the task continues by resetting the counter. In other words, the NI-DAQmx library –through this error– wants to ensure that overrun events occur within user’s notice.

The counters were programmed to count APD pulses in two alternative ways, as either synchronously or asynchronously. In synchronous acquisition, APD pulses are connected to the source terminals, and a periodic signal generated internally by the card is connected to the sample terminals. This configuration corresponds to an intensity measurement at regular time intervals. The temporal resolution of the measurement is determined by how small/large these regular time intervals can be made. The limitation on the small end comes from the data transfer rate, while that on the large end is imposed by the overrunning error mentioned above. To accommodate these limitations, the allowable temporal resolution in synchronous acquisition was kept within $1\mu\text{s}$ to 1s . The upper limit was in fact chosen almost arbitrarily. With common detection rates in a single molecule experiment, counter overruns are unlikely to happen even through the whole measurement long, letting alone 1s (for a relatively high detection rate of 1MHz , a counter overruns in $2^{32}/10^6 \approx 4295\text{s} \approx 1.2\text{hour}$). For the same reason, overruns are checked only when retrieving a recorded time trace, and ignored in real time displaying (to gain speed). The only effect of an overrun –if it ever happens–, is that it appears and flows away as a notch on the real time intensity-versus-time graph. In the asynchronous configuration, the 100MHz internal clock of the card is connected to the source of the counters, and the APD signals are this time connected to the sample terminals. This way, each time a photon is detected, the number of clock pulses counted until that time is delivered to the output terminal of the counter. This corresponds to a time measurement that determines the arrival time of each photon with $(100\text{MHz})^{-1} = 10\text{ns}$ resolution. Again due to the way NI-DAQmx library handles errors (there may be technical reasons for this that fall outside the scope of this thesis), the whole task is abandoned when two or more sample pulses (in this case APD pulses) arrive within a source pulse (in this case clock pulses). Luckily, the 50ns dead time of the APDs saves this complication. If the dead time were shorter than 10ns , there would be no possibility to detect photons asynchronously with the current configuration.

Both modes of acquisition have their own advantages and weaknesses. In detecting intense signals, the synchronous acquisition is more advantageous. While the exact value for the maximum photon rate that can be handled with this configuration depends on the time resolution of the measurement, it is always far above the maximum detection rate of the APD. Therefore with synchronous acquisition, the data acquisition electronics or program does not impose any limitations on the maximum measurable photon rate (it is limited by the detector). For asynchronous acquisition on the other hand, the maximum measurable photon rate cannot be assigned a definite value. It varies greatly depending on: i) the time interval between incoming photons, ii) the size of the on board memory (first in first out (FIFO) buffer of the card), and iii) the data transfer rate between the on board memory and the memory on the computer. If the on board memory is not large enough, it can easily get filled and overwritten by instantaneous bursts in intensity, which results in an error terminating the task and thus spoiling the measurement. This can happen even with signals that may appear as of moderate-intensity on the time scale of a second (for example 50kHz per channel). The key parameter here is the fluctuations in the number of photons that occur on the time scale of the data transfer from card's on board memory to computer's memory¹. These fluctuations depend on the statistical characteristic of the signal, but as a general trend, are expected to become more probable with increasing intensity². With fluorescence from a concentrated dye solution excited by the pulsed laser mentioned in Section 2.2, the on board memory of the card becomes overwritten (within typical measurement times of several minutes) at an average detection rate of $\approx 350\text{kHz}$ per channel; whereas with perfectly periodic pulses of a signal generator, it proves to be

¹ The time it takes for data transfer from the on board memory to the computer memory depends on computer properties and activity. A simple estimate can be done based on the following two specifications: i) the maximum detection rate of the APD is $\sim 20\text{MHz}$; and ii) the size of the on board memory is 127 samples. The first one means that the on board memory cannot be filled faster than 20×10^6 samples/s. Combining this rate with the size information, one concludes that the present configuration should be able to tolerate any bursts in photon rates, as long as they relax within $127/(20 \times 10^6) = 6.35\mu\text{s}$.

² This probability also depends on the acquisition time. In principle, any asynchronous time trace acquisition –if not terminated otherwise (for example by the user upon finishing his experiment) - will eventually get spoiled by an “on board memory overwrite” error.

sufficient up to 1MHz per channel. This shows that the limitation on the maximum measurable photon rate is not set by the efficiency of the program, but by a combination of the above-mentioned three factors. Unfortunately, none of these factors can be made better: i) the measurements are based on fluorescence, which defines the nature of the signal, ii) the on board memory of the card has a fixed size of 127 samples per counter, and iii) the data transfer method between the card and the computer was already set to the fastest available option (direct memory access). In conclusion, for typical measurement times of several minutes, maximum measurable photon rate in asynchronous acquisition is limited to $\approx 350\text{kHz}$ per channel, and so synchronous acquisition is more advantageous in this connection. However when it comes to temporal resolution, asynchronous acquisition is obviously more advantageous. Similar issues with data transfer rate this time limit the time resolution in the synchronous acquisition. As another comparison, one must also consider the size of the generated data files. With synchronous acquisition, a 1-minute-long time trace of $1\mu\text{s}$ resolution would be $60 \times 10^6 \times 32 = 1.92 \times 10^9 \text{bits} = 1.79\text{GB}$, irrespective of the photon detection rate. For a typical photon detection rate of $5 \times 10^4 \text{photons/s}$, an asynchronously-recorded 1-minute-long time trace on the other hand would only be $60 \times 5 \times 10^4 \times 32 = 9.6 \times 10^7 \text{bits} = 91.6\text{MB}$. As this example shows, for typical values in single molecule experiments, synchronous acquisition generates unnecessarily large files. The term unnecessary is used here to signify that most of the records in a synchronously-recorded time trace would not correspond to any photon counts at all (in the above example, at least 95% of the records would correspond to 0 photons). The discussions so far comparing the two acquisition modes are summarized in Table 2.1. As these suggest, synchronous acquisition should be used in cases where a coarse time resolution such as $\geq 1\text{ms}$ would suffice or where one deals with high intensity levels. Asynchronous acquisition should be chosen when high time resolution is needed.

For both modes of acquisition, data is recorded as it comes from the counter (i.e. as raw 32-bit unsigned integers), without any processing. As an example of some possible processing that could have been done, one can deem overrun corrections in the asynchronous recording mode. In this configuration, the counters get overrun at every

$2^{32}/10^8 = 42.95\text{s}$, which should be corrected both on-the-fly to display the intensity versus time graph correctly, and afterwards when retrieving a recorded time trace. Although the necessary corrections are done each time a time trace is displayed, the data is recorded as is. A second example could be for the synchronous recording mode, which –depending on time resolution– may suffer from large data files. It could be possible to heal this problem by recording the counter readings with fewer bits. With the example of the above paragraph, a synchronously recorded time trace of $1\mu\text{s}$ resolution never requires a 32-bit representation. This could be replaced by any representation that can express the highest instantaneous (i.e. on $1\mu\text{s}$ scale) photon rate, or to be on the safe side the highest photon rate that the APD can detect. The APD gets saturated at around 20MHz. This means that a 5-bit representation would also be sufficient for a $1\mu\text{s}$ -resolution time trace ($2^5/(1\mu\text{s}) = 32\text{MHz}$), and so it could have been recorded using a 5-bit representation instead. However, since the new representation depends on the time resolution and more bits are required for lower resolutions; such a change of representations would be too intricate to be justified for a saving from disc space. Therefore data in time trace measurements is always recorded as 32-bit unsigned integers.

Acquisition Mode Property	Synchronous	Asynchronous
Counter connections	Source: APD Sample: Sample clock (1MHz – 1Hz)	Source: 100MHz clock Sample: APD
Time resolution	$1\mu\text{s} - 1\text{s}$.	10ns.
Maximum count rate per channel	Unlimited.	350kHz.
Maximum acquisition time	Unlimited.	Unlimited (unless on board memory is overwritten).
Main advantage	Detector-limited maximum count rate.	Fine time resolution.
Main disadvantage	Large data files with $\leq 10\mu\text{s}$ time resolutions.	Limited maximum count rate.

Table 2.1: Comparison of synchronous and asynchronous acquisition modes.

Following these discussions, a sample time trace is shown in Figure 2.6. It is recorded from a single terrylene molecule in a poly(methyl methacrylate) (PMMA) film, using the asynchronous mode. The molecule emits at a count rate of $\approx 20\text{kHz}$ on a 400Hz background until it bleaches at $t \approx 26\text{s}$. Before bleaching, the molecule also goes temporarily into a dark state at $t \approx 19\text{s}$; an event commonly referred to as blinking. The digital on/off nature of the fluorescence intensity during blinking and bleaching is strong evidence that the recorded signal is emitted by a single molecule.

2.3.3 Coincidence Counting

TAC is an electronic device that measures the time elapsed between two events. It has 2 input channels and 1 output channel. The input channels are commonly referred to as start and stop channels. For the TAC alone, the events mean standard electronic pulses (TTL) arriving at its start and stop channels. The real physical occurrence of the events and how they are converted into TTL pulses (in this case via APDs) are considered independently from the TAC. Once the start-stop channels of the TAC are activated by the TTL pulses, the time between them is converted into a voltage and delivered from the output channel as another electrical pulse. The amplitude of the resulting output pulse is proportional to the time difference. Its width is immaterial, and can be tuned according to the detection speed.

TAC is most suitable for measuring times from tens of picoseconds to hundreds of nanoseconds. The maximum measurable time between start and stop pulses, termed full-scale time limit (FSTL), can be set by a combination of switches on the device (range and multiplier switches). The FSTL setting also determines the time resolution of the TAC. For example for a typical FSTL of 100ns , the specified resolution becomes 15ps . In fact, such fine time resolutions are never benefited in the measurements due to the much higher jitter (uncertainty in response time) of the APDs. Nevertheless they are still useful in determining the overall time resolution of the whole detection process (instrument response function: IRF), where detector jitter is the limiting component. The linearity of a TAC (i.e. the proportionality between amplitude of the generated voltage pulse and the

actual time between start-stop pulses) is usually not so reliable at the edges of the FSTL (i.e. for times slightly longer/shorter than the IRF/FSTL). In order to measure short times, a common trick applied in coincidence counting is to make the stop pulses delayed about half the FSTL. This is done by using a longer cable between the stop detector and the TAC (longer as compared to the one between the start detector and the TAC). This way, the short time is artificially carried closer to the center of the FSTL, where the TAC operates most linearly. The length of the delay line is adjusted by trial and error, but usually 1m of extra cable corresponds to a delay of 5ns.

One application of TAC is coincidence detection. Coincidence detection is a general term used for joint detection of two or more particles on separate detectors. The particles are detected within a very short time interval, so that they can be regarded as coinciding with each other within that interval. In coincidence detection of two photons with a TAC, each coincidence event is detected as a voltage pulse on the output channel of the TAC. A typical measurement involves detecting thousands of such pulses, which are not only counted but also registered as a function of their heights. This way, one can form a histogram of coincidence events, where the horizontal axis is the time interval between the two (coinciding) photon detections. Such a histogram will hereafter be referred to as a TAC histogram. Coincidence detection can be used for many purposes such as observing the photon antibunching phenomenon, measuring fluorescence lifetime, or determining the IRF. It can be done using either a pulsed or a cw laser³. A pulsed laser with suitable repetition rate can be used for any of the above-mentioned applications (provided that its pulsewidth is shorter than the fluorescence lifetime or the IRF). A cw laser on the other hand is useful only when working with a single emitter, to observe the photon antibunching phenomenon, or to measure its fluorescence lifetime.

³ When employed with a pulsed laser, one of the TAC inputs can be fed from a synchronization signal denoting laser pulses (being either an electrical signal from the laser or generated optically by a suitable detector). This very similar configuration is termed time correlated single photon counting (TCSPC), meaning that the time intervals outputted by the TAC are in this case referenced to laser pulses.

The coincidence detection program was written as an analog input task that reads voltages from the output channel of the TAC with a high sampling rate (1MHz), to sufficiently resolve the pulses. It analyzes the acquired data stream in real time to find the pulses and determine their heights. When recording data, only the resulting pulse heights are stored. The raw voltage-versus-time data stream used in the analysis is not preserved. Due to its high sampling rate, the analog input task is gated by the “valid conversion” signal from the TAC. This is a digital signal that becomes high when an output pulse is released. It is important that the cable carrying this signal should be shorter than the one carrying the TAC output. Otherwise the rise of the output pulse may not be captured.

Two sample TAC histograms recorded from single terrylene molecules in p-terphenyl are shown in Figure 2.7. The FSTL was 100ns for the measurement of Figure 2.7.a, and was brought to 200ns in Figure 2.7.b to capture more of the long delay time behavior. Both histograms were plotted with 500 bins. The artificial delay of the stop pulses due to the delay line was subtracted from the raw time intervals. Thus, the delay time axes of the histograms show the time elapsed between real photon detection events, and not the time elapsed between their corresponding electrical pulses. A negative delay time in this case corresponds to a coincidence, for which the real photon detection event that produced the electrical stop pulse has actually happened earlier than that produced the electrical start pulse. In other words, the order between real photon detection events and their corresponding pulses gets reversed for coincidences that occur in time intervals less than the time spent in the delay cable. This reversal in the order of start-stop events is expressed as a negative delay time. The molecules were excited by the cw diode laser. Under cw excitation, a TAC histogram would be a flat line (similar coincidence counts for all bins) if the photons reaching the detector were emitted at random times. The most distinguishing feature of the histograms in Figure 2.7 is therefore the dip around their zero delay time. This dip is the experimental evidence of the photon antibunching phenomenon described in Section 1.3. The number of coincidences decreases as the time interval between their photon detection events gets shorter, resulting in almost no coincidence for zero time intervals. This proves that two or more photons cannot be emitted simultaneously (i.e.

within zero time interval) from a single emitter. The not-perfect decay of these antibunching dips to zero coincidence level is due to noise photons coming from sources other than the molecule in the focus. Besides antibunching evidence, a single molecule TAC histogram can also be used to determine the fluorescence lifetime of that particular molecule. To illustrate this, the histograms of Figure 2.7 were fitted by a simple exponential rise function

$$C(\tau) = C_{\infty} (1 - e^{-|\tau - \tau_0|/\tau_F}) + C_{bg}, \quad (2.2)$$

where $C(\tau)$ is the coincidence counts, τ is the delay time, τ_F is the fluorescence lifetime, C_{∞} is the coincidence counts for $|\tau| \gg \tau_F$, C_{bg} is the coincidence counts due to background, and τ_0 is the offset due to the delay line. When plotting histograms, τ_0 was subtracted from the delay time axis. The fit results are tabulated in Table 2.2.

	Molecule-1: Figure 2.7.a		Molecule-2: Figure 2.7.b	
	Fit value	95% Confidence interval	Fit value	95% Confidence interval
C_{∞} (counts/bin)	162	156 – 167	354	338 – 370
C_{bg} (counts/bin)	6	0 – 11	28	12 – 44
τ_F (ns)	7.6	7.1 – 8.0	6.9	6.4 – 7.4
τ_0 (ns)	49.9	49.7 – 50.0	48.9	48.7 – 49.1

Table 2.2: Results obtained from fitting eq. (2.2) to the TAC histograms in Figure 2.7.

It should be noted that the rise time of a single molecule TAC histogram recorded under cw excitation becomes equivalent to τ_F only in the low pumping regime. As the pumping rate, or in other words the excitation intensity increases, the rise time decreases. While a simple fit was sufficient for the above example, the rigorous way of determining τ_F from a cw TAC histogram would be to record several histograms with varying excitation intensities, plot rise times as a function of excitation intensity, and extrapolate this plot to get the τ_F value that corresponds to zero excitation intensity.

TAC histograms can also be used for determining the IRF. Figure 2.8.a shows a TAC histogram recorded with the pulsed laser mentioned in Section 2.2. The notch- and band-

pass filters shown in Figure 2.2 were taken out, and the reflection of the laser from a bare coverslip was directly sent to the APDs. Due to pulsed emission of the source, the detected photons arrive at times equal to an integer multiple of the pulse period $T = 1/(80\text{MHz}) = 12.5\text{ns}$. This results in a TAC histogram with coincidence counts peaking around delay times $|\tau| = nT$, where $n = 0, 1, 2, \dots$. Since the pulse duration of the laser –corresponding to uncertainty in photon arrival times– is much shorter than the expected range of the IRF (subpicosecond pulses compared to $\sim 500\text{ps}$ for IRF), the width of the coincidence peaks directly yields the IRF. Figure 2.8.b shows a magnified view of one of the coincidence peaks in Figure 2.8.a, along with a peak shape function (in this case Lorentzian) fitted to it. The fit gives a width of 555ps.

2.3.4 FCS

Strictly speaking, FCS in the form carried here is not a different type of measurement, but an analysis that complements the time trace measurements described in Subsection 2.3.2⁴. Although time trace measurements offer high temporal resolutions (see Table 2.1), the low intensity levels in single molecule detection hinder their use for transient analyses. In other words, the number of photons detected from a single molecule is not sufficient to produce a meaningful intensity-versus-time plot on submillisecond scale. A solution employed for this problem is to calculate the autocorrelation function of the intensity-versus-time data given by

$$G^{(2)}(\tau) = \langle I(t)I(t + \tau) \rangle, \quad (2.3)$$

where $G^{(2)}(\tau)$ is called the second order- or intensity autocorrelation function⁵, $I(t)$ is the intensity at time t , τ is the lag time, and $\langle \rangle$ denotes averaging over time [68].

⁴ The form of FCS described here is referred to as software correlation. This involves calculating the correlation function from an intensity-versus-time record, using a computer program. It is essentially a post-processing method. On the other hand there are also dedicated cards called hardware correlators that calculate the correlation function directly on their own arithmetic logic units. Hardware correlation must be regarded as a separate type of measurement, because in this case there is no need for an intensity-versus-time data.

⁵ The term “second order” comes from the fact that for a propagating electromagnetic wave, intensity goes with the second power of the electric field amplitude.

The behavior of $G^{(2)}(\tau)$ in the limiting cases is intuitive to understand FCS. For small τ , $G^{(2)}(\tau)$ becomes almost equal to the mean square intensity (i.e. $\langle I^2(t) \rangle$), whereas for large τ , the intensities at times t and $t + \tau$ become almost totally independent from each other, and $G^{(2)}(\tau)$ becomes equal to the square of the mean intensity (i.e. $\langle I(t) \rangle^2$). Since $\langle I^2(t) \rangle$ is always greater than or equal to $\langle I(t) \rangle^2$, the intensity autocorrelation function is either a decaying- or a constant function. Owing to this general behavior, $G^{(2)}(\tau)$ is customarily normalized by $\langle I(t) \rangle^2$, yielding the normalized intensity autocorrelation function

$$g^{(2)}(\tau) = \frac{\langle I(t)I(t+\tau) \rangle}{\langle I(t) \rangle^2}, \quad (2.4)$$

which for a fluctuating intensity always starts from a value greater than 1, and decays to 1 on the long τ limit [68].

In FCS, one calculates the $g^{(2)}(\tau)$ from a fluorescence time trace. If there are transient events causing fluctuations in fluorescence intensity, and if there are a large number of them within the recorded time trace, then their cumulative contributions appear as a decay in the $g^{(2)}(\tau)$ curve. The decay spreads over a range of τ values covering the characteristic duration of the transient events. In cases where there are two or more different types of transient events giving rise to fluctuations in fluorescence, their corresponding decays may overlap depending on characteristic durations. Although such complications have been tackled to study heterogeneities/distributions among/of similar events [69,70], it is usually much more preferable to deal with distinct events having characteristic durations separated by at least a factor of two.

FCS is most commonly used for studying random diffusion of dyes or dye-labeled molecules in liquids or gels either from a fundamental point of view [71,72], or for monitoring other related processes [59,73,74]. In these experiments, a very dilute (~ 1 nM) solution of the fluorescent molecule is used as the sample. The solution is so dilute that the number density of fluorescent molecules per volume probed by confocal detection is less than 1. In other words there is sometimes a molecule in the detection volume, and sometimes not. The occasional diffusion of (fluorescing) molecules into- and out of the detection volume causes spikes in the fluorescence time trace, which upon correlation

provide information about the average time a molecule spends within the detection volume (known as diffusion time).

As a second application area of FCS, one can deem transitions of a dye to its triplet state. These can be studied either when the molecules randomly diffuse in a liquid as described above, or immobilized in a matrix. In the former case the resulting $g^{(2)}(\tau)$ function exhibits two decays, one for the –relatively faster– transitions to triplet state, and the other for random diffusion. A model used in interpreting such data is:

$$g^{(2)}(\tau) = \left[1 - T + T e^{-\frac{\tau}{\tau_T}} \right] A \left(1 + \frac{\tau}{\tau_D} \right)^{-1} \left(1 + \frac{\tau}{\tau_D \kappa^2} \right)^{-1/2} + g_\infty, \quad (2.5)$$

where T is the triplet fraction of molecules, τ_T is the triplet state lifetime, A is the amplitude of the correlation curve, τ_D is the diffusion time, κ is the length to diameter ratio of the detection volume, and g_∞ is the long τ limit of $g^{(2)}(\tau)$ [75]. After fitting eq. (2.5) to the experimental $g^{(2)}(\tau)$ curve, if the diffusion coefficient D of the molecule in that liquid is known, the relations

$$D = \frac{\omega_0^2}{4\tau_D}, \text{ and } \kappa = \frac{z_0}{\omega_0} \quad (2.6)$$

can be used to calculate the diameter ω_0 and length z_0 of the detection volume, which then yield the effective detection volume V_{eff} of the setup according to

$$V_{eff} = \pi^{3/2} \omega_0^2 z_0. \quad (2.7)$$

The calculation of $g^{(2)}(\tau)$ is completely different for time traces recorded by synchronous and asynchronous acquisition modes (see Subsection 2.3.2). For synchronous time traces, the correlation program was written according to the so-called multi-tau algorithm described in [76,77]. This algorithm was designed for hardware correlators (see Footnote 4 in this chapter), and takes too long when implemented by a computer program. While a new version of it suitable for parallel computing (or equivalently suitable for vectorizing the code on a single computer) has been introduced in [77], the program here was still written according to the less complicated original version. The reason for this was that the typical count rates in an FCS experiment are not at a level of causing FIFO

overwrite problems for asynchronous acquisition. Taking into account also the time resolution advantage of asynchronous acquisition, a synchronous time trace would rarely be considered for FCS. Its correlation program was therefore written just to be available in exceptional cases. For asynchronous time traces, the correlation program was written according to an algorithm that calculates $g^{(2)}(\tau)$ directly from photon arrival times [78]. Owing to small data sizes of asynchronous acquisition, this algorithm allows for a much faster calculation of $g^{(2)}(\tau)$. With some sacrifices in the resulting $g^{(2)}(\tau)$ curve (such as limited number of lag times, or increased noise due to processing in batches) the algorithm can be implemented even in real-time, which may be useful while setting up the experiments.

In FCS, the correlation function is calculated at logarithmically spaced lag times, to cover a wide range of timescales on the same curve. In this case, the resolution of the time trace may become unnecessarily fine for longer lag times, and bring considerable noise into the correlation calculation. In order to reduce this noise, the original resolution of the time trace is coarsened in successive steps with increasing lag times. This procedure also significantly reduces the number of operations involved in the calculation and thus improves run time. A full description of the resolution coarsening, correlation and normalization procedures can be found in [76,77,79-81] for synchronously-, and in [78] for asynchronously-recorded time traces.

Figure 2.9 shows a sample FCS analysis. The time trace was recorded from freely diffusing Rhodamine-B molecules in water, using a 1.2 NA water immersion objective, and with the focal spot $20\mu\text{m}$ above the water-coverslip interface. Acquisition was done in the asynchronous mode for 120s. Average detection rates of the APDs were 10.47kHz and 8.38kHz. A 1-s part (from $t = 4.6\text{s}$ to 5.6s) of the recorded time trace is shown in Figure 2.9.a (sum of two channels), with 1ms integration time. The spikes in this plot correspond to molecules' passing through the probe volume. The resulting FCS curve and a fit by eq. (2.5) are shown in Figure 2.9.b. Details of the fit are tabulated in Table 2.3. Taking the diffusion coefficient of Rhodamine-B in water to be $D = 360\mu\text{m}^2/\text{s}$ [82], and using eq. (2.6), one calculates the diameter and length of the detection volume to be $\omega_0 = 268\text{nm}$

and $z_0 = 1.32\mu\text{m}$. Substituting these into eq. (2.7) then yields an effective detection volume of $V_{eff} = 0.53\text{fL}$.

	Fit value	95% Confidence interval
T	0.05	0.037 – 0.069
τ_T (μs)	1.82	0.56 – 3.08
A	0.94	0.93 – 0.95
τ_D (μs)	49.8	45.8 – 53.7
κ	4.94	2.41 – 7.47
g_∞	1.00	1.00 – 1.01

Table 2.3: Results obtained from fitting eq. (2.5) to the FCS curve in Figure 2.9.b.

For diffusion studies exemplified above, the liquid medium is mostly water. This is in part due to the historical development of FCS, which originated from molecular or cellular biology studies. Although it would be very interesting to study diffusion of molecules in liquids other than water (for example organic solvents), there are some experimental difficulties for this. Most organic solvents are volatile molecules that need to be enclosed in a chamber to prevent their evaporation. Given that at least one side of the chamber has to be made of a coverslip, it is not trivial to build a chamber without using glue. However organic solvents easily dissolve almost any glue one can find within reasonable effort. As a result, there have been very few studies that report FCS measurements in organic solvents [72,83,84]. This problem was handled in the present thesis as part of the FCS capability of the room temperature confocal detection setup. It was shown that water glass can serve as a glue to build a chamber for organic solvents. The chamber could be built in a very facile way by bringing together a coverslip, and a vial cut from bottom, as seen in Figure 2.10.a. The screwed cover of the vial is ideal for replacing the solution in the chamber, and preventing it from evaporation. This chamber was proven to keep aggressive solvents like chloroform or toluene for weeks without any evaporation. The coverslip can be separated from the vial at any time by dipping the chamber in water. This way the vial part can be used again with a new coverslip. It requires about half a day for the water glass

to dry, but an overnight waiting would be safer. Figure 2.10.b shows an FCS curve recorded with this chamber, and a fit similar to that of Figure 2.9.b.

2.4 Cryostat Setup

The cryostat setup, built for low temperature experiments, uses the confocal detection arrangement. A schematic drawing of the components is presented in Figure 2.11. When compared with the room temperature counterpart, the inverted microscope is replaced with a cryostat here, with some custom manufactured mechanical parts. Excitation source is a pulsed Ti:Sa laser with second harmonic generation extension (Coherent Chameleon Ultra II). Emission from the sample is sent either to a grating spectrometer (Princeton Instruments, SP2750 monochromator equipped with a PIXIS series camera), or to a pair of APDs (Perkin Elmer, SPCM-AQR-14; dark counts: 50 cps). There is also a halogen lamp and webcam assembly included to the setup for visual inspection of the sample, especially after the cryostat is closed.

Working at low temperature brings some limitations. The most severe one of these limitations is the impossibility to work with high NA microscope objectives, due to the fact that any immersion liquid would freeze at cryogenic temperatures. The relatively low NA air objectives are not suitable either. The thermal strains of the glue used in fixing their lenses were reported to cause misalignments in the objective [85]. As a solution to this limitation, aspheric lenses are commonly used in cryostats. They offer moderate NAs approaching to those of air objectives, and as being single-piece components, they don't pose any problems with alignment. However they cannot fully substitute a microscope objective, for they have no correction against chromatic aberrations. The low temperature setup described here also uses a 0.68 NA aspheric lens (Thorlabs C330TME). Another important limitation brought by low temperatures is encountered in positioning of the sample. The piezo stages similar to the one used in the room temperature setup are not suitable for operating at low temperatures. There are two solutions for this problem. One of them is to follow the beam scanning approach, and move the excitation beam rather than the sample, using steering mirrors located outside the cryostat. However in this case

the possible range of accessible area on the sample becomes quite limited ($\sim 100\mu\text{m} \times 100\mu\text{m}$ at best). Another approach is to move the sample again, using special kind of piezo actuators designed for low temperature applications. These actuators are based on the so-called inertial drive principle, which makes use of the velocity dependence of friction force to generate motion. The resulting motion occurs in the form of successive steps, with a specified minimum step size of 10nm at 4K. The travel range is 5mm; much larger than the one offered by laser scanning. The low temperature setup built as part of this thesis uses three of these actuators for moving the sample in three axes (Attocube systems, 2 ANPx101 and 1 ANPz101 positioners, driven by ANC300 controller). Unfortunately these positioners do not provide feedback about the actual position (i.e. there is no position sensor in the system), which when combined with a specified reproducibility of 5% in step sizes, makes confocal imaging almost hopeless. Therefore no programming effort has been taken for confocal imaging with the low temperature setup. Molecules are to be found by random trials guided by real-time spectrometer data.

The cryostat used in this setup is a pulse-tube cooler cryostat, which is a totally different system in comparison to traditional bath cryostats. In a bath cryostat, the sample and the related parts (optics, holders etc.) are all dipped into liquid helium, resulting in fast cooling. Thermal equilibrium is reached quickly and maintained as long as there is liquid helium in the cryostat. Liquid helium needs to be added as it boils away. In this design the cryostat is essentially an isolated container to house liquid helium. A pulse tube cooler on the other hand actively cools a metal part called cold finger, which is then brought into contact with the sample. It can be thought of as a refrigerator that uses helium (instead of a chlorofluorocarbon) as the working gas, and that has a special expansion valve with no movable parts. Helium is not consumed in this system; it is just being compressed and expanded continuously in a closed cycle. The compressor needs electricity and cooling water (for water-cooled version) to operate, but these are negligible in cost and obviously more abundant, when compared to liquid helium. Although pulse tube coolers are great in saving running costs, they offer limited cooling power. As a result of this, thermal contacts, load mass and isolation from room environment (maintained by vacuum) all

become crucial, and it takes considerably more time for the sample to reach the desired temperature, as compared to a bath cryostat. For the pulse tube cooler (Cryomech, cold head: PT405 RM, compressor: CP2800), vacuum system (Pfeiffer, DUO 2.5 and HiPace 80) and cryostat design (Cryoconcept) combination used in this study, it typically took ≈ 5 hours between vacuum start and reaching ≈ 6 K.

The above-mentioned differences regarding a pulse tube cooler cryostat caused some difficulties when developing the low temperature setup. One of them was related with cooling the sample. In a bath cryostat this is a relatively easy task, because everything is immersed in liquid helium. However in the pulse tube cooler, one needs to pay attention to all components and interfaces on the way from the cold finger to the sample. It turned out that the piezo positioners mentioned above had poor thermal conductivity (they were probably designed considering bath cryostats), which prevented efficient cooling and yielded a temperature of only ≈ 70 K on the sample. To overcome this problem, the positioners were bypassed by copper wire connections between the ceiling of the sample chamber and the sample holder. Although this ceiling is still an intermediate component between the cold finger and the sample, it was confirmed to be sufficiently cold (≈ 4 K). Making connections directly from the cold finger would require too much of a change on the initial design of the cryostat. The number and thickness of the copper wire connections became critical too. As the system cools down, these wires get harder than they are at room temperature. As a result of this change, when they were too many or too thick, they started blocking the positioners' motion. After some time-consuming trials, the wires were finally adjusted to allow for temperatures ≈ 6 K at the bottom of the sample holder (farthest point to the cold finger) without blocking the positioners. This final configuration is shown in Figure 2.12. Another difficulty was encountered with the sample. The terylene doped p-terphenyl films used for the preliminary measurements of the room temperature setup completely sublimated under the vacuum environment of the cryostat. This was a general problem, because nearly all the good matrices for low temperature single molecule experiments are small aromatic hydrocarbons similar to p-terphenyl, as shown in Table 2.4. Among these matrices, p-terphenyl was in fact the one that would be expected to

sublimate least easily (based on its higher boiling point). However it couldn't withstand the vacuum needed for pulse tube cooler ($\sim 10^{-4}$ mbar) for typical times required to reach cryogenic temperatures (3-4 hours). To overcome the sublimation problem, a second layer of film from a polymer was coated onto the p-terphenyl film. Due to its high molecular weight, a polymeric material does not sublime, and when made sufficiently thick, also preserves the underlying p-terphenyl molecules from breaking off from the film surface. The requirements here are that, this polymer should be soluble in a nonsolvent of p-terphenyl, should be transparent, and form smooth films when spin coated. Poly (vinyl alcohol) (PVA) dissolved in water was a good candidate regarding these issues. In first trials, it was observed that the PVA solution washed away the p-terphenyl film. Luckily, when waited sufficiently long between two coating steps (at least 30min.), this effect became less pronounced, leaving the p-terphenyl film intact in small regions. However it was again a challenge to find these regions when the cryostat was running.


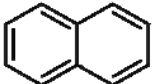
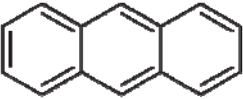
Molecule	Structure	Molecular weight (g/mol)	Melting point (°C)	Boiling point (°C)
p-terphenyl		230.30	212-213	389
naphthalene		128.17	80-82	218
anthracene		178.23	210-215	340

Table 2.4: Structure and relevant physical properties of common matrices used in low temperature single molecule experiments [86].

Despite all these difficulties, some data close to single molecule level could be recorded occasionally. As an example to these, a fluorescence spectrum recorded at 6K is

shown in Figure 2.13. Excitation was done at 517nm (vibronic excitation), and fluorescence was filtered by a bandpass filter (605/90). The sharp peaks between 575-580nm in this spectrum are limited by the resolution of the spectrometer, occurring to mind that they can correspond to ZPTs of individual terrylene molecules. These molecules are thought to be oriented to some extent parallel to the substrate and could be excited with the low NA aspheric lens. Their concentration was however too high to make the antibunching effect visible in the TAC histogram. If this were possible, detecting fluorescence from the ZPT using a narrow band filter would yield better SNR as compared to room temperature measurements. This idea has been exploited in [28,30] with another dye-host system (DBATT in n-tetradecane).

2.5 Conclusion

Various single molecule experiments allowed by the developed infrastructure have been demonstrated. These include wide-field imaging with standard (parallel) and TIRF excitation geometries, sample scanning confocal imaging, time-trace recording with synchronous and asynchronous detection modes, fluorescence lifetime measurements, fluorescence correlation spectroscopy in both aqueous solutions and organic solvents, and acquiring fluorescence spectra. Applications of these capabilities will follow in the next two chapters.

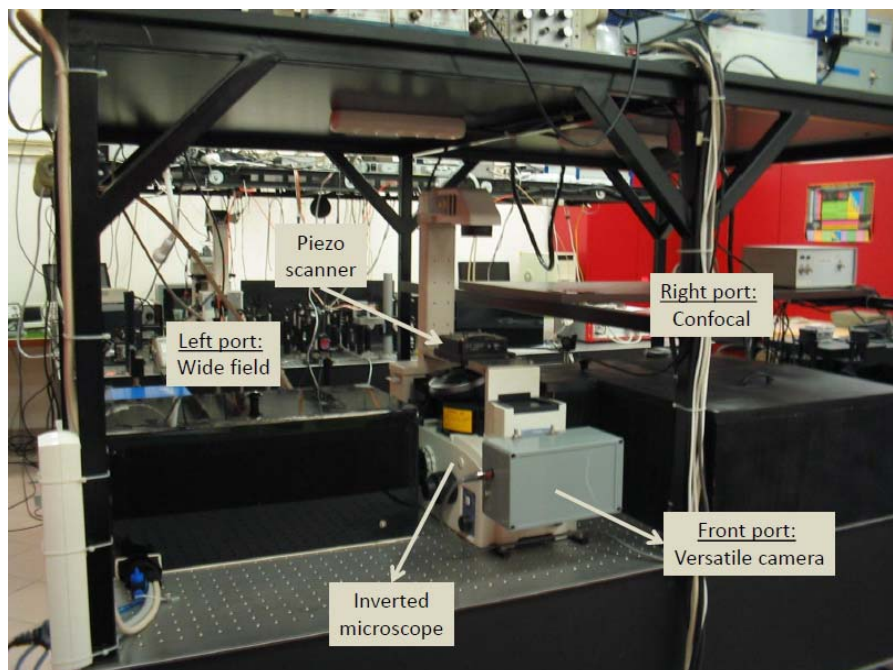


Figure 2.1: General overview of the room temperature setup.

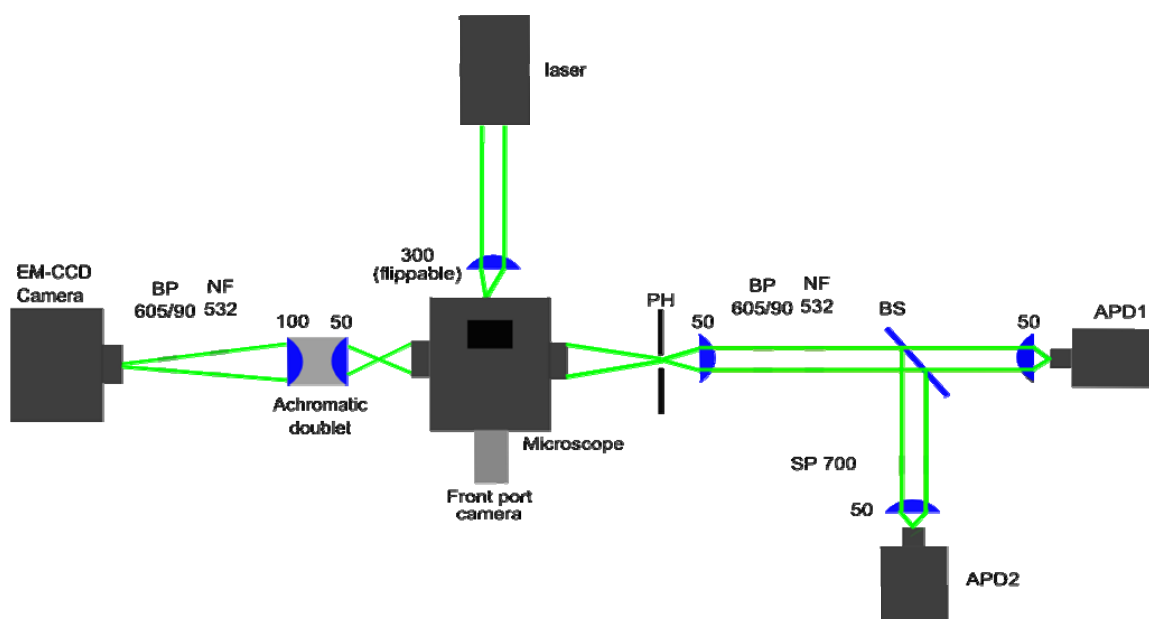


Figure 2.2: Schematic drawing showing components in the room temperature setup (BP: band pass filter; NF: notch filter; PH: pinhole; SP: short pass filter; BS: beamsplitter). BP 605/90 and NF 532 are used interchangeably between wide-field and confocal detection parts.

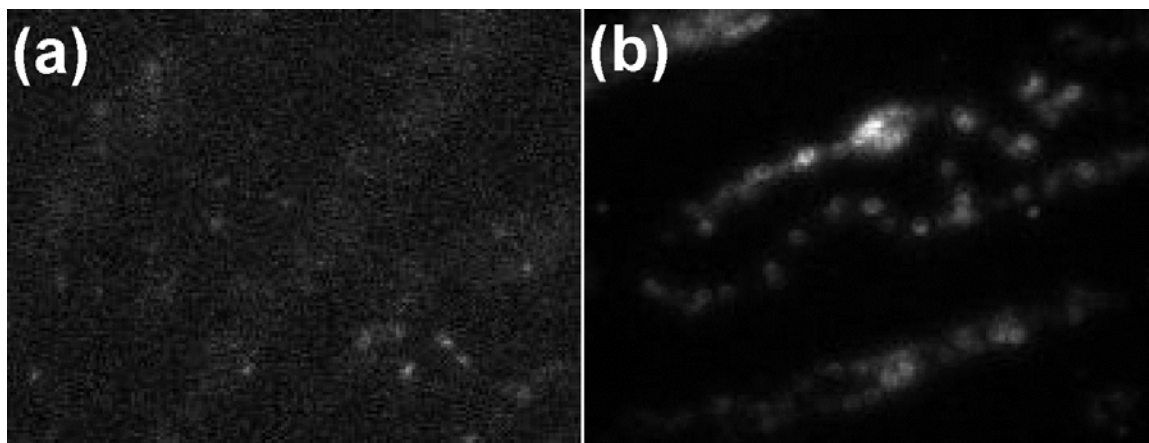


Figure 2.3: Wide field images of terrylene-doped p-terphenyl crystals taken under parallel- (a), and TIRF excitations (b). The vertical orientation of terrylene molecules to the substrate plane (parallel to the optical axis) prevents their excitation in (a), and makes them appear as doughnut shapes in (b).

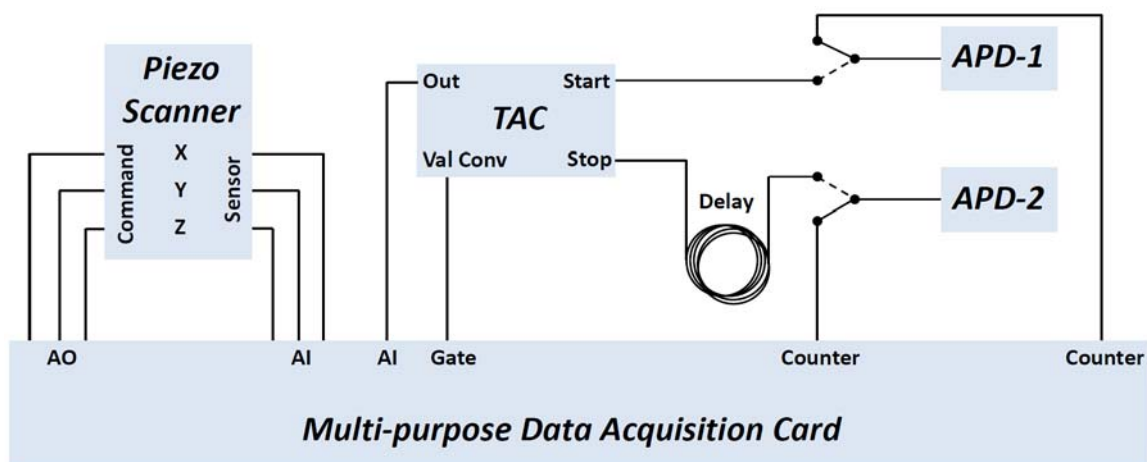


Figure 2.4: Hardware connections for the confocal detection part of the room temperature setup. APDs can be connected either to the card or the TAC (indicated by dashed lines).

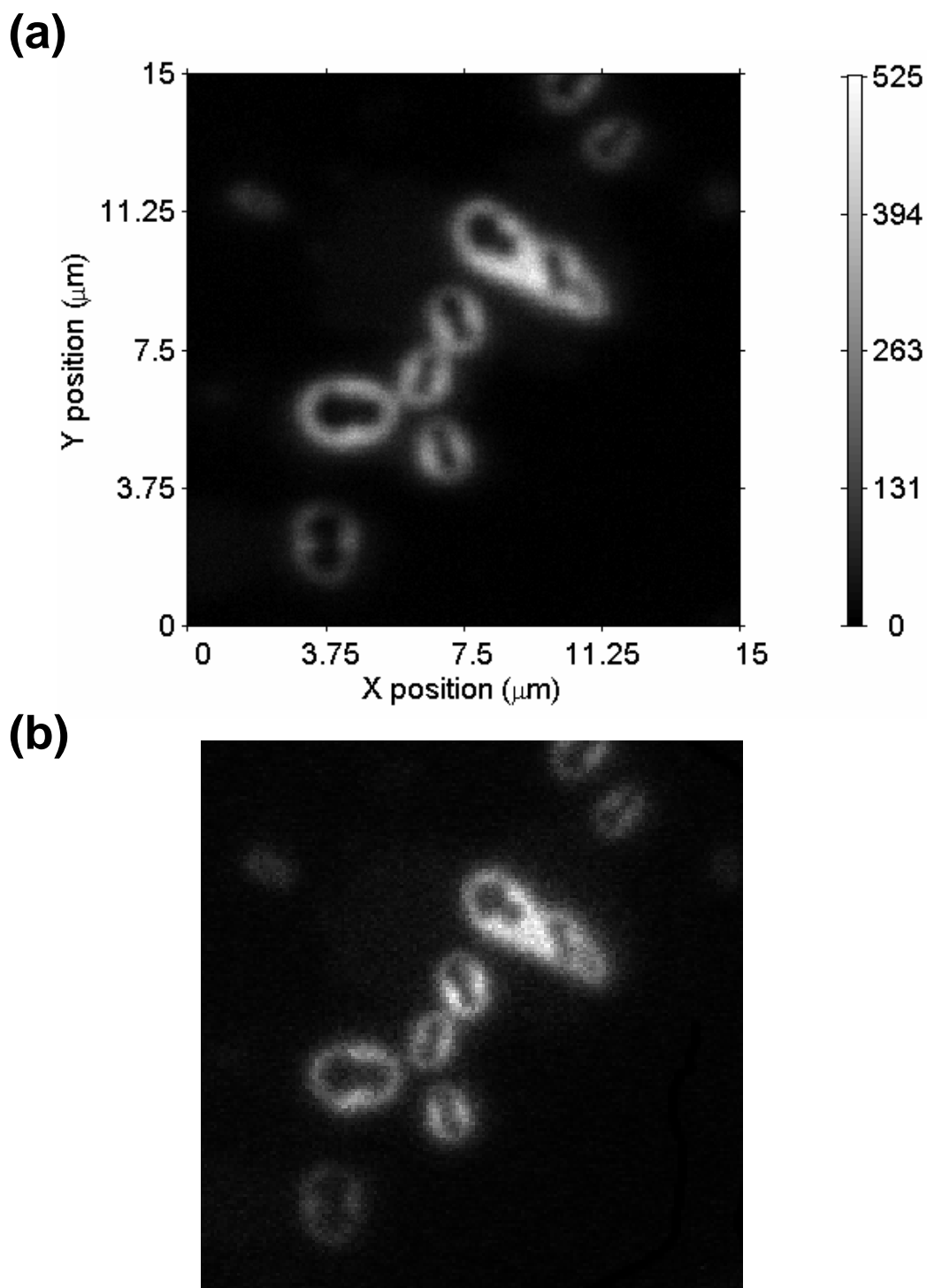


Figure 2.5: (a) Confocal image of DBT crystals on coverglass, recorded from a $15\mu\text{m}\times 15\mu\text{m}$ area with 300×300 pixels, and $0.5\text{ms}/\text{pixel}$ integration time. Colorbar indicates photons detected per pixel. (b) Detail cropped and rotated from a wide-field image, showing the same region as in (a).

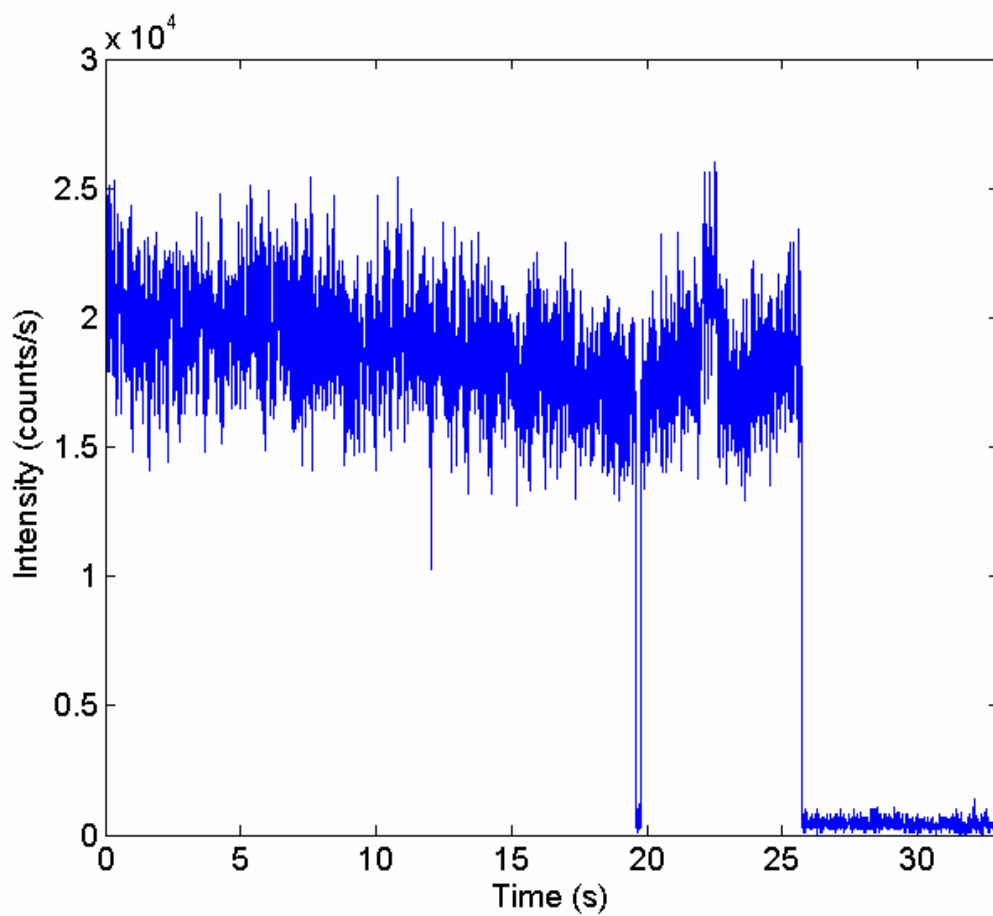


Figure 2.6: Fluorescence time trace of a single terrylene molecule in PMMA that exhibits blinking at $t \approx 19$ s, and photobleaches at $t \approx 26$ s.

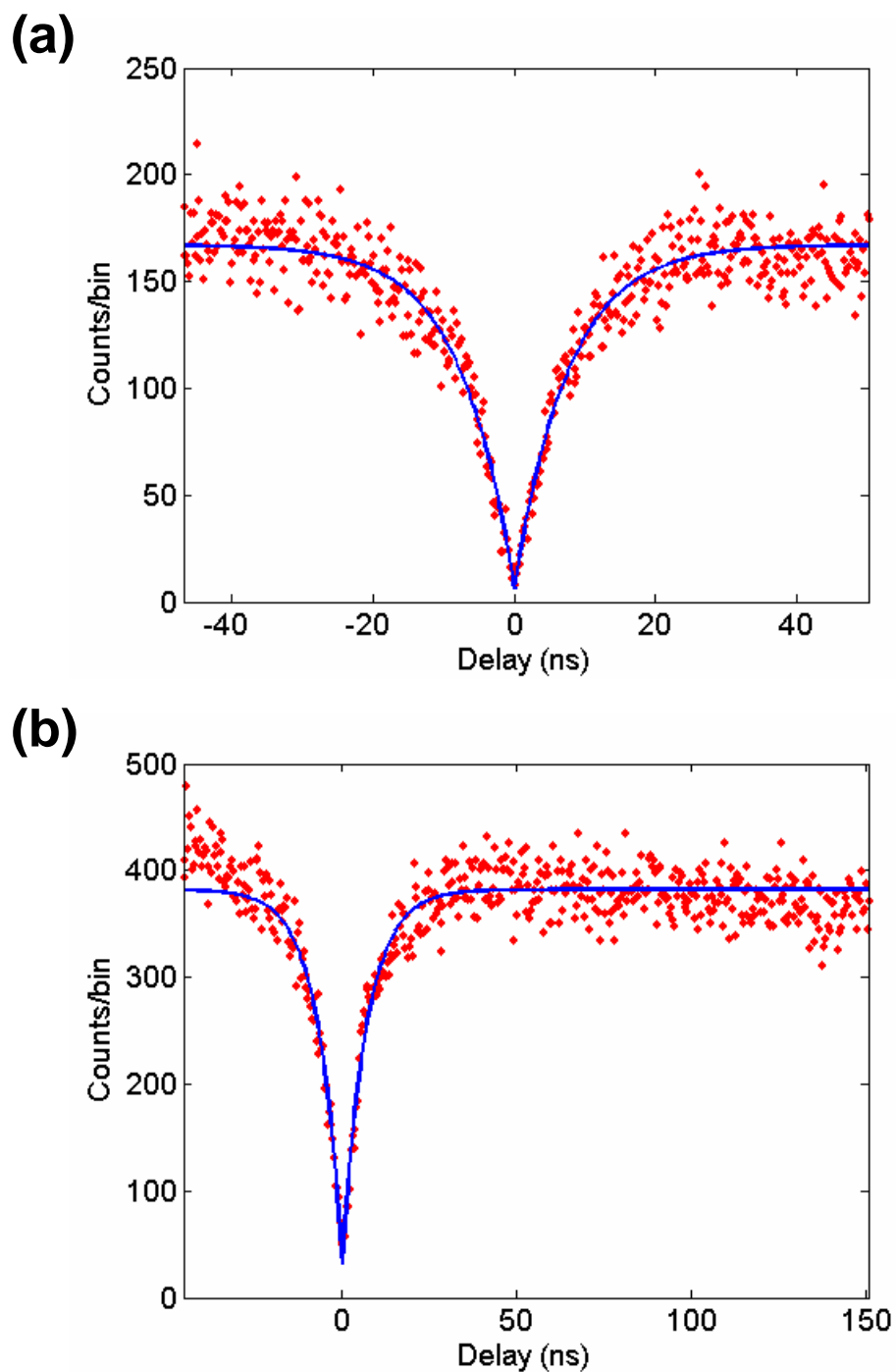


Figure 2.7: Representative TAC histograms recorded from single terrylene molecules in p-terphenyl. Blue line is a fit according to the exponential rise function of eq. (2.2) (see Table 2.2). The FSTL, acquisition time, and TAC rate were 100ns, 183.4s, and 382.2 Hz for the measurement of (a), and 200ns, 302.1s and 594.5Hz for that of (b).

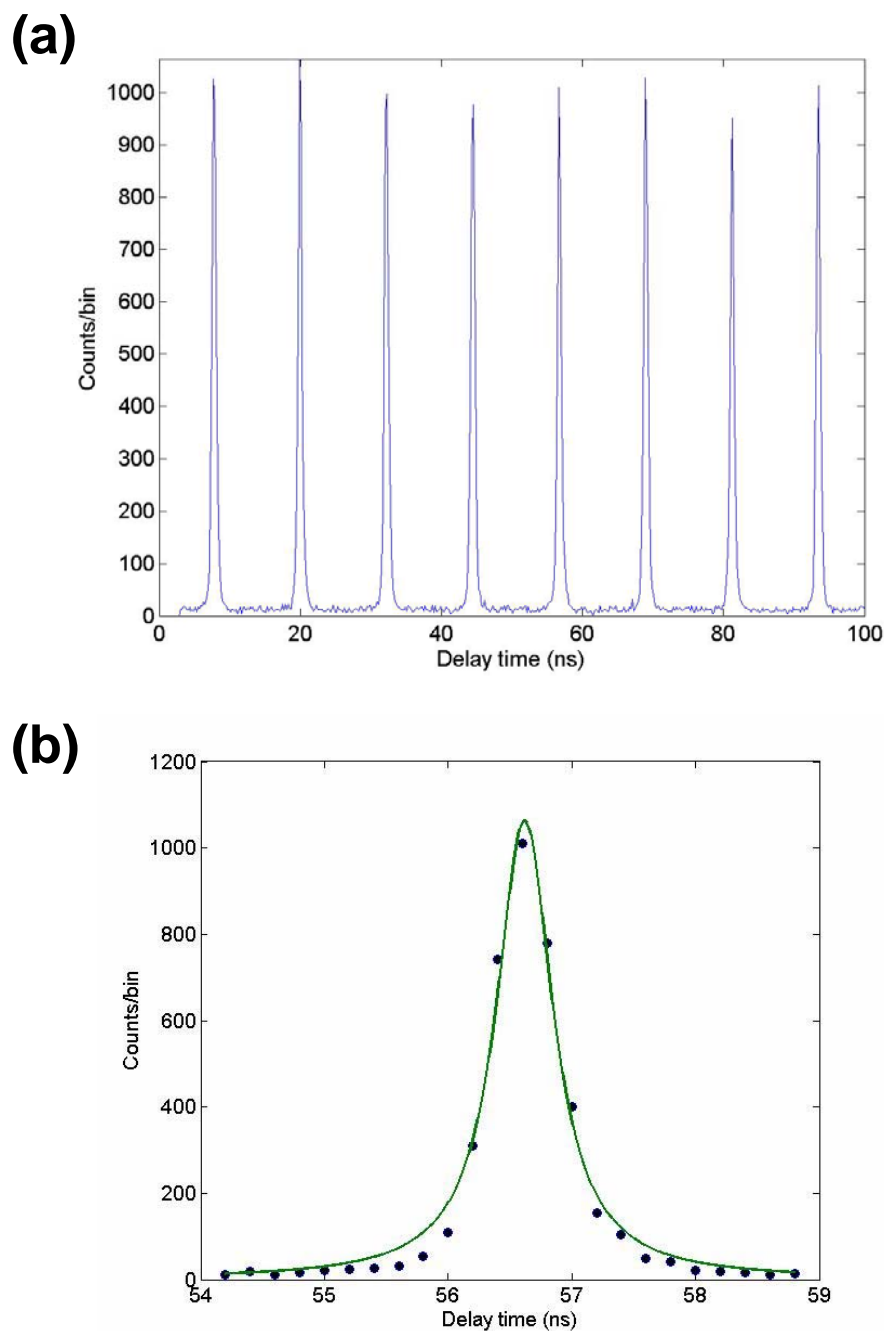


Figure 2.8: (a) TAC histogram showing the pulses of the subpicosecond Topica laser. 80MHz repetition rate of the laser appear as 12.5ns separation between histogram peaks. The histogram was plotted with 500 bins. (b) One of the peaks in (a) fitted with a Lorentzian function reveals the IRF as 555ps. TAC rate was 344Hz; APD rates were 79.7 and 50.4kHz; acquisition time was 104s.

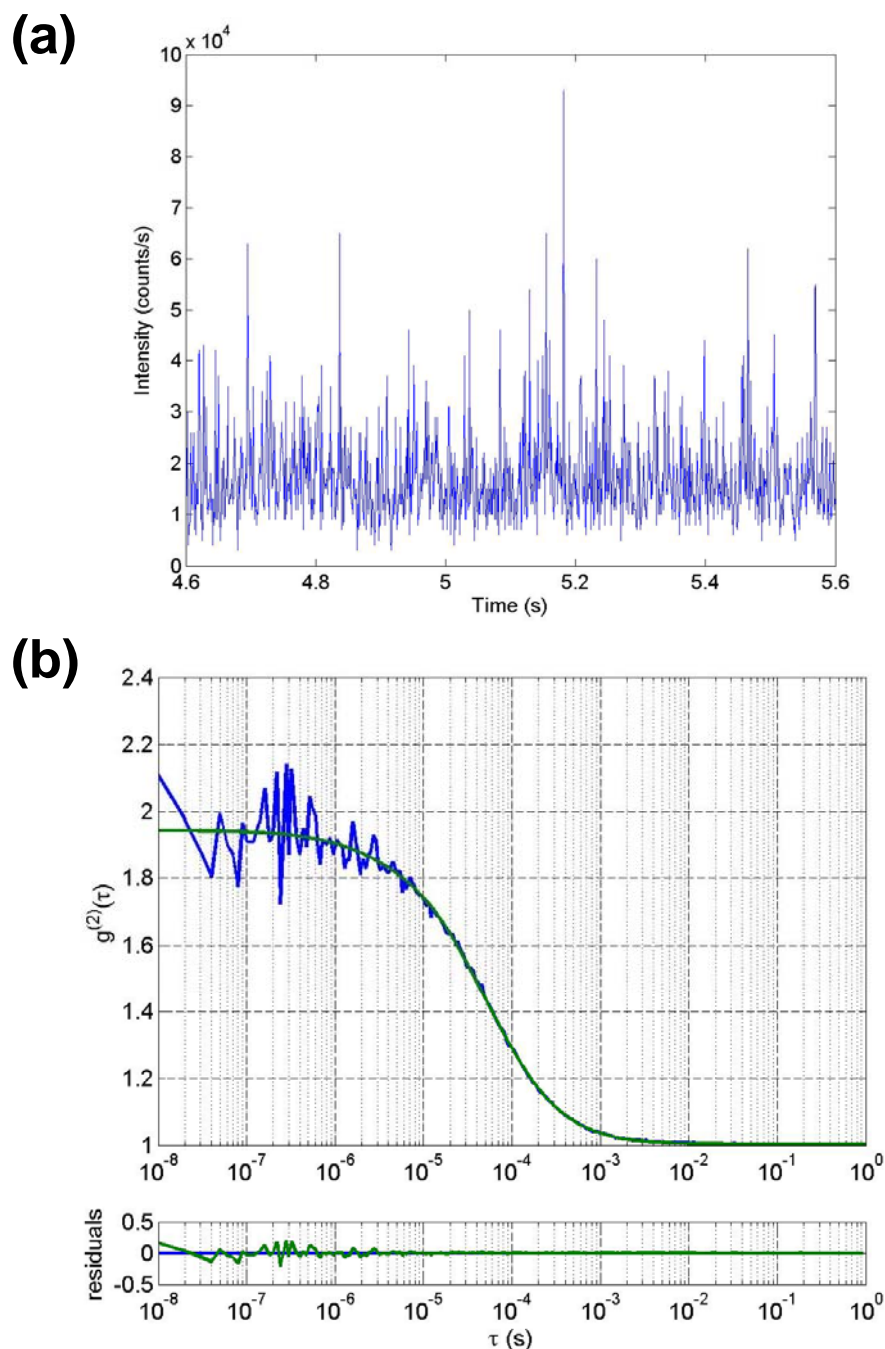


Figure 2.9: (a) 1s section from a 120s-long FCS time trace, recorded from a 0.1nM Rhodamine B solution in water. Passing of molecules through the confocal probe volume appear as spikes in the time trace. The typical width of the spikes is expressed by τ_D of eq. (2.5). (b) $g^{(2)}(\tau)$ (blue line) calculated from the time trace in (a), and a fit according to eq. (2.5) (green line). Owing to asynchronous acquisition, the analysis can address events occurring on a wide timescale starting from 10ns.

(a)



(b)

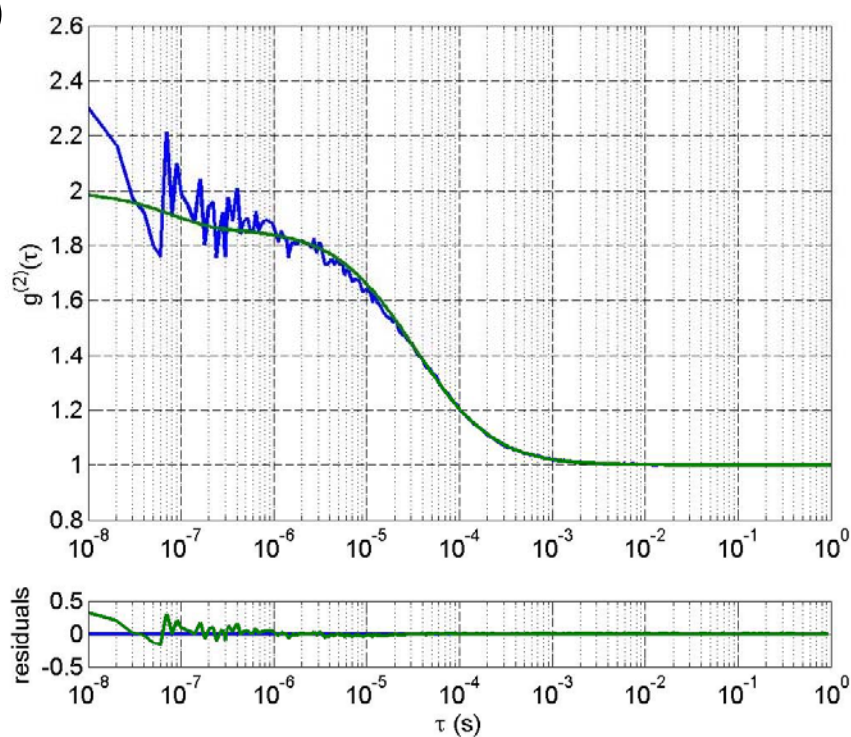


Figure 2.10: (a) Chamber built for FCS analysis of dye molecules in organic solvents. The upper half of a cut vial and a standard glass coverslip are fused together by water glass. (b) FCS curve (blue line) from dilute terrylene in toluene solution. Time trace was recorded with a 1.49 NA oil objective, 2-3 μm above the coverslip. Acquisition time was 120s, with APD rates 10.26kHz and 10.80kHz. The same fitting procedure as in Figure 2.9.b yields $T = 0.14$, $\tau_T = 80\text{ns}$, $A = 1.00$, $\tau_D = 32.9\mu\text{s}$, $\kappa = 5.22$, and $g_\infty = 1.00$.

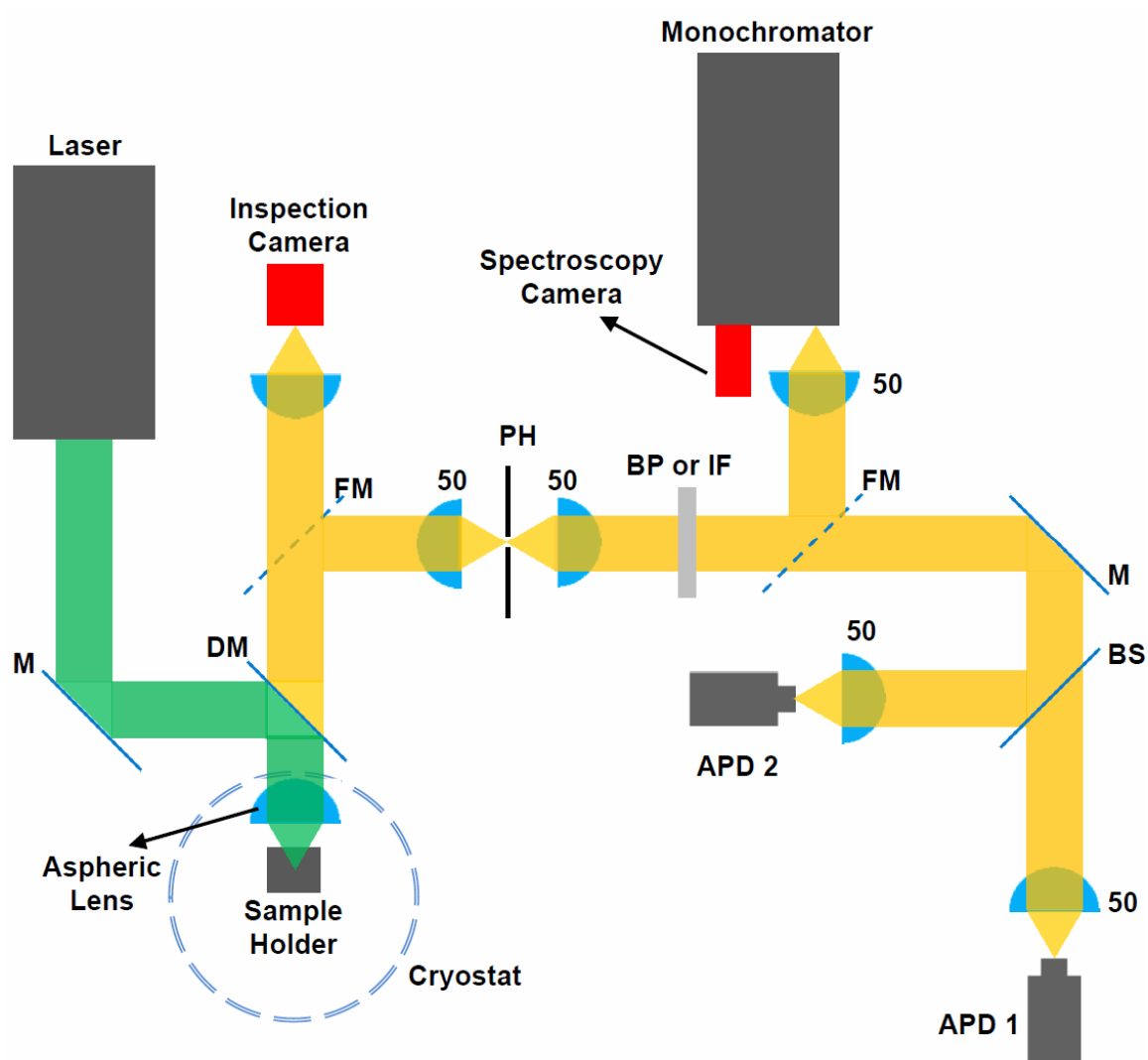


Figure 2.11: Schematic drawing of the cryostat setup.

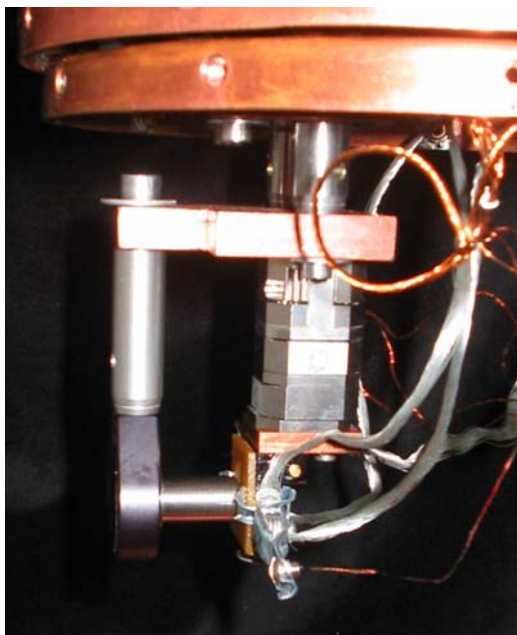


Figure 2.12: A photograph from inside the sample chamber showing copper wire connections.

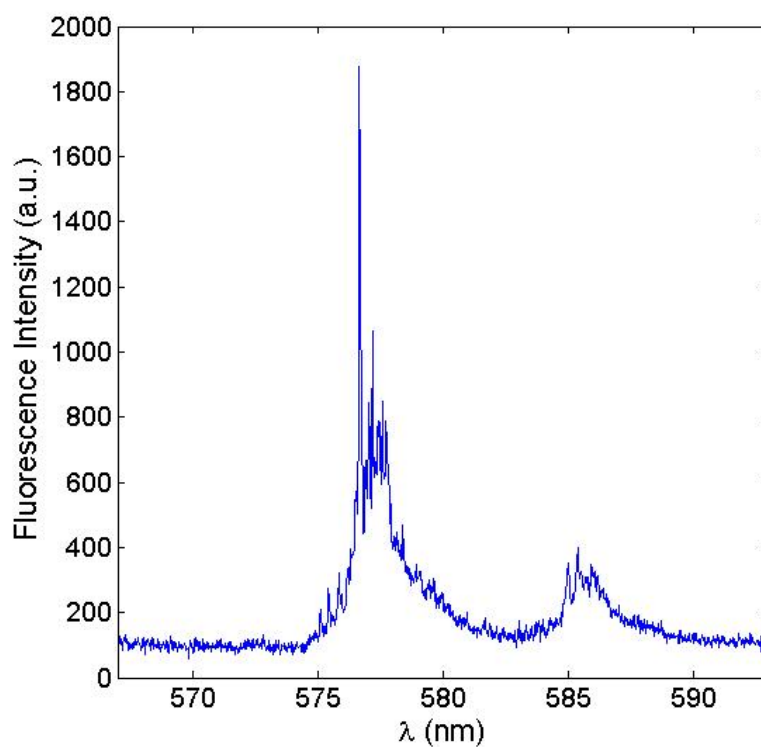


Figure 2.13: Low temperature fluorescence spectrum of dilute terrylene molecules embedded in p-terphenyl, recorded at 6K.

Chapter 3

TERRYLENE – ANTHRACENE AS A NEW DYE – HOST SYSTEM

3.1 Introduction

Fluorescent dye molecules embedded in host matrices have been the system of choice for many quantum optical demonstrations including photon antibunching [15, 41,87], two-photon interference [26,27,29,31], and guided emission [45,53]. In these systems, both the dye and the host are critical for optical properties such as photostability, saturation emission rate, and orientation of the transition dipole moment.

Despite their widespread use over the last two decades, there are only a limited number of dye–host pairs with desirable optical properties. This makes any new combination to be welcomed in hopes of extending the range of possible experiments [18,20,42,88]. A relatively recent example is the DBT-anthracene system, which was first introduced by Orrit and coworkers [42], and paved the way for many other interesting demonstrations [19,29,43-45,89].

The DBT-anthracene system was in fact chosen following some unsuccessful trials with terrylene-anthracene [90,91]. Motivated by studying conduction in organic crystals, Orrit et al have initially investigated the terrylene-anthracene system at cryogenic temperatures, but the fluorescence signal they could obtain was surprisingly low. They attributed this to a new type of intersystem crossing event that also involves the host triplet state (intermolecular intersystem crossing), and occurs when the first excited electronic state of the dye is located energetically higher than the triplet state of the host. Based on this explanation, they turned their attention to another dye, DBT, which has its first excited electronic state lower than the anthracene triplet.

As of the preparation of this thesis, [90,91] have been the only reports of terrylene in anthracene at the single molecule level. Considering that these were low temperature studies, the terrylene–anthracene system has never been explored at room temperature. The present chapter aims to fill this gap by presenting single molecule measurements obtained from spin-cast films of terrylene-doped anthracene.

Spin coating has long been shown to be a possible method for obtaining thin films of anthracene [92]. However its use in single molecule experiments to obtain thin films of dye-doped molecular crystals was due to Sandoghdar and coworkers, who have successfully developed the procedures for terrylene in p-terphenyl [66], and DBT in anthracene [89]. In comparison to the traditional sublimation method, their spin coating procedure greatly facilitates sample preparation, reduces material costs, and allows for much thinner films. They have also reported a preferential orientation of the dye molecule within the host crystal, being perpendicular to the substrate for terrylene in p-terphenyl, and parallel for DBT in anthracene.

The work described in this chapter also uses spin coating to obtain terrylene-doped anthracene films, and characterizes their optical properties at room temperature through single molecule measurements. Following this introduction, Section 2 continues with a description of the experimental details. Results are discussed in Section 3 with emphasis on characterizing the general properties of the system, and quantifying its performance. Section 4 finally summarizes the chapter.

3.2 Experimental

Terrylene-doped anthracene films were obtained following the same procedure in [89], except for using terrylene instead of DBT. The solution used for spin coating contained 2.6 mg/ml anthracene and ~100 nM terrylene in a 100/1 (by volume) mixture of diethyl ether/benzene. This was coated onto glass coverslips with a commercial spin coater (Specialty Coating Systems, P6700), at a speed of 3000 rpm for 30 s, followed by 1500 rpm for 20 s. Prior to coating, the coverslips were cleaned with a UV-Ozone cleaner (Jelight Company, 42-220) for 10 minutes.

Films prepared this way were then characterized using the room temperature confocal setup described in Section 2.2. A 1.49 NA oil immersion objective (Nikon, TIRF Apo 60x) was used with 90x total magnification. Excitation was done at 532 nm either with the subpicosecond pulsed laser, or the cw diode laser (mentioned in Section 2.2), and using a suitable dichroic mirror (Chroma, z532/1064rpc). All the values of excitation power to be mentioned hereafter were measured at the objective nosepiece of the microscope with a wide-area detector (Thorlabs, S120B). A half waveplate (Thorlabs, WPMH05M-532) mounted on a custom-made motorized holder was used to rotate the polarization of the excitation beam, where necessary. Similarly, a polarizer (Melles Griot PSP-450-750-10) mounted on a more precise but slower rotation stage (Standa) was used for polarization dependent analysis of emission.

The collected light from the sample was sent either to a pair of avalanche photodiode detectors, or to a monochromator (Princeton Instruments, SP2750; focal length: 750 mm, grating: 300 groves/mm) equipped with a spectroscopy camera (Princeton Instruments, PIXIS eXcelon-100B), located on different ports of the microscope. Detection with APDs was done as described in Section 2.2, with an appropriate choice of notch (Chroma, ZET532NF), bandpass (Chroma, HQ605/90M), and short-pass (Thorlabs, FES0700) filters (same combination as shown in Figure 2.2). For recording spectra, a long-pass filter (Thorlabs, FEL0550) was placed at the entrance of the monochromator to reject the red tail of the laser that coincided with the spectral window in our measurements.

3.3 Results and Discussion

A representative confocal fluorescence image of terrylene molecules in anthracene film is shown in Figure 3.1. The image is $4 \times 4 \mu\text{m}$ in size, consists of 100×100 pixels, and was acquired with 1ms/pixel integration time under an excitation power of $10 \mu\text{W}$. The bright features in this image are candidate locations for individual terrylene molecules. Being $\sim 1\text{nm}$ in size, a terrylene molecule should act as a point source, and reveal the diffraction-limited waist of the excitation beam at the focal plane. The

intensity profile along a line drawn through one of these features (marked by A-B) is plotted in the inset. A Gaussian function fitted to this profile gives a FWHM of 223nm, in agreement with a confocal single molecule image at the given excitation wavelength. The varying intensity of the features is attributed to different orientations of terrylene molecules within the host. Molecules with their transition dipole moments parallel to the (linear) excitation beam polarization vector are excited more efficiently.

In order to verify that the bright features in Figure 3.1 correspond to individual terrylene molecules, one of them (marked by C) was positioned onto the focal spot, and a fluorescence spectrum (Figure 3.2.a) and a TAC histogram (Figure 3.2.b) were recorded from it. Both data were recorded for 1min, and with the same excitation power as in scanning. The background correction for the spectrum was done in the most direct way by recording a second spectrum at an empty position (marked by D) with identical conditions (i.e. with the excitation laser on), and subtracting this from the source spectrum recorded at point C. The resulting fluorescence spectrum given in Figure 3.2.a shows a peak emission wavelength of 579.3nm and a phonon sideband around 630nm, indicating that the detected photons come from terrylene. On the other hand, the antibunching effect that appears as a missing peak at the zero delay time of the TAC histogram in Figure 3.2.b is characteristic for a single emitter. Noting that these two data were collected from the same position, one can conclude that the bright features in the confocal image of Figure 3.1 truly correspond to single terrylene molecules.

To calculate the fluorescence lifetime of terrylene in anthracene, the data of Figure 3.2.b was fitted with the following model

$$C(\tau) = \sum_n A_n e^{-\frac{|\tau-nT|}{\tau_F}}, \quad (3.1)$$

where $C(\tau)$ is the coincidence counts, τ is the delay time, τ_F is the fluorescence lifetime, T is the time between consecutive laser pulses, and n and A_n are the order and weight of the peaks [32]. Using this model, the fluorescence lifetime for the molecule of Figure 3.2.b was obtained as $\tau_F = 3.0$ ns. The same analysis made over 41 individual molecules resulted in an average of $\tau_F = 3.6 \pm 0.5$ ns. Fluorescence lifetime was also determined

under cw excitation. Figure 3.3 shows a representative TAC histogram for this case, fitted with eq. (2.2) to yield $\tau_F = 2.8\text{ns}$. Similarly, the same analysis made over 17 molecules resulted in an average of $\tau_F = 2.7 \pm 0.6\text{ns}$. As mentioned in Section 2.3.3, measuring τ_F from cw TAC histograms is likely to yield shorter values due to pumping rate effect, and the τ_F obtained using pulsed excitation is therefore more reliable. This was in fact in good agreement with the value of $3.15 \pm 0.1\text{ns}$ reported in [90,91], and significantly shorter than fluorescence lifetimes observed with other hosts [93].

In order to gain insight about the orientation of terrylene molecules in the spin-cast anthracene films, a polarizer was mounted into the detection path, and the fluorescence intensity of a single molecule was observed as the polarizer rotated. As shown in Figure 3.4, the fluorescence intensity exhibited a clear cosine-square dependency on the polarizer angle (trace A). As the calculations in [94] show, in collecting fluorescence of a single molecule located at the focal point of an objective, the fluorescence polarization across the collimated beam depends on the orientation of the transition dipole moment of the molecule. When the transition dipole moment lies within the focal plane, the fluorescence becomes polarized predominantly along the axis of the transition dipole and varies little across the collimated beam (the variations occur at the edge of the beam and become more pronounced with increasing NA). On the other hand, when the transition dipole moment is parallel to the optical axis, the fluorescence polarization vector is directed radially at every point across the collimated beam. According to these numerical results, the high modulation depth of trace A in Figure 3.4 indicates that the terrylene molecules are oriented such that their transition dipole moments are mainly parallel to the plane defined by the anthracene film (i.e. perpendicular to the optical axis). A similar in-plane orientation has been observed also for single DBT molecules in anthracene [89], and shown to be a desired property in a microcavity design [45]. The same measurement was also carried at an empty position within the host crystal, $0.8\ \mu\text{m}$ away from the molecule (trace B). This provided the background level present in the former single molecule data. The background count rates remained lower than the dip of the modulating single molecule fluorescence,

suggesting that the transition dipole moment is not perfectly in-plane with the anthracene film. It should be noted that the same observation (i.e. dip of trace A remaining above trace B) can also be interpreted as an ellipticity in fluorescence polarization introduced by oblique elements in the detection path such as beamsplitter or port selection prism [95]. Nevertheless even in the presence of an artifact, one can still ignore any depolarization and attempt to quantify the out-of-plane component as if the not-perfect modulation were completely due to dipole orientation. The result in this case becomes an upper bound for the angle between a terrylene molecule and the film plane. To carry this analysis, the out-of-plane component was quantified following the method proposed in [94]: The background-subtracted count rates (trace B subtracted from trace A) were used to read the fluorescence intensities corresponding to cases when the polarizer axis is parallel, at 45°, and orthogonal to the transition dipole moment as 160, 97, and 24kHz respectively. Then, using these intensities in eq. (6-8) of [94], the transition dipole moment was calculated to be out of plane by at most 28°. The same analysis carried over 21 single molecules and respective background data resulted in an average value of $35 \pm 11^\circ$.

As a next step for characterizing the terrylene-anthracene system, fluorescence saturation curves were recorded from single molecules. Figure 3.5 shows one such curve, where the background-subtracted signal (red squares), and the background (red squares) are plotted as a function of the excitation power. The background rates were recorded at the same position as the molecule, after the molecule has photobleached. The fluorescence rates were fitted using the well-known saturation model

$$S(P) = S_\infty \frac{P / P_{sat}}{1 + P / P_{sat}}, \quad (3.2)$$

where S is the fluorescence detection rate, P is the excitation power, P_{sat} is the saturation power, and S_∞ is the fluorescence detection rate at saturation [44]. The fit yielded $P_{sat} = 60\mu\text{W}$, and $S_\infty = 754\text{kHz}$, which were moderate values considering several other terrylene molecules analyzed similarly.

It is interesting to note that this typical S_{∞} value obtained at room temperature is orders of magnitude higher than the one reported by Orrit and coworkers at cryogenic temperatures ($\approx 750\text{kHz}$ versus $\approx 300\text{Hz}$) [90,91]. Although the oil immersion objective used in the present experiments brings some clear advantages over an aspheric lens, the discrepancy is still too large to be attributed to numerical aperture of the lenses alone. Looking for another explanation, one can think of the orientation of terrylene molecules within the host crystal, which may have significant influence on the collection efficiency. However, the possibility of an unfavorable orientation was already addressed in [91], and ruled out based on control experiments with another host, naphthalene. In addition to their conclusion, it is worth pointing out the similarity between sublimation-grown [91] and spin-cast [92] anthracene films, both of which were reported to extend along the (a,b) plane. A similar morphology has also been observed for crystals obtained from solution [96] and vapor phase [97] as well, indicating that one should not expect a dramatic change in molecular organization within anthracene films prepared by different methods. Consequently, the anthracene morphology that favored in-plane orientation of terrylene molecules in spin-cast samples was most probably also present in [90,91]. Furthermore the same group also studied DBT in anthracene, prepared by the same sublimation method, and demonstrated nice dependency of single molecule fluorescence on excitation polarization [43]. Had there been problems originating from sample preparation such as dye orientation, film thickness, or birefringence, they would have difficulty with the DBT-anthracene system as well. Consequently, the above comparison leaves temperature as the only source of difference that can explain the two contrasting S_{∞} values. The intermolecular intersystem crossing mechanism proposed by Orrit et al may be a temperature dependent event caused by changes in the energy level of the host triplet state.

At this point it would be interesting to calculate the intersystem crossing yield at room temperature. This has been done via correlation analysis, following the procedure in [91]. Figure 3.6 shows the autocorrelation function, $g^{(2)}(\tau)$, calculated from intensity

versus time data of a single terrylene molecule with $P = 10\mu\text{W}$ excitation power and 30s acquisition time (red diamonds). The autocorrelation function was fitted with a mono-exponential model $g^{(2)}(\tau) = 1 + Ce^{-\lambda\tau}$, yielding a contrast of $C = 0.071$, and a decay parameter of $\lambda = 7 \times 10^5\text{Hz}$ (blue line). The population and depopulation rates of the triplet state, denoted by k_{23} and k_{31} respectively, were then calculated from the fit parameters using relations

$$C = \frac{\lambda - k_{31}}{k_{31}}, \quad (3.3)$$

and

$$\lambda = k_{31} \left[1 + \frac{P/P_{sat}}{1 + (2k_{31}/k_{23})(1 + P/P_{sat})} \right], \quad (3.4)$$

where P_{sat} was taken as $60\mu\text{W}$ based on the analysis of Fig. 3.5. The obtained k_{23} and k_{31} rates were 1×10^6 and $6.8 \times 10^5\text{Hz}$ respectively. In comparison to the values reported at cryogenic temperatures in [91] ($k_{23} = 1.0 \pm 0.5 \times 10^6$ Hz, $k_{31} = 1.8 \pm 0.3 \times 10^3$ Hz), one can see that the triplet state is populated with almost the same rate, whereas the depopulation rate k_{31} is much faster for the room temperature case. Noting the strong relation between k_{31} and λ , it would be safer to confirm that the observed decay in the autocorrelation function was not an artifact due to other effects such as laser intensity fluctuations. For this, the autocorrelation function of the laser beam reflected from an empty coverslip was calculated, and observed to be distributed symmetrically around $g^{(2)}(\tau) = 1$, as expected (data not shown). A TAC histogram recorded from the same molecule is presented in the inset of Figure 3.6; using this histogram, the fluorescence lifetime was fitted to be $\tau_F = (k_{21} + k_{23})^{-1} = 3.6\text{ns}$, using the same model as in Figure 3.2.b. The intersystem crossing yield was then calculated as $k_{23}/(k_{21} + k_{23}) = 4 \times 10^{-3}$, which is comparable to its reported low-temperature value of $(3 \pm 2) \times 10^{-3}$ [91].

Finally, the issue of photostability of the terrylene-anthracene system was addressed through statistical analysis of intensity-versus-time data recorded from individual molecules, as suggested by [98,99]. Since the survival time of a molecule depends on the excitation intensity, and blinking events impose difficulties in quantifying it, the

number of photons detected before bleaching was used as the measure of photostability. To ensure equal excitation efficiency for all azimuthal orientations of the molecular transition dipoles, a half-waveplate was mounted into the excitation path, and rotated at an angular frequency of ≈ 1.7 Hz. This resulted in a temporally modulated fluorescence signal, which provided an extra indication of single molecule observation in addition to one-step photobleaching. Figure 3.7 shows the probability distribution of the number of photons detected before bleaching, obtained from a set of 104 molecules (red squares). The distribution could not be fitted by mono- or bi-exponential decays, indicating some degree of heterogeneity within the studied molecular population. A tri-exponential fit yielded the characteristic numbers of detected photons as 1×10^4 , 3.3×10^5 and 3.6×10^6 , with weights 0.19, 0.37 and 0.44 respectively. It is not clear if this heterogeneity is inherent to the terrylene-anthracene system, or related to sample preparation. The weighted average for the characteristic number of detected photons is 1.6×10^6 , which must be sufficient for most of the single molecule experiments.

3.4 Conclusion

This chapter appraised the potential use of terrylene-doped anthracene thin films for single molecule experiments at room temperature. The short fluorescence lifetime, mostly in-plane orientation, high detection rate at saturation, fast triplet state depopulation rate, and fair photostability all make this system a good candidate. The results presented here are expected to be beneficial also for further studies on the intermolecular intersystem crossing mechanism.

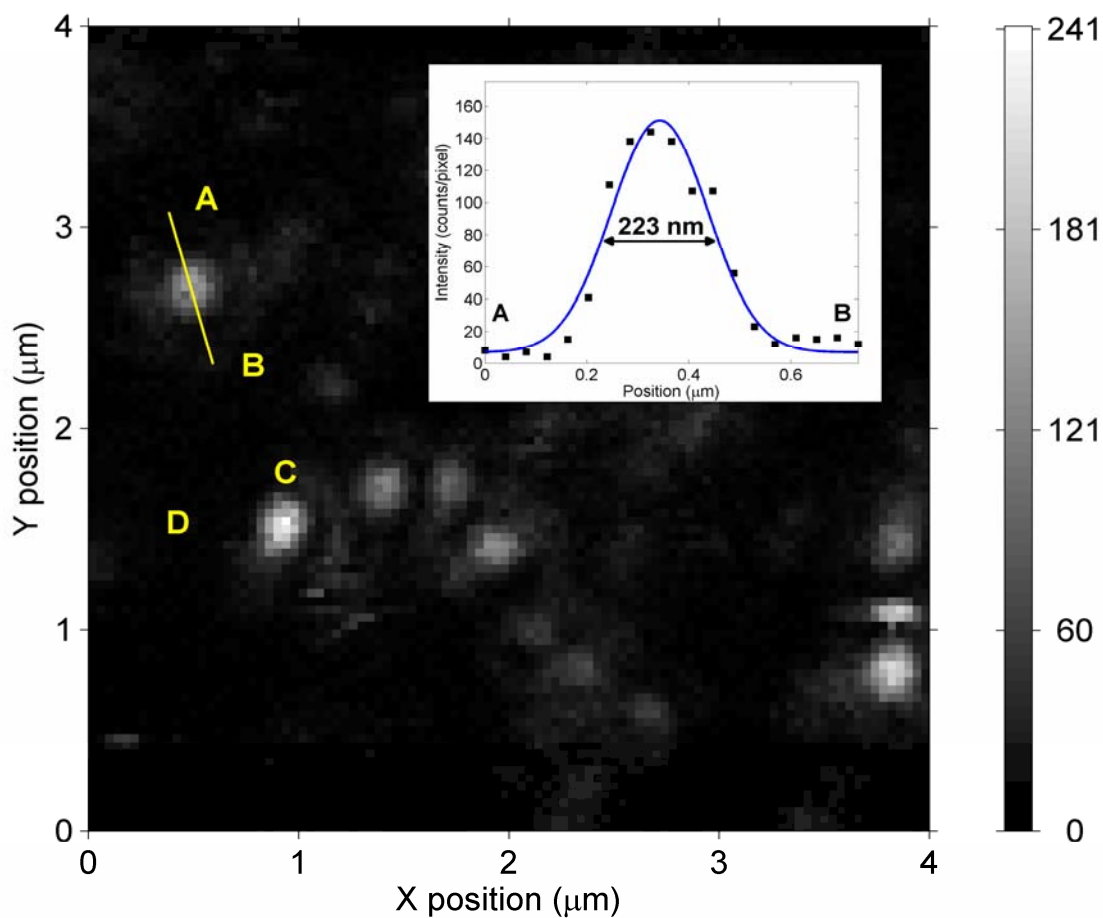


Figure 3.1: Confocal image of individual terrylene molecules in anthracene, recorded from a $4\mu\text{m}\times 4\mu\text{m}$ area with 100×100 pixels, and $1\text{ms}/\text{pixel}$ integration time. Excitation power was $10\mu\text{W}$. Inset shows the intensity profile (black squares) taken along the center of the upper left molecule, and a Gaussian fit (blue line) to it. Width of the Gaussian function is 223nm , in agreement with the diffraction limited resolution. The colorbar designates the number of photons detected per pixel.

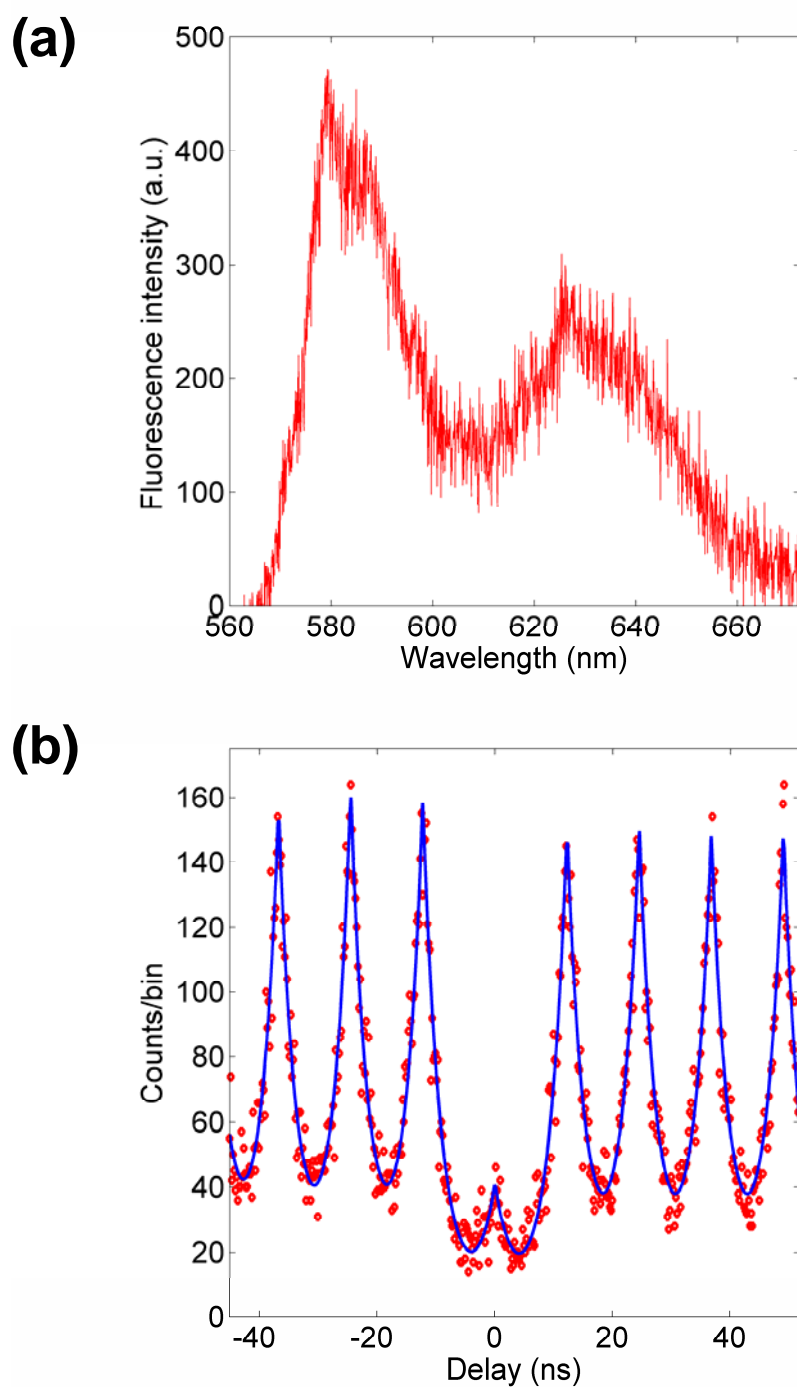


Figure 3.2: (a) Fluorescence spectrum recorded from one of the bright features (marked by C) in the confocal image of Figure 3.1. (b) TAC histogram (red diamonds) recorded from the same position, and fitted with the exponential model described in the text (blue line). TAC rate was 537Hz.

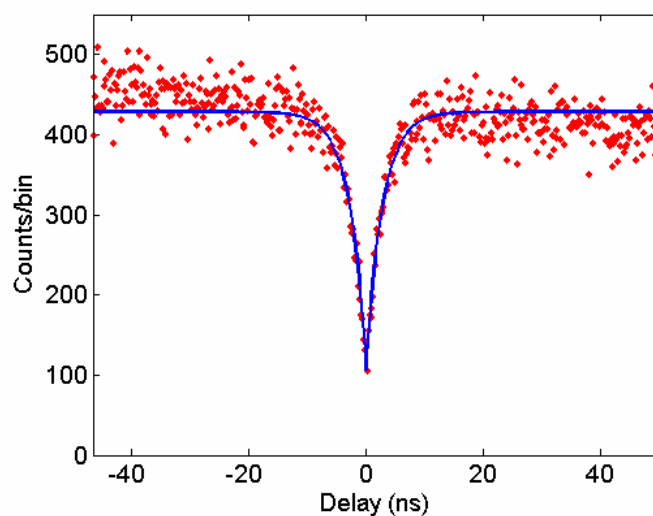


Figure 3.3: TAC histogram (red diamonds) recorded from a single terrylene molecule, fitted with the model of eq. (2.2) to yield $\tau_F = 2.8\text{ns}$ (blue line). TAC rate and acquisition time were 3228Hz, and 63s respectively.

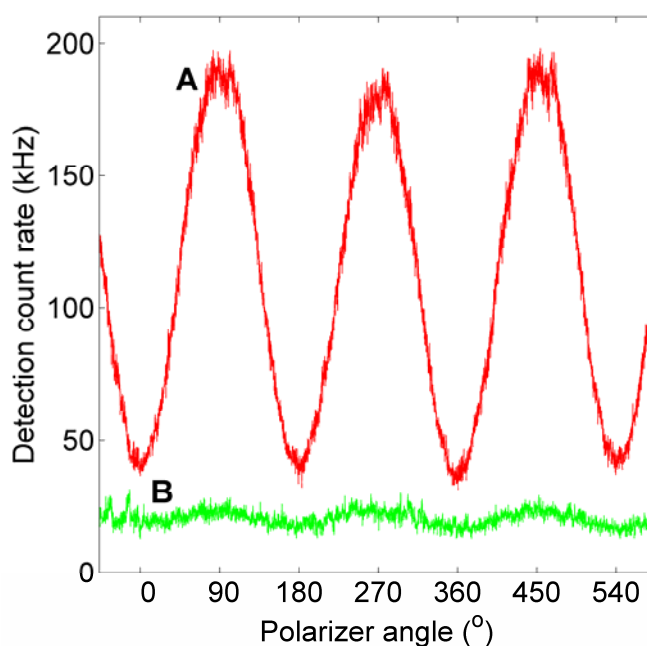


Figure 3.4: Detection rate as a function of the polarizer angle, recorded from a single Terrylene molecule (trace A; red), and an empty position within the anthracene crystal (trace B; green). The high modulation depth is an indicative of the parallel orientation of the transition dipole moment with respect to the substrate plane. Excitation power was $55\mu\text{W}$ for both measurements. Integration time of the original intensity versus time data was 10ms.

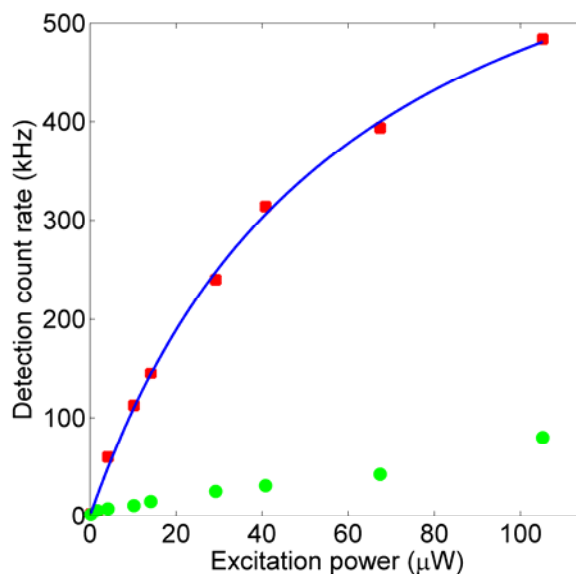


Figure 3.5: Detection rates for the fluorescence of a single terrylene molecule (red squares) and the background (green circles) plotted as a function of the excitation power. The fluorescence signal is fitted to a standard saturation model to yield a detection rate at saturation of $S_{\infty} = 754\text{kHz}$ (blue line).

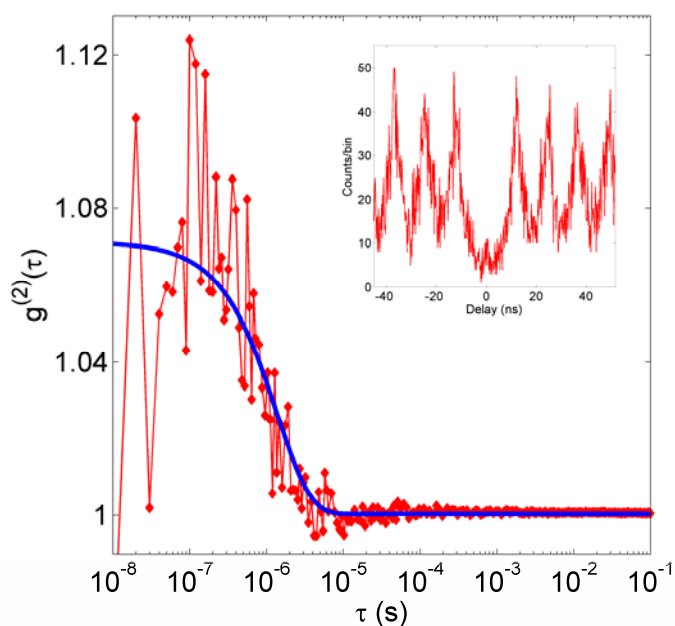


Figure 3.6: Intensity autocorrelation function of a single terrylene molecule (red diamonds), fitted by an exponential decay function (blue line). Excitation power was $10\mu\text{W}$, corresponding to a total count rate of 137kHz on the APD's. A TAC histogram recorded from the same molecule is shown in the inset.

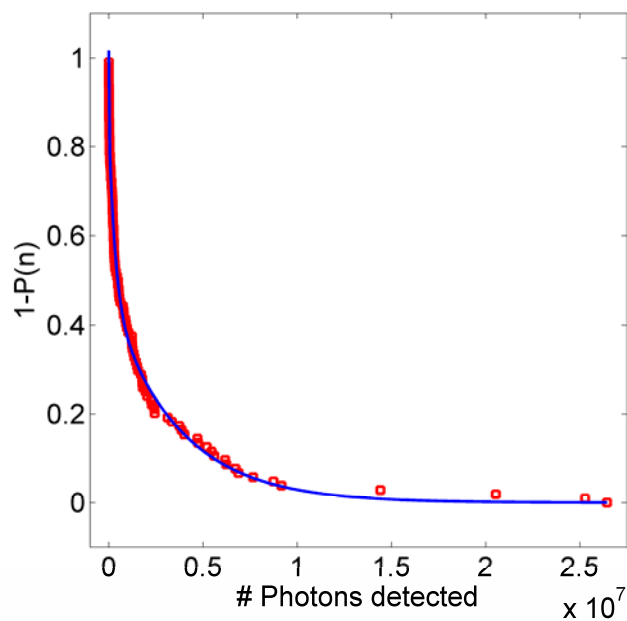


Figure 3.7: Probability distribution of the number of photons detected before photobleaching, obtained from a set of 104 single molecule measurements (red squares), and fitted to a tri-exponential decay function (blue line). Excitation power was $19\mu\text{W}$.

Chapter 4

SINGLE MOLECULE TRACKING BASED ON A NEW IMAGING MODEL

4.1 Introduction

SMT is a powerful method in fluorescence microscopy. It involves recording of a movie from a sample, where single fluorescent molecules serve as probes of their environment or tracers of other chemically attached molecules. Upon determining locations of the single molecules in each individual frame, and relating these to the position information from other frames, one can obtain the trajectories of single molecules in that sample [58-60].

The main advantage of SMT over other single molecule techniques lies in the combined spatial and temporal information it provides. The temporal part of this information is fairly reliable with contemporary electronics. The spatial part on the other hand requires careful analyses, due to limited optical resolution and signal levels. This has been addressed either in the more general framework of particle tracking [100-102], or by specifically considering single molecules with an emphasis on accuracy [103], or both accuracy and speed [104]. Among algorithms suitable for SMT, direct Gaussian fitting [100] with a maximum likelihood estimator (MLE) [105,106] was found to be the most accurate one.

The estimation performance can be enhanced by a better representation of the data generation process. A good example of this has been demonstrated in [103,104], where the discrete and independent nature of the photon emission event was put into use to develop a novel imaging model based on Poisson statistics. Their analysis however considered stationary molecules only.

The present chapter extends the same approach to a moving molecule, by taking into account its motion during the exposure time of a frame. Since this extended model better represents the real imaging process, it is expected to yield more accurate position estimates for a moving molecule. As inherently including motion, the new imaging model also allows molecules' velocity to be estimated from single frame data. The single-frame position and velocity estimates are then fed into a Kalman filter to have an algorithmic framework for tracking [107-109].

The chapter is organized as follows: Section 2 describes the assumed imaging model, Section 3 explains the algorithm, Section 4 puts the algorithm into test by means of simulations and real experimental data obtained with a piezo scanner, and Section 5 finally gives a concluding summary.

4.2 Imaging Model

The imaging model to be developed in this section extends the model of [103] to moving molecules. As illustrated in Figure 4.1, motion of a molecule within 1 frame exposure time, T , is assumed to be a uniform translational motion from an initial position (x_0, y_0) at the beginning of the exposure to a final position at the end of the exposure. The position at an arbitrary time t is denoted by (x, y) , and the (constant) velocity components of the uniform motion are denoted by (v_x, v_y) . The whole motion of a molecule throughout the movie, the molecule trajectory, is thus assumed to be a piecewise linear function of (x, y) versus t . For reasons to be explained in the next section, the mid-frame position components are defined as $x_c = x_0 + v_x \cdot T/2$, and $y_c = y_0 + v_y \cdot T/2$. All of these position and velocity components are defined in the sample plane. Their corresponding values in the image plane are obtained by multiplying by the magnification, M .

The image of the sample develops progressively as the emitted photons land on the camera chip. The photons are assumed to be originating either from the imaged molecule, or the background. Both sources are assumed to emit in the form of homogeneous Poisson processes denoted by $q_0(t)$ and $q_{bg}(t)$ with respective (constant)

rates of λ_0 , and λ_{bg} . Landing of emitted photons on the camera chip is described by the point spread function $g(x,y)$, which is approximated by a 2-D Gaussian function as is well-established in tracking of sub-wavelength particles.

Parameters of the described model and their units are tabulated in Table 4.1. Two alternative unit systems are used corresponding to the sample and image spaces. When expressed in sample units, the parameter values remain unchanged under different exposure times. The model parameters are estimated from single frame data as described in the next section.

Parameter	Units	
	Sample space	Image space
x_0, y_0	nm	pixel
v_x, v_y	$\mu\text{m/s}$	pixel/frame
λ_0	photons/s/molecule	counts/frame/molecule
λ_{bg}	photons/s/pixel	counts/frame/pixel

Table 4.1: Parameters of the described imaging model and their units in the sample and image spaces.

4.3 Algorithm

The SMT algorithm described here can be considered as a low- and high level analysis of a recorded movie. The low level analysis works on an individual frame, and determines the position of the tracked molecule in that frame. The high level analysis fuses the position information from individual frames to improve the localization precision and accuracy, and to obtain the resulting trajectory.

The low level analysis is treated as an estimation problem, where the unknown parameters of the imaging model (listed in Table 4.1) are estimated from the image of the tracked molecule, using the maximum likelihood approach. Since there are typically many molecules in a frame, a region of interest, to be called window, has to be defined around the tracked molecule. The estimation algorithm accepts the window as an input, and returns the estimates of the model parameters as an output.

Defining the window for the estimation algorithm is handled by the high level analysis. For the first frame, the window is readily defined when the user specifies the molecule to be tracked. For subsequent frames, the window position (size is kept fixed) must be renewed so as to enclose the moving molecule. This requires that the high level analysis must have a predicted estimate of the molecule position, before the low level analysis can actually estimate it. This results in a recursive estimation-prediction cycle, for a prediction must also depend on previous estimates. The Kalman filtering technique of statistical estimation theory is a perfect match for such recursive data processing problems, and forms the basis of the high level analysis. Besides being a prediction tool for placing the window in the next frame, Kalman filtering also compensates the error in position and velocity estimates of the current frame by conditioning them on those of the past frames.

The following subsections will provide the details of the low level (in-frame estimation) and high level (Kalman filtering) analyses.

4.3.1 Maximum Likelihood Approach for In-frame Parameter Estimation

The maximum likelihood estimation is one of the most popular approaches in estimation [107]. Its application requires that the joint probability mass function (pmf) of the measured pixel values m_1, \dots, m_N should be derived as a function of the unknown parameters $x_0, y_0, v_x, v_y, \lambda_0, \lambda_{bg}$ of the model described in the previous section.

The stochastic nature of photon detection event brings an unavoidable uncertainty to the mapping between the image and sample planes, and requires a probabilistic interpretation. The probability p_k , that a photon emitted at (x', y') in the sample plane lands on a pixel k of the chip is defined as:

$$p_k(x', y') = \int_{A_k} g(x - x', y - y') dx dy, \quad (4.1)$$

where $g(x, y)$ is the point spread function, A_k is the projection of the pixel area on the sample plane defined as: $A_k = \{(x, y): x_{k1} \leq x \leq x_{k2}, y_{k1} \leq y \leq y_{k2}\}$, and the detection efficiency is assumed to be 1.

For a moving molecule, the photon emission positions (x', y') and hence the p_k values change with time. The assumed linear motion of the imaging model can be included into p_k by substituting $x' = x_0 + v_x \cdot t$, and $y' = y_0 + v_y \cdot t$ in eq. (4.1). This yields a time-varying p_k written in terms of the model parameters:

$$p_k(t) = \int_{A_k} g(x - x_0 - v_x t, y - y_0 - v_y t) dx dy. \quad (4.2)$$

In order to arrive from $p_k(t)$ to the pmf of the pixel values, the photon arrival process to pixel k , denoted by $\{q_k(t), t \geq 0\}$. Having contributions from two Poisson processes (emissions of the molecule and the background), $\{q_k(t)\}$ is also a Poisson process. Its rate can be written as:

$$\lambda_k(t) = \lambda_0 p_k(t) + \lambda_{bg}, \quad (4.3)$$

where the first term on the right hand side is the contribution from the molecule, given by the product of the photon generation rate and the landing probability. The second term is the contribution from the constant and homogenous background, for which the arrival probability is the same for all times and pixels, and therefore dropped. eq. (4.3) signifies that $\{q_k(t)\}$ has a time-varying rate, and is therefore a non-homogeneous Poisson process. The non-homogeneity comes from the motion of the molecule.

The pmf of $\{q_k(t)\}$, denoted by $p_{q_k(t)}(m)$, gives the probability of having m photons arrived to pixel k until time t , and can be written as:

$$p_{q_k(t)}(m) = \frac{\Lambda_k(t)^m}{m!} e^{-\Lambda_k(t)}, \quad (4.4)$$

where $\Lambda_k(t) = \int_0^t \lambda_k(\tau) d\tau = \lambda_0 \int_0^t p_k(\tau) d\tau + \lambda_{bg} t$. It is worth emphasizing that the probability functions $p_k(t)$ and therefore the pmf functions $p_{q_k(t)}(m)$ are functions of the unknown model parameters, $x_0, y_0, v_x, v_y, \lambda_0, \lambda_{bg}$.

Assuming that each pixel detects photons independently from other pixels, the joint pmf of the pixel photon counts at the end of the exposure time T can be written as the product of the marginals:

$$P_{q_1(T), q_2(T), \dots, q_N(T)}(\mathbf{m}_1, \dots, \mathbf{m}_N; \Theta) = \frac{\Lambda_1(T)^{m_1} \Lambda_2(T)^{m_2} \dots \Lambda_N(T)^{m_N}}{m_1! m_2! \dots m_N!} e^{-\sum_{k=1}^N \Lambda_k(T)}, \quad (4.5)$$

where Θ is the parameter vector defined as $\Theta = [x_0 \ y_0 \ v_x \ v_y \ \lambda_0 \ \lambda_{bg}]^T$, with subscript T denoting the transpose.

Eq. (4.5) is the pmf needed for the maximum likelihood algorithm. It gives the probability of obtaining a particular image $\mathbf{m} = [m_1 \ m_2 \ \dots \ m_N]^T$, for fixed T and Θ . As usual, it can also be read as the likelihood function by considering \mathbf{m} as the independent variable, and Θ as the dependent variable (for fixed T).

The log-likelihood function, L , is then just the natural logarithm of eq. (4.5), given by:

$$L(\Theta) = \sum_{k=1}^N m_k \log(\Lambda_k(\Theta)) - \sum_{k=1}^N \log(m_k!) - \sum_{k=1}^N \Lambda_k(\Theta). \quad (4.6)$$

The goal of the in-frame estimation algorithm is to find the Θ that maximizes the $L(\Theta)$ in eq. (4.6). This is done by Newton-Raphson method, for which the updates can be written as:

$$\hat{\Theta}^{(t+1)} = \hat{\Theta}^{(t)} - \mathbf{g}^{(t)}, \quad t = 1, \dots, \Omega \quad (4.7)$$

where $\hat{\Theta}^{(t)}$ is the estimate of the model parameter vector at iteration t , $\mathbf{g}^{(t)}$ is the update vector at iteration t , whose k^{th} entry can be written as

$$\mathbf{g}_k = \left(\frac{\partial^2 L(\Theta)}{\partial \Theta_k^2} \right)^{-1} \left(\frac{\partial L(\Theta)}{\partial \Theta_k} \right), \quad (4.8)$$

and Ω is the number of iterations. The general expressions for the first- and second-order partial derivatives of $L(\Theta)$ with respect to the components of Θ can be written as:

$$\begin{aligned} \frac{\partial L(\Theta)}{\partial \Theta_i} &= \sum_{k=1}^N \frac{m_k}{\Lambda_k(\Theta)} \frac{\partial \Lambda_k(\Theta)}{\partial \Theta_i} - \sum_{k=1}^N \frac{\partial \Lambda_k(\Theta)}{\partial \Theta_i} \\ &= \sum_{k=1}^N \left(\frac{m_k}{\Lambda_k(\Theta)} - 1 \right) \frac{\partial \Lambda_k(\Theta)}{\partial \Theta_i}, \end{aligned} \quad (4.9)$$

and

$$\begin{aligned}
\frac{\partial^2 L(\Theta)}{\partial \Theta_i \partial \Theta_j} &= \sum_{k=1}^N -\frac{m_k}{\Lambda_k^2(\Theta)} \frac{\partial \Lambda_k(\Theta)}{\partial \Theta_i} \frac{\partial \Lambda_k(\Theta)}{\partial \Theta_j} + \sum_{k=1}^N \frac{m_k}{\Lambda_k(\Theta)} \frac{\partial^2 \Lambda_k(\Theta)}{\partial \Theta_i \partial \Theta_j} - \sum_{k=1}^N \frac{\partial^2 \Lambda_k(\Theta)}{\partial \Theta_i \partial \Theta_j} \\
&= \sum_{k=1}^N \left[-\frac{m_k}{\Lambda_k^2(\Theta)} \frac{\partial \Lambda_k(\Theta)}{\partial \Theta_i} \frac{\partial \Lambda_k(\Theta)}{\partial \Theta_j} + \left(\frac{m_k}{\Lambda_k(\Theta)} - 1 \right) \frac{\partial^2 \Lambda_k(\Theta)}{\partial \Theta_i \partial \Theta_j} \right]. \quad (4.10)
\end{aligned}$$

The specific forms of eqs. (4.9) and (4.10) for components of Θ can be found in Appendix B. As shown there, when the point spread function $g(x,y)$ is taken to be a 2-D Gaussian function, the $p_k(t)$ functions appearing implicitly in $\Lambda_k(\Theta)$ in the above derivatives can be written in terms of error functions, which greatly facilitates vectorizing the code [104].

Having written the log-likelihood function (eq. (4.6)) and the general expressions for its partial derivatives (eq. 4.9 and 4.10), it would be very intuitive at this point to discuss the Fisher Information Matrix (FIM) of the proposed imaging model. FIM is an analytical tool, widely used in parameter estimation problems. It has the utility that its inverse defines a lower bound (known as the Cramer Rao lower bound; CRLB) for the error covariance of all possible unbiased estimators. The square root of the CRLB will therefore provide the best achievable precision, with which one can estimate the model parameters from the image of a molecule in an unbiased way.

The FIM, J , for the parameter vector Θ is defined as

$$[J(\Theta)]_{ij} = -E \left[\frac{\partial^2 L(\Theta)}{\partial \Theta_i \partial \Theta_j} \right], \quad (4.11)$$

where $E[\dots]$ denotes expectation, and L is the log-likelihood function. Substituting eq. (4.6) into eq. (4.11), using the independence of the pixel values, and recognizing that $E[m_k] = \Lambda_k(\Theta)$, one obtains the ij entry of $J(\Theta)$ as

$$[J(\Theta)]_{ij} = \sum_{k=1}^N \frac{1}{\Lambda_k(\Theta)} \frac{\partial \Lambda_k(\Theta)}{\partial \Theta_i} \frac{\partial \Lambda_k(\Theta)}{\partial \Theta_j}, \quad (4.12)$$

and can write $J(\Theta)$ in a more suitable form as

$$J(\Theta) = \sum_{k=1}^N \frac{1}{\Lambda_k(\Theta)} \frac{\partial \Lambda_k(\Theta)}{\partial \Theta} \frac{\partial \Lambda_k(\Theta)^T}{\partial \Theta}. \quad (4.13)$$

The derivatives in the FIM are evaluated at the true values of the parameter vector, meaning that the CRLB resolution limits are going to be different for different parameter values (for example different molecule velocities). For the special case of a stationary molecule (i.e. $v_x = v_y = 0$), the derivatives in the FIM become

$$\begin{aligned}\frac{\partial \Lambda_k(\Theta)}{\partial x_0} &= \lambda_0 \frac{\partial p_k}{\partial x_0} T, \\ \frac{\partial \Lambda_k(\Theta)}{\partial y_0} &= \lambda_0 \frac{\partial p_k}{\partial y_0} T, \\ \frac{\partial \Lambda_k(\Theta)}{\partial v_x} &= \lambda_0 \frac{\partial p_k}{\partial x_0} \frac{T^2}{2}, \\ \frac{\partial \Lambda_k(\Theta)}{\partial v_y} &= \lambda_0 \frac{\partial p_k}{\partial y_0} \frac{T^2}{2}, \\ \frac{\partial \Lambda_k(\Theta)}{\partial \lambda_0} &= p_k T,\end{aligned}$$

and

$$\frac{\partial \Lambda_k(\Theta)}{\partial \lambda_{bg}} = T.$$

Based on these derivatives, one sees that

$$\frac{\partial \Lambda_k(\Theta)^T}{\partial \Theta} \begin{bmatrix} T/2 \\ 0 \\ -1 \\ 0 \\ 0 \\ 0 \end{bmatrix} = 0 \quad \text{and} \quad \frac{\partial \Lambda_k(\Theta)^T}{\partial \Theta} \begin{bmatrix} 0 \\ T/2 \\ 0 \\ -1 \\ 0 \\ 0 \end{bmatrix} = 0 \quad \text{for all } k. \quad (4.14)$$

Consequently, the FIM given by eq. (4.13) is rank deficient (with rank 4) for the case of a stationary molecule. The rank deficiency implies inherent ambiguity in resolving parameters corresponding to directions within the null-space of the FIM.

On the other hand, the FIM is non-singular in the directions orthogonal to the span of the null space vectors given in eq. (4.14). For example, the FIM is non-singular in the directions

$$\begin{bmatrix} 1 \\ 0 \\ T/2 \\ 0 \\ 0 \\ 0 \end{bmatrix} \quad \text{and} \quad \begin{bmatrix} 0 \\ 1 \\ 0 \\ T/2 \\ 0 \\ 0 \end{bmatrix}, \quad (4.15)$$

corresponding to mid-frame x- and y-positions (i.e. $x_c = x_0 + v_x \cdot T/2$, and $y_c = y_0 + v_y \cdot T/2$), which means that there is no ambiguity in estimating these parameters.

The problem of singularity of the FIM for the stationary molecule case transforms to the problem of ill-conditionedness for relatively slow (near stationary) motions. This manifests itself as high estimation errors in the linear combination of model parameters nearly in the directions defined by the span of the vectors in eq. (4.14). On the other hand, the mid-frame position vector $[x_0 + v_x \cdot T/2 \quad y_0 + v_y \cdot T/2]^T$ can almost always be estimated accurately, despite the potential inaccuracies in the individual position and velocity parameters. This argument is, of course, only valid when the in-frame motion length is less than the window size, as will be discussed in Section 4.

As a final remark to this subsection, it must be noted it is not possible to determine the actual sign of the velocity vector from single-frame data only (i.e., there is an inherent sign ambiguity). The algorithm yields the estimates of the initial position and the velocity vector, from which one can calculate the estimate of the final position. An alternative result with these initial and final position estimates interchanged and the sign of the velocity components reversed, fits the data equally well. Deciding on the correct alternative requires additional information from neighboring frames. This is done during the high-level analysis.

4.3.2 Kalman Filtering for Tracking

Kalman filter is a recursive data processing algorithm used in estimating the state of a linear dynamic system from noisy measurements. In the present case, the system corresponds to the moving molecule, measurements correspond to the in-frame estimations, and state is a set of parameters that describe molecule's motion. The Kalman filtering equations will be described following the same notation as of [108]: Lower-case characters are used to show vectors, and written in bold font for random variables. Matrices are denoted by upper-case italic characters. The subscript k indicates the discrete time steps, corresponding to frame numbers.

The state-space model is given by:

$$\begin{aligned}\mathbf{x}_k &= F_{k-1} \mathbf{x}_{k-1} + \mathbf{n}_{k-1} \\ \mathbf{y}_k &= H \mathbf{x}_k + \mathbf{v}_k,\end{aligned}\quad (4.16)$$

where \mathbf{x} is the state vector, F is the transition matrix, \mathbf{n} is the process noise, \mathbf{y} is the measurement vector, H is the observation matrix, and \mathbf{v} is the measurement error.

The state vector is defined to be

$$\mathbf{x} = \begin{bmatrix} x_c \\ y_c \\ v_x \\ v_y \end{bmatrix}.\quad (4.17)$$

The transition matrix, under the constant uniform motion assumption of the imaging model, is given by

$$F = \begin{bmatrix} 1 & 0 & T + T_r & 0 \\ 0 & 1 & 0 & T + T_r \\ 0 & 0 & 1 & 0 \\ 0 & 0 & 0 & 1 \end{bmatrix},\quad (4.18)$$

where T_r is the read-out time. H is the identity matrix (the system is fully observable).

The process noise \mathbf{n} , and the measurement error \mathbf{v} are assumed to be normally distributed around 0 mean with covariance matrices Q and R respectively. Q and R are diagonal matrices, with their elements given by the typical variations in the actual and

measured values respectively of the parameters in \mathbf{x} . These variations are assumed to remain constant throughout the motion.

Due to the recursive nature of Kalman filtering, the operations carried at a frame k involve predictions from (to) the previous (next) frame, denoted by subscript $k|k-1$ ($k+1|k$), and related to their current estimates, denoted by subscript $k|k$, through measurement (time) update equations. The operations start with the measurement to obtain \mathbf{y}_k . Then the measurement innovation vector, \mathbf{e}_k , and its covariance matrix, $R_{\mathbf{e},k}$, and subsequently the Kalman gain matrix, $K_{f,k}$, are calculated according to

$$\mathbf{e}_k = \mathbf{y}_k - H\hat{\mathbf{x}}_{k|k-1}, \quad (4.19)$$

$$R_{\mathbf{e},k} = HP_{k|k-1}H^T + R, \quad (4.20)$$

$$K_{f,k} = P_{k|k-1}H^TR_{\mathbf{e},k}^{-1}, \quad (4.21)$$

Next, the state vector estimate $\hat{\mathbf{x}}$ and the error covariance matrix P are updated by the measurement-update equations:

$$\hat{\mathbf{x}}_{k|k} = \hat{\mathbf{x}}_{k|k-1} + K_{f,k}\mathbf{e}_k, \quad (4.22)$$

$$P_{k|k} = P_{k|k-1} - K_{f,k}R_{\mathbf{e},k}K_{f,k}^T. \quad (4.23)$$

And finally the time-update equations predict their values for the next frame:

$$\hat{\mathbf{x}}_{k+1|k} = F_k\hat{\mathbf{x}}_{k|k}, \quad (4.24)$$

$$P_{k+1|k} = F_kP_{k|k}F_k^T + Q. \quad (4.25)$$

Since $\hat{\mathbf{x}}_{k|k-1}$ and $P_{k|k-1}$ will not be present for $k = 1$, they must be initialized with typical values before the algorithm starts.

As mentioned earlier in the in-frame estimation subsection, single frame data alone is not sufficient to determine the correct sign of the velocity vector. Therefore while updating the Kalman filter, one has to check for the sign of the velocity vector. This is done by calculating Kalman updates of both alternatives, and comparing the Frobenius norms of the resulting windows in the next frame. If the norms are different by more than 1.5 times (a user-defined arbitrary factor), the program concludes that the one with lower norm misses the molecule, and therefore is the wrong choice. If the difference

does not reach this threshold (i.e. the molecule still remains within the window even with wrong choice of sign, as can happen for slow motions, or large windows), then the in-frame estimation is run in the next frame for both window positions, and the alternative that yields better agreement between the time updated position and the estimation result is chosen.

4.4 Testing the Algorithm

This section evaluates the performance of the algorithm at both the low- and the high-levels. In testing the low level analysis (in-frame estimation), the estimation part of the algorithm is applied to simulated images of a moving molecule, and its success is compared with the theoretical outcomes of the CRLB calculations. For testing the high-level analysis (tracking), the whole algorithm is used to analyze actual single molecule movies, where motion has been generated by a piezo stage. Molecule trajectories obtained from analysis are compared with the position information from the piezo stage sensor.

4.4.1 Generating Simulated Images

Simulated image of a moving molecule was generated by accumulating individual photons emitted by that molecule in camera pixels. Each photon had three accompanying data: i) random emission time, ii) emission position in the sample space, and iii) landing position in the image space. Random numbers corresponding to times elapsed between subsequent emitted photons were drawn from an exponential distribution with parameter $1/\lambda_0$. The unique emission times of the photons were then given by the cumulative sum of the times between subsequent photons. This was continued until the emission times reached T . The emission positions of the photons were given by the position of the molecule at the time of emission. This depends on the (known) trajectory of the molecule. For each photon, its landing position on the camera chip was determined by randomly drawing a single value from a normal distribution

with mean equal to the emission position, and width to the theoretical point spread function. The landing positions were then assigned to pixels to yield the final image.

4.4.2 Piezo Stage Experiments

A thin film of PMMA (Aldrich 201033) doped with well-separated terrylene dye molecules was spin-coated onto glass coverslips. Prior to spin coating, the coverslips were cleaned with a UV-O cleaner (Jelight Company, Model: 42) for 10 minutes. This sample was then mounted onto a piezo scanner (Physical Instruments, stage: P-733.3DD, controller: E-509.C3A) and moved with a known trajectory generated by a multi-purpose data acquisition (DAQ) card (National Instruments PCIe-6363). The same card was also used to read the position feedback of the stage (at 10kHz). Wide-field imaging was done in the standard way, with an NA=1.49 oil objective (Nikon, TIRF Apochromat), 178x total magnification, and an EM-CCD camera with pixel size of 16 μ m (Hamamatsu C9100-13). The point spread function of the setup was determined from stationary single molecule images, and corresponded to $\sigma = 1.2\text{pixel} = 108\text{nm}$, when approximated with a Gaussian function. This σ value has been used in analyzing recorded movies. The camera was operated at its 11MHz/pixel clock rate mode, with an EM-gain of 255, and was externally triggered by the DAQ card, so that driving the piezo, reading its sensors, and image acquisition were all done in synchronization. Excitation was done with a green diode laser of $\approx 10\text{mW}$ power and a suitable dichroic mirror (Chroma z532/1064rpc). Fluorescence was further separated from excitation using notch (Chroma ZET532NF) and band-pass (Chroma HQ605/90M) filters (same as shown in Figure 2.2).

Since the formulation in the in-frame estimation algorithm is based on photon numbers, applying it to frames of a movie required a conversion from pixel counts to photon numbers. This has been done according to the relation:

$$N_{\text{photons}} = \frac{\left(N_{\text{counts}}^{\text{image}} - N_{\text{counts}}^{\text{dark}}\right) \cdot \text{ConversionFactor}}{\text{Ana log Gain} \cdot \text{EMGain} \cdot \text{QE}}, \quad (4.26)$$

where $N_{photons}$ are the number of photons arrived to the pixels, N_{counts}^{image} are the pixel values of the image, N_{counts}^{dark} are the pixel values in the absence of illumination, and other quantities are the fixed or adjustable specification parameters of the camera [109]. The distribution of the pixel values in a dark image was so narrow that N_{counts}^{dark} was taken as a constant equal to the mean dark pixel value.

4.4.3 Results and Discussions

As a first attempt to evaluate the performance of in-frame estimation, a molecule moving with uniform translational motion along the positive x-direction has been considered ($v_x \neq 0$, $v_y = 0$). The molecule speed was taken to be $3.11\mu\text{m/s}$, corresponding to 7pixel/frame for $T = 0.2\text{s}$. A window size of 15×15 pixels was used, and λ_0 and λ_{bg} were taken to be 15000 and 300photons/s respectively, representing the typical values obtained in real experiments.

Figure 4.2.a shows the CRLB limits for parameters x_0 , v_x , and x_c as a function of T , calculated from the FIM. Except for the extreme T values, the CRLB limits increase only slightly with the increasing exposure time. The divergence on the long T end is merely a finite window size effect: As the exposure time is increased, a molecule with a certain speed travels more pixels per frame, and its smeared image eventually extends out of the estimation window. The rise in the CRLB of x_0 and v_x , at short exposure times is a result of the ill-conditionedness problem of the FIM, discussed in Subsection 4.3.1 above. In the short T limit, the image of the molecule becomes less smeared, or equivalently less dependent on v_x . This causes a redundancy in parametrization that appears as a correlation between x_0 and v_x , and renders their individual estimations subject to high uncertainties. On the other hand, x_c intrinsically achieves better precision as discussed in the FIM analysis.

Figures 4.2.b and 4.2.c show the same type of analysis using simulated data. All parameters had the same values as for Figure 4.2.a, and a set of 50 images was analyzed for each T . The window center was placed at (x_c, y_c) position, and the maximum

likelihood algorithm was run for 400 iterations¹. Due to the uncertainty in determining direction of motion mentioned before, the v_x estimates sometimes had the reverse sign with respect to the true molecule velocity used in the simulation. For such cases the sign of the velocity vector estimate was changed, and the initial position estimate was replaced with the final one. In order to compare the performance the proposed estimation algorithm to standard tracking programs that do not take in-frame motion of the molecule into account, the same set of simulated images were also processed with a modified version of the proposed algorithm that assumed a stationary molecule and, thus, could only provide estimates of the mean in-frame position of the molecule, x_m .

In Figure 4.2.b, the mean of the estimates is compared with the actual values used in the simulation, and their difference, the bias, is interpreted as the accuracy of the estimator for that parameter (to be denoted with a hat). The accuracy of \hat{x}_c is quite good, with <0.05 pixel (<4.4 nm) bias for all $T < 0.5$ s, whereas both \hat{x}_0 and \hat{v}_x are biased. If the stationary molecule algorithm is applied, \hat{x}_m becomes biased at moderate values of $T > 0.25$ s, where smearing of the molecule image due to its motion becomes significant.

Similarly, Figure 4.2.c shows the standard deviations of x_0 , v_x , and x_c estimates, interpreted as the precisions of \hat{x}_0 , \hat{v}_x , and \hat{x}_c respectively. A comparison with the CRLB limits of Figure 4.2.a reveals that the two are very close for T values from 0.1s to 0.4s. The window effect on the long T side is almost identical, whereas the diverging behavior of the uncertainty in x_0 and v_x estimates on the short T side disappears to a large extent in Figure 4.2.c. This is attributed to \hat{x}_0 and \hat{v}_x being biased estimators (see Figure 4.2.b), as opposed to the unbiased estimator assumption of the CRLB analysis. \hat{x}_c performs the best also in terms of precision, with <0.08 pixel (<7.1 nm) standard

¹ The number of iterations was kept highly conservative, to ensure that the resulting statistics reflects the performance of the estimation algorithm, and not the variations among not-fully-converged parameters. Otherwise, <100 iterations were proven to be sufficient for most practical cases.

deviation for all $T \leq 0.4$ s. Again, precision of \hat{x}_m decreases significantly for $T > 0.25$ s, where it becomes worse than both \hat{x}_c and \hat{x}_0 .

All these observations are in agreement with the relatively abstract interpretations of the FIM. Analysis of both CRLB predictions and numerical simulation results conclude that it is more advantageous to describe molecule's motion with the mid-frame position (x_c, y_c) instead of the initial position (x_0, y_0) , and rely more on the position estimates, than on the velocity estimates. In fact, the whole parametrization in this study could have been done using (x_c, y_c) , but there was no way to know in advance that its estimator would perform better. Therefore the material is presented in its natural development. The comparison of x_c with x_m clearly shows that the implicit assumption of molecule motion during image acquisition improves the accuracy and precision of position estimates. As expected, this tendency becomes more pronounced for higher T , where the image distortion due to molecule motion increases.

As a next conclusion from Figure 4.2, one sees that both accuracy and precision of the estimates only slightly depend on T . This suggests that in a real experiment, the choice of a suitable T must be based on other criteria rather than the performance of the estimation algorithm. Working with a short exposure time would be beneficial for several reasons: First and most importantly, this would reinforce validity of the uniform in-frame motion assumption of the proposed imaging model. Secondly, the Kalman filter would be updated more frequently, and third the resulting trajectory would have a higher time resolution. It is true that the in-frame velocity estimation becomes worse for short T , but the main goal here is to determine the position of the molecule as a function of time. The in-frame velocity is just a model parameter estimated at no extra cost. Although it is later on exploited by the Kalman filter (to have better position estimates, and predict where to place the MLE window in the next frame), the main intention for including it into the model was to achieve a better representation of the data generation process. If the molecule velocity on the time scale of T is needed, it can always be

determined (even more precisely) from the difference of mid-frame positions of consecutive frames.

Based on these conclusions, a similar analysis has been carried for a range of velocities and fixed T . This represents the condition in a real experiment. Figure 4.3.a shows the CRLB limits for x_c and v_x estimations as a function of v_x values from 0.5 to 15pixel/frame for $T = 50\text{ms}$ ($v_x = 0.89$ to $26.67\mu\text{m/s}$), and a window of 15×15 pixels. λ_0 and λ_{bg} are again taken to be 15000 and 300photons/s. The maximum error within the studied velocity range turns out to be $<0.5\text{pixel}$ ($<44.4\text{nm}$) for \hat{x}_c , and $<1.5\text{pixel/frame}$ ($<2.67\mu\text{m/s}$) for \hat{v}_x . Similar to Figure 4.2, Figure 4.3.b and 4.3.c present the accuracy and precision with simulated data. The estimation algorithm performs fairly well for both x_c and v_x , except for an increase in the bias in \hat{v}_x for $v_x \leq 3\text{pixel/frame}$, and the finite window effect in Figure 4.3.c. For \hat{x}_c , the bias is $<0.1\text{pixel}$ (8.9nm) for all v_x , whereas the precision is better than 0.2pixel (17.8nm) up to $v_x = 12\text{pixel/frame}$. The negligible bias, and the standard deviation comparable to the CRLB limit indicate that, for $T = 50\text{ms}$, and typical λ_0 and λ_{bg} values, the mid-frame position (x_c, y_c) can be estimated as accurately and precisely as its theoretical limit for a wide range of molecule velocities. Similar to Figure 4.2, accuracy and precision of \hat{x}_m drop significantly with increasing v_x , underlining once again the benefits of the newly proposed tracking algorithm over the traditional stationary-molecule schemes.

The discussions so far were for the in-frame (low level) analysis of the tracking algorithm. Using these results, the remaining part of the section will continue with the piezo-stage experiments, where the high level, Kalman filtering part is also used. In these experiments, the measured (\mathbf{y}_k), and filtered ($\hat{\mathbf{x}}_{k|k}$) position and velocity data of a molecule are compared with their actual values (\mathbf{x}_k) obtained from the position sensor readings. The actual velocity was calculated from position sensor data at a 200 times lower rate (50Hz), to discard the high-frequency noise in the position data. The in-frame estimations were done with 400 iterations for the first frame, and with 100 iterations afterwards, where the starting values in a frame were taken as the results of

the previous one (Kalman time updates for x_c, y_c, v_x, v_y ; and in-frame estimates for λ_0, λ_{bg}). The operation of Kalman filtering is related to the covariance matrices Q and R . Q was formed using approximate values that reflect the expected deviations from the uniform motion assumption. Working with higher process noise variance values tolerates more deviations from the assumed model, but it also results in less accurate estimates. In a real experiment, one can only enter approximate values for the process noise variance, but as shown in [110], the result does not change much; unless an order of magnitude error is made. The elements of R were taken to be the sum of squares of the typical biases and standard deviations in position and velocity estimation suggested by Figure 4.3 ($0.2^2+0^2 = 0.04\text{pixel}^2 = 316\text{nm}^2$ for position, and $0.2^2+0.4^2 = 0.2(\text{pixel}/\text{frame})^2 = 0.63(\mu\text{m}/\text{s})^2$ for velocity).

Figure 4.4.a shows the case for a linear motion along the x-axis. The movie was recorded with $T = 50\text{ms}$, and analyzed using a window of 15×15 pixels. Owing to the perfect agreement between the assumed and actual motions, a small process noise variance was used (1nm^2 for position, and $(1\text{nm}/0.05\text{s})^2$ for velocity). In comparing position data, a constant (but unknown) offset (D_x, D_y) between the position of the analyzed molecule and the origin of the stage position sensor readings had to be eliminated to bring the two to the same origin. This was done by taking the average over k of the differences between the filtered and actual positions (i.e. $D_x = \langle \hat{\mathbf{x}}_{k|k}[1] - \mathbf{x}_k[1] \rangle_k$, and $D_y = \langle \hat{\mathbf{x}}_{k|k}[2] - \mathbf{x}_k[2] \rangle_k$), and subtracting it from the filtered/measured positions. After this necessary shift, the measured and filtered trajectories agree well with the actual one, as seen in Figure 4.4.a.

Figure 4.4.b plots the position error against time (or frame numbers) for the measured and filtered trajectories. The position error is defined as $\sqrt{\Delta x^2 + \Delta y^2}$, where Δ denotes the difference of the measured/filtered values from the actual values at the mid-frame times. One sees that both measured and filtered data reveal the actual motion within average errors of 0.17pixel (15.5nm) and 0.11pixel (9.7nm) respectively. Considering the difficulty in comparing the values from image analysis with the ones

from the real system, this error likely involves other contributions from the shifting procedure, or from slight misalignments or astigmatism within the imaging setup. The level of accuracy obtained here is therefore quite satisfactory for a real experiment. The errors in measured and filtered trajectories do not differ significantly. This is explained by the in-frame position estimations' precision already being comparable to the fluctuations in the sensor reading. Since the sensor reading itself has a standard deviation of 0.03pixel (2.6nm) in the (stationary) y-axis (see Figure 4.4.a), error in the filtered data cannot be smaller than $\sqrt{2} \times 0.03 = 0.04\text{pixel}$ (3.6nm).

The situation with velocity is different. In this case, the in-frame estimates have a larger error than the real velocity fluctuations, and the effect of Kalman filtering becomes clear. This is shown in Figure 4.4.c, where the v_x estimates of the same molecule are plotted together with their filtered and actual counterparts. It is seen that Kalman filtering settles quickly within first three frames, and corrects the noisy estimations. A similar trend would be observed in filtered position estimations too, when working with images of a worse signal-to-noise ratio.

In addition to the linear motion case presented above, Figure 4.5 summarizes the results for a more general type of motion: a sinusoidal trajectory of $y = 2 \sin\left(\frac{2\pi}{2\mu\text{m}}x\right)$ with period 1s. The movie was again recorded with $T = 50\text{ms}$, analyzed using a window of 15×15 pixels, and the offset (D_x, D_y) was corrected. A higher process noise variance (100nm^2 for position, and $4(\mu\text{m/s})^2$ for velocity) was used to compensate the difference between the actual and assumed motions. This resulted in less effective filtering as compared to the linear motion experiment. In fact, the Kalman filtering was almost completely turned off, as evidenced by the coinciding filtered and measured values (see Figure 4.5.a for position, and Figure 4.5.c for velocity). In other words, the whole tracking algorithm worked based on the raw in-frame estimates. Despite the absence of corrections from Kalman filtering, as Figure 4.5.b shows, the error in position estimation still remained smaller than 1pixel (90nm), and had an average value of 0.42pixel (37.4nm). Although this error is higher than the linear motion case, it must be

considered together with the level of velocity and acceleration present in this motion. The maximum values of the (time-varying) velocity and acceleration along y-direction were 7pixel/frame (12.6 $\mu\text{m/s}$), and 2.2pixel/frame² (79 $\mu\text{m/s}^2$), respectively. Two 15 \times 15 pixel images from one of the maximum velocity and maximum acceleration instants are provided in Figure 4.6 to demonstrate the appreciable distortion. This illustrates the potential advantage of the proposed algorithm in analyzing fast molecules. Furthermore the algorithm performs sufficiently well even for accelerated motion that violates the assumptions of the used imaging model.

4.5 Conclusion

An imaging model that takes into account the in-frame motion of the molecules has been proposed. The molecules' motion within the exposure time of a frame was approximated as a constant-speed linear motion. An estimation program based on the maximum likelihood method was developed to estimate model parameters from single molecule images. The Poisson nature of photon emission and detection processes has been benefited in writing the likelihood function. CRLB analyses and simulations have shown that the estimation program can estimate the mid-frame position of a molecule efficiently. The mid-frame position and velocity information obtained from individual frames were then fed into a Kalman filter for inter-frame tracking of molecules. Performance of the tracking algorithm was evaluated via model experiments with a piezo-stage. Tracking of molecules moving as fast as 7pixels/frame (12.6 $\mu\text{m/s}$) has been demonstrated within a mean error of 0.42pixel (37.43 nm).

Incorporating in-frame motion into the imaging model by a constant velocity term can be thought of as a first order correction to traditional tracking algorithms that assume stationary emitters. In this sense, the following higher order corrections would be including first a constant and then a time-varying acceleration term either/both to the imaging model, or/and state vector of the Kalman filter. Although these parameters will bring in new sign ambiguities to the problem, they will hopefully be overcome with the advent of imaging detectors that can deliver arrival times of individual photons.

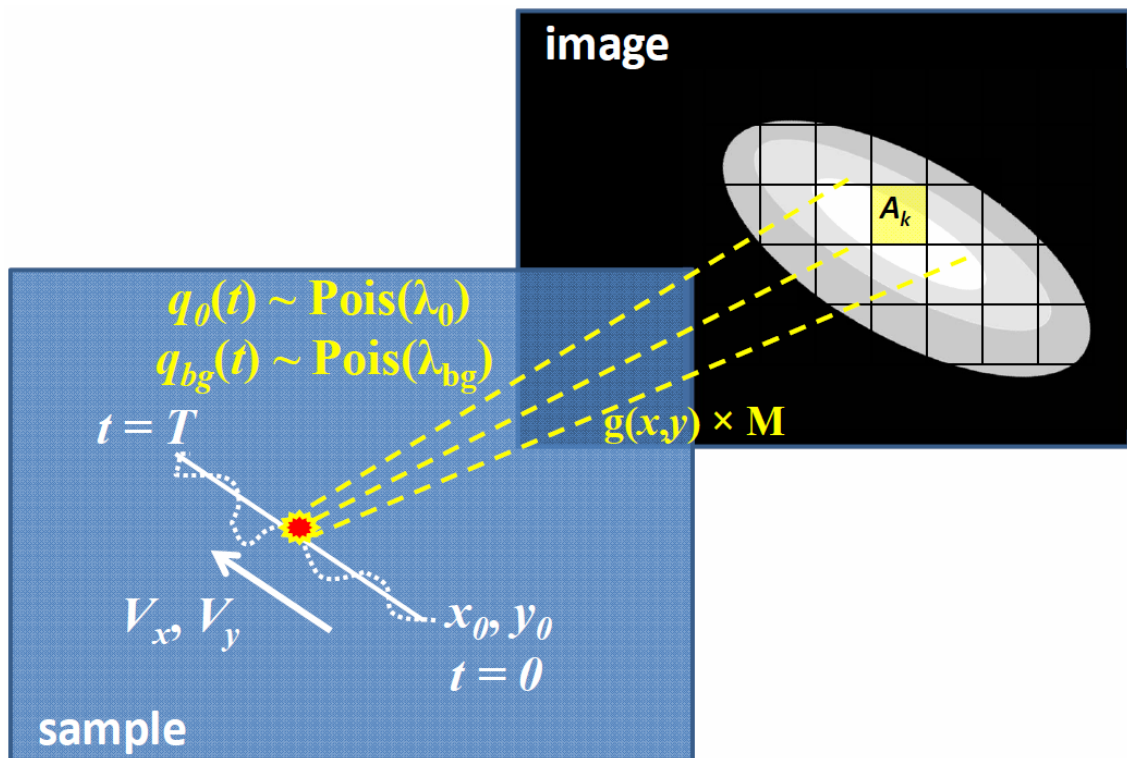


Figure 4.1: Description of the assumed image formation model.

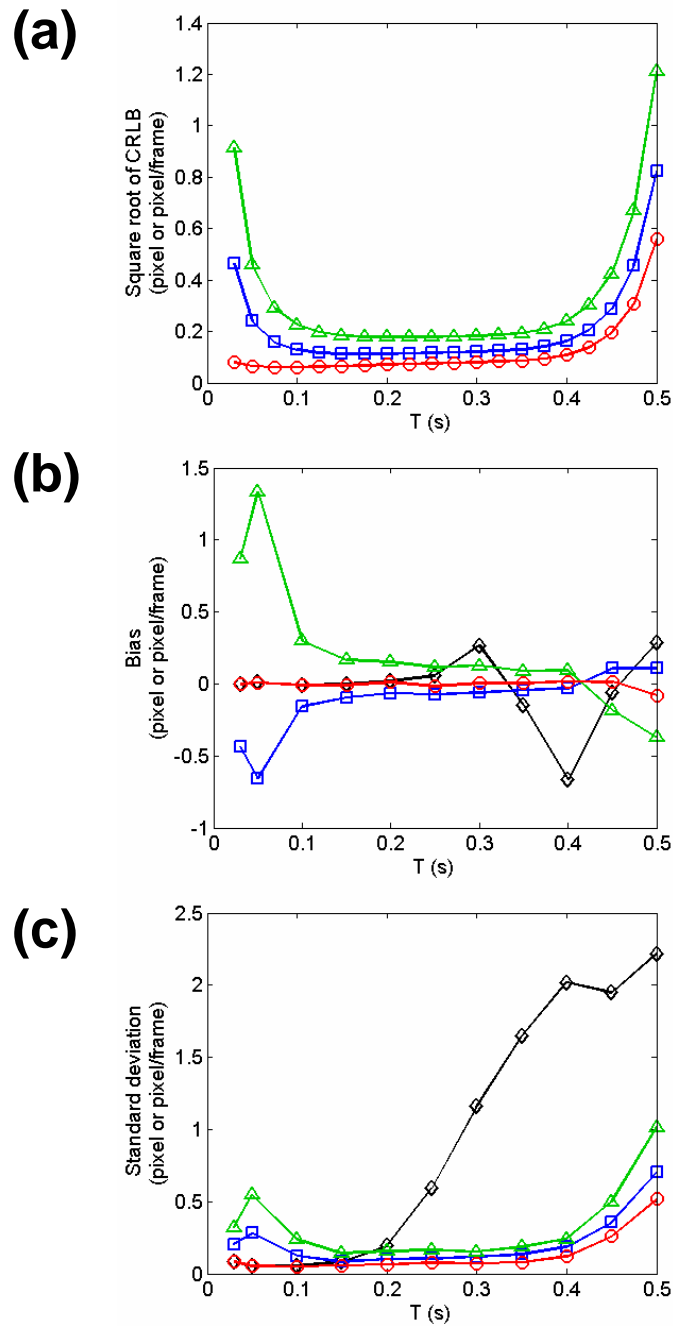


Figure 4.2: Performance of the proposed estimation algorithm as a function of T for parameters v_x (green triangles), x_0 (blue squares), and x_c (red circles). Tracking performance is evaluated on the basis of (a) CRLB limits, (b,c) bias and standard deviation of estimates from simulated images. For comparison, corresponding characteristics of x_m obtained from same set of simulated images are also shown (black diamonds). For all presented data, v_x is kept fixed at $3.11 \mu\text{m/s}$ (7pixel/frame at $T=0.2\text{s}$).

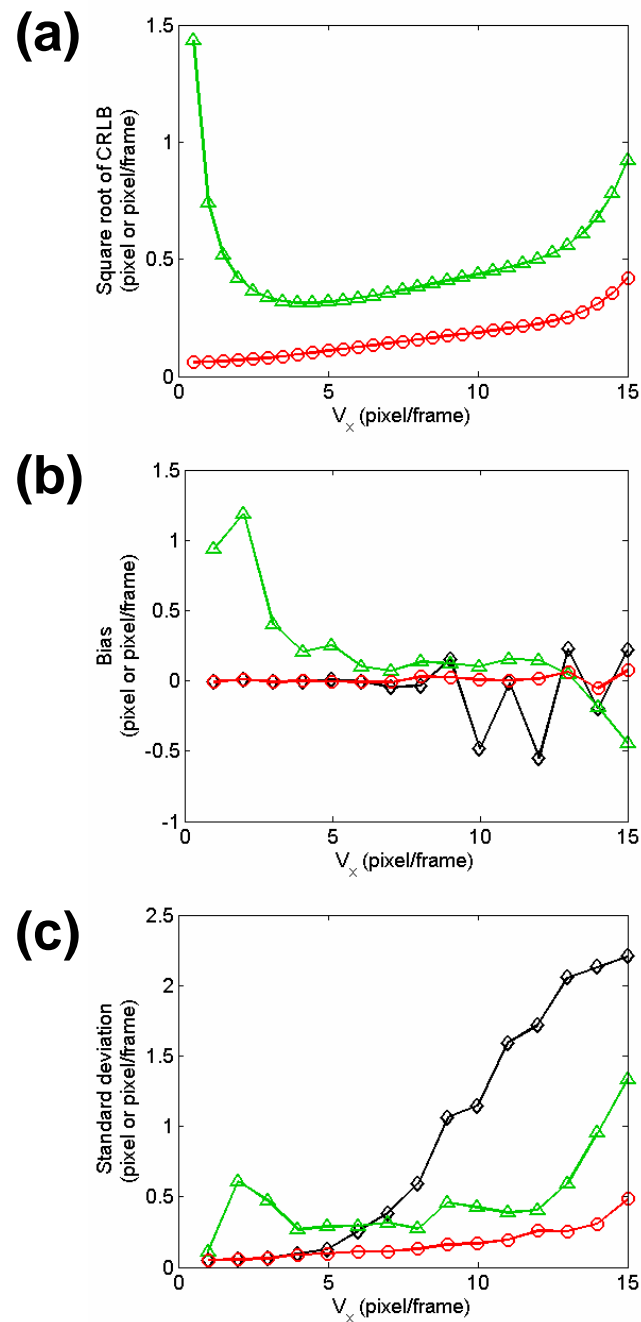


Figure 4.3: Performance of the proposed estimation algorithm as a function of v_x for parameters v_x (green triangles), and x_c (red circles), based on their (a) CRLB limits, (b,c) bias and standard deviation of estimates from simulated images. For comparison, corresponding characteristics of x_m obtained from same set of simulated images are also shown (black diamonds). T is kept fixed at 50ms for all presented data.

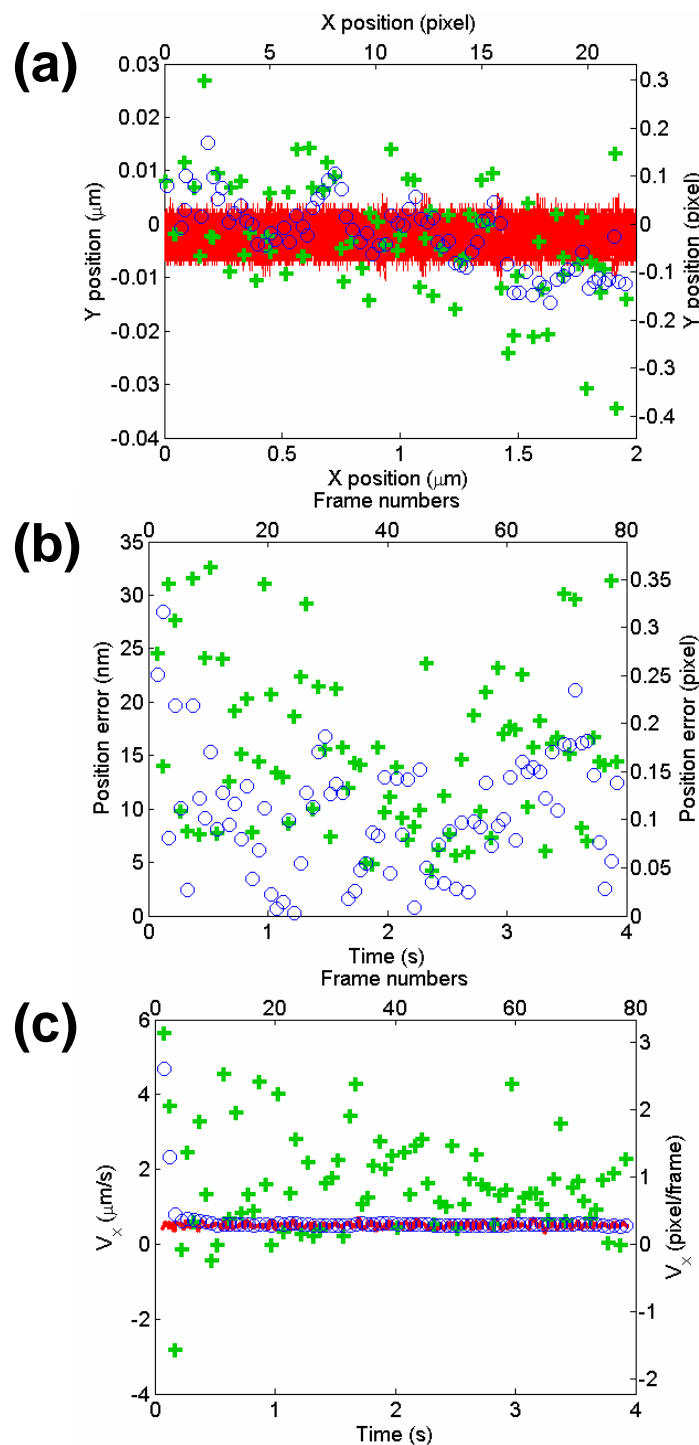


Figure 4.4: A representative result from the piezo-stage experiments, showing (a) the overall linear trajectory, (b) the measurement error, and (c) v_x data for the actual (red line), measured (green pluses), and Kalman-filtered (blue circles) values.

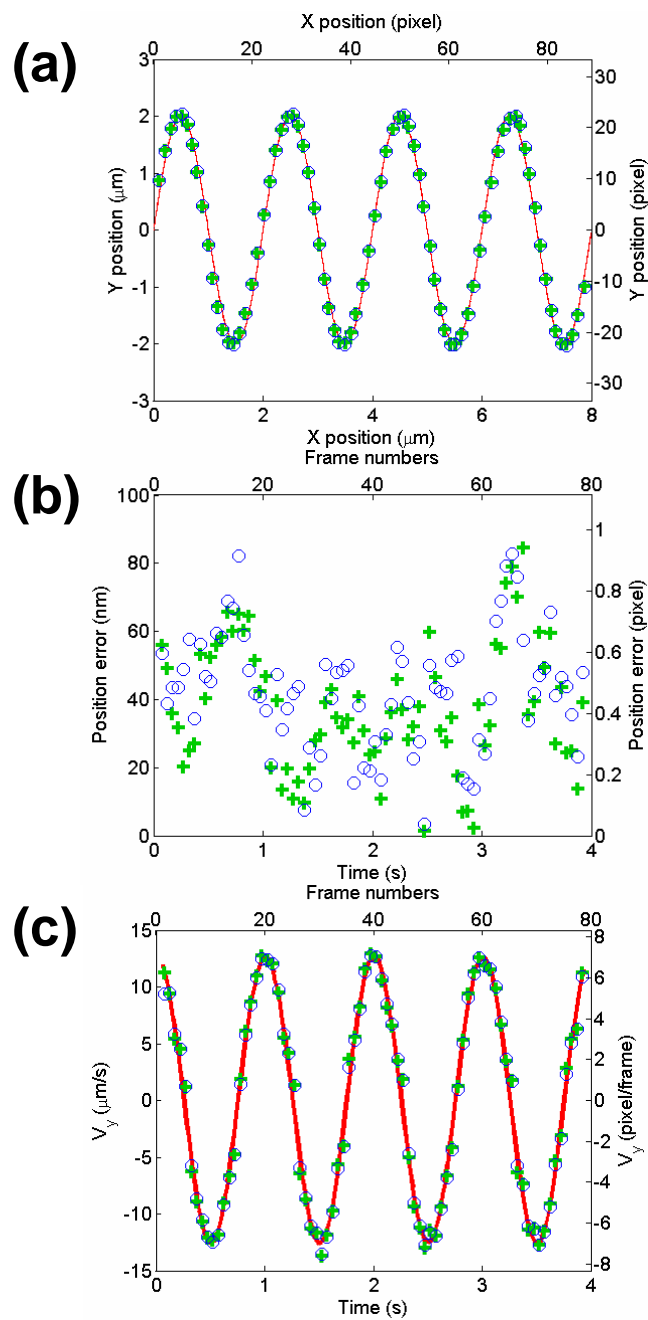


Figure 4.5: Result from the piezo-stage experiments with accelerated motion, showing (a) the overall sinusoidal trajectory, (b) the measurement error, and (c) v_y data for the actual (red line), measured (green pluses), and Kalman-filtered (blue circles) values.

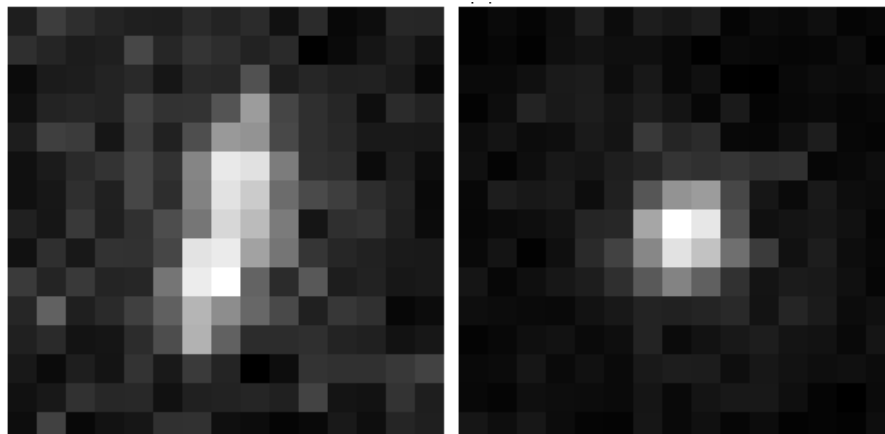


Figure 4.6: Two 15×15 pixel images of the molecule tracked in Figure 4.5, corresponding to representative maximum-velocity (left), and maximum-acceleration (right) instants that occurred at 19th, and 25th frames respectively.

Chapter 5

CHARACTERIZATION OF APD DETECTORS

5.1 Introduction

APDs are the most commonly employed detectors for time-resolved single molecule spectroscopy, and single molecule confocal microscopy. They deliver a standard electronic pulse (TTL pulse) per each detected photon. Strictly speaking, the correct name for these devices would be “single photon avalanche photodiode detector” (SPAPD), however the term APD is used almost interchangeably for SPAPD in single molecule literature [111]. This is valid also for the present thesis. A brief survey from general to specific would be useful to prevent confusion: Photodiode detectors are p-i-n junctions operated under reverse bias [112]. The absorption of an incident photon within the intrinsic region generates an electron-hole pair, after which each charge carrier drifts to corresponding electrode (electrons to the cathode or the n-type region, and holes to the anode or the p-type region) and produce an electrical current in the external circuit. In an avalanche photodiode detector, the reverse bias voltage is held slightly below the breakdown voltage so that the charge carriers can gain sufficient kinetic energy to give rise to further electron-hole pairs in an avalanche fashion. The resulting electrical current due to the avalanche effect goes linearly with light intensity, characterized by a stable gain of $\sim 10^2$ to 10^3 [113]. Owing to this dependence, an avalanche photodiode detector is called to operate in the linear mode. While the avalanche effect significantly increases sensitivity of the photodiode detector, a gain of 10^3 is still not sufficient to detect single photons. To further increase the gain, the bias voltage is brought above the breakdown voltage. In this case however, the avalanche process may cause permanent damage to diode structure. To prevent this, the bias

voltage is reduced soon after the avalanche process starts. This results in delivery of an electrical pulse for each detected photon. Such operation mode is called photon counting mode, or Geiger mode, in analogy to the Geiger Müller tube of particle physics. The bias voltage can be controlled either passively by a resistor or actively by a quenching circuit. The latter produces shorter dead time and thus higher maximum count rate. The APDs used in today's time-resolved single molecule experiments are always actively quenched single photon APDs. Therefore except for the above summary, the acronym APD in this thesis refers to actively quenched single photon avalanche photodiode detectors.

There are two types of noise associated with photon detection. These are the shot noise originating from statistical nature of a discrete event (in this case photon emission/detection) dictated by uncertainty, and Johnson noise originating from thermal fluctuations in the detector. The Johnson noise further separates into two as dark counts and afterpulses. Dark counts arise from electron-hole pairs generated randomly by thermal effects. These can be minimized by cooling the diode or reducing its size. Afterpulses come from charge carriers that are temporarily trapped and released later by thermal fluctuations [114]. The lifetime of these trapped carriers increases with decreasing temperature. Therefore the operating temperature needs to be optimized to achieve a balance between low dark counts (low temperature) and reduced afterpulsing probability (high temperature) to minimize the Johnson noise.

This chapter describes some basic measurements with APDs, performed at then UEKAE (Turkish acronym for "National Research Institute of Electronics and Cryptology"). Section 2 gives the experimental details. Section 3 presents dynamic range measurements, which are also used for determining dark counts and linearity. Section 4 is about stability of APDs. Section 5 studies the effect of diode temperature and bias voltage on the detection rate. Section 6 uses the data of previous sections to show the effects of intensity, bias voltage, and temperature on SNR. Section 7 concludes the chapter with a brief summary.

5.2 Experimental

The studied APDs are listed in Table 5.1. These include two units of different models from ID Quantique, two units of same model from Perkin Elmer, and two evaluation boards from ID Quantique again. These boards enable adjusting bias voltage and set temperature of the thermoelectric cooler separately via two screw potentiometers. A replaceable diode from the same manufacturer can be mounted on the board from a dedicated socket.

Referral name	Full commercial name	Specified dark counts (Hz)	Active area diameter (μm)
IDQ-20	ID Quantique id100-20, Ultra Low Noise	<2	20
IDQ-50	ID Quantique id100-50	<80	50
PE-1	Perkin Elmer SPCM AQRH-14H (Module SN: 19872)	62	170
PE-2	Perkin Elmer SPCM AQRH-14H (Module SN: 15973-1)	88	170
IDQ-D1 Board-1	ID Quantique id101-50 (Board + Diode; Board SN: 0800045D210)	111	50
IDQ-D2 Board-2	ID Quantique id101-50 (Board + Diode; Board SN: 0800042D210)	95	50

Table 5.1: APDs used in measurements, and some of their properties.

A power-stabilized HeNe laser was used as the light source (Spectra Physics 117A-2). Its beam was sent to an integration sphere through the tiny opening of an iris diaphragm located on one window. The photons scattered within the integration sphere then randomly impinged on the active areas of the APD's, located on other windows of the sphere. In cases where the scattered light was not sufficient, the APD was placed directly behind the diaphragm (for example when determining the saturation of ID Quantique id100-20 APD). The laser power reaching to the APDs was adjusted in the usual way using neutral density filters and a high quality polarizer. Data acquisition was done through serial port using a home-made counter card, and an application written in Visual Basic. For some measurements, a high-dynamic-range and high-linearity analog

photodiode (Hamamatsu; model information could not be provided) was used as a reference for APDs.

5.3 Dynamic Range

A sample dynamic range measurement, obtained from the PE-1 APD, is given in Figure 5.1. In addition to dynamic range, dark counts and linearity can also be determined from this curve. The horizontal axis in this graph shows the normalized laser power (normalized to its value without any attenuation), and the vertical axis shows the photon count rate read from the APD. The constant count rates in the low laser power region correspond to dark counts of the APD. With increasing laser power, count rates increase too and exhibit a linear dependency within a certain range. Following this linear range, count rates start not responding to further increase in laser power, indicating that the APD gets saturated.

Results of similar data with other APDs are summarized in Table 5.2. Dynamic range was taken as the ratio of the highest- to lowest value of the count rates (or laser power) within the linear region. The slope of a line fitted to data points having count rates from 10^2 (10 for IDQ-20) to 10^6 was used to quantify linearity. Based on Table 5.2, PE-1, PE-2, and IDQ-50 APDs show similar performance, while IDQ-20 has a wider dynamic range and fewer dark counts.

	Dark counts (Hz, μV)	Dynamic range	Linearity
IDQ-20	1 ± 0.3	10^5	1.06
IDQ-50	74 ± 9	10^4	1.07
PE-1	67 ± 1	10^4	1.07
PE-2	84 ± 1	10^4	0.95
Hamamatsu	$196\pm 5\mu\text{V}$	$>10^5$	0.96

Table 5.2: Comparison of the characterized APDs and the analog photodiode in terms of their dark counts, dynamic range and linearity.

5.4 Stability

The long term stability of the APDs was studied next. A sample data is presented in Figure 5.2. The graph shows as a function of time, the changes in count rates read from IDQ-20 and PE-1 APDs. The laser was off in the beginning of the measurement, and was turned on at the 34th second. Its power oscillated until 215th second, at which the control loop stabilizing its power has been started. Although the two APDs were positioned at identical windows of the integration sphere, and thus exposed to same intensity levels, the photon counts read from PE-1 were 700 times those of IDQ-20 (PE-1: 250kHz; IDQ-20: 350Hz). This difference was attributed to the size of active area of the APDs, and other design properties (such as quantum efficiency). In order to correct this difference, the count rates were normalized by their average value in the region of stable laser intensity (215-800s). For both APDs, the difference between count rates when the laser is off and on clearly indicates that they detect the laser. In addition, it is also seen that the counts generated by IDQ-20 are much noisier than those of PE-1. A simple calculation with raw (i.e. not normalized) count rates from 300-800s yields the SNR (mean divided by standard deviation) as $354/20 = 17.7$ for IDQ-20, and $2.534 \times 10^5 / 3.6 \times 10^3 = 71.3$ for PE-1.

From dynamic range analyses, it was known that the count rates of 250kHz and 350Hz for PE-1 and IDQ-20 respectively, lay within their linear ranges. However, in order to clarify that the difference in noise levels was not a misinterpretation originating from the difference in count rates, the measurement was repeated for each APD separately with (different) laser intensities adjusted to yield similar count rates (Figure 5.3). For the region where the laser has stabilized, the SNR was calculated as $2.27 \times 10^4 / 464 = 48.9$ for IDQ-20, and $2.53 \times 10^4 / 203 = 124.5$ for PE-1. To have similar counts on both APDs, IDQ-20 was exposed to a higher intensity as compared to the measurement of Figure 5.2, and as a result, the SNR was improved from 17.7 to 48.9. On the other hand, PE-1 was exposed to almost the same intensity, but its SNR was also improved (from 71.3 in Figure 5.2 to 124.5 in Figure 5.3.b). This is interpreted as the noise in PE-1 counts could be even smaller than the long term fluctuations in laser

intensity. The slight increase in the count rates of PE-1 in Figure 5.2 confirms this explanation. Note that this trend gets lost in the noisier count rates of IDQ-20.

5.5 Effects of Temperature and Bias Voltage on Detection Rate

This section presents measurements with the evaluation boards. These boards enable adjusting bias voltage of the diode and set temperature of the thermoelectric cooler separately via two screw potentiometers. The set- and current temperatures of the thermoelectric cooler are read respectively from the FB+ and FB- voltages on the board. Both voltages take values from 0 to 1300mV, with 0mV corresponding to no cooling. The bias voltage on the other hand can be read from the V_{op} voltage on the board, and takes values from -26.8 to -22.7V¹. The default settings for FB+ and V_{op} are 500mV and -25.3V respectively. During adjustments, it is recommended not to exceed 560mV for FB+, and to stay within -24.0 to -26.2V for V_{op} .

In initial trials with IDQ-D1 diode mounted on Board-1, dark counts were measured to be <100cps, however in a few hours observed to rise abruptly to \approx 600cps. Later measurements revealed that the FB- voltage read from the board corresponding to diode temperature remained fixed at \approx 1500mV, irrespective from changes in the set temperature (FB+ voltage). This was interpreted as a malfunction of the thermoelectric cooler that could have happened when the FB+ voltage was brought to a value outside the recommended range. Same type of measurement with IDQ-D2 diode mounted on Board-1 confirmed that the problem was with the diode, and not with the board.

The high dark counts of IDQ-D1 was tried to be brought back to its initial value by adjusting the bias voltage. The change of dark counts as a function of V_{op} is shown in Figure 5.4. The same measurement was also done in the presence of laser illumination, to better distinguish the minimum bias voltage required to generate electrical pulses from individual charge carriers. As seen in this plot, it was possible to obtain dark

¹ Unlike thermoelectric cooler temperature, there is no distinction between set and actual values for the bias voltage. The reason for this may be the much faster (almost instantaneous) response of bias voltage to changes made through the relevant potentiometer.

counts less than 100Hz, but the lack of control over diode temperature still remained as a problem.

A similar measurement was done with IDQ-D2 diode and for a set of laser intensities (Figure 5.5). The thermoelectric cooler was at its default temperature throughout the measurements ($FB^- = 501.98\text{mV}$). The minimum V_{op} voltage required to have non-zero detection rate turned out to be different for the two diodes (IDQ-D1: -23.4V ; IDQ-D2: -22.6V). Another difference was the fast increase in count rates of IDQ-D2 beyond $V_{op} = -26.2\text{V}$. This bias voltage is also one limit of the recommended range. After the measurements the bias voltage was brought back to its factory setting of $V_{op} = -25.3\text{V}$, and it was observed that the dark count rate also returned back to its specified value of $\approx 100\text{cps}$. This confirmed that exiting the recommended range for bias voltage did not cause any problems with the diode.

The effect of temperature on dark count rate was also studied. Figure 5.6 shows the change in the dark count rate of IDQ-D2 diode as a function of FB^- , measured using two different boards. The bias voltage during measurements was kept constant at the factory value of $V_{op} = -25.3\text{V}$. It is seen that dark counts decrease rapidly with increasing cooling. When the set temperature was brought to $FB^+ = 700\text{mV}$ (the right-most data point), the actual temperature was read to be $FB^- \approx 695\text{mV}$ for about 55s, but then FB^- started to decrease rapidly (i.e. the diode started to heat). Immediately after this change, the measurement was stopped in order not to cause any damage on the thermoelectric cooler. When the set temperature was brought back to its default value of $FB^- = 502\text{mV}$, the dark count rate returned to ≈ 100 again. Figure 5.6 also tests if the board has any effect on the measurements. As expected, different boards yielded consistent results with the same diode.

The count rate – temperature relation was also studied for cases, where laser light was detected. The bias voltage was again kept constant at $V_{op} = -25.3\text{V}$, and IDQ-D2 was used as the diode. The resulting count rate – temperature relation was plotted in Figure 5.7 for 4 different laser intensities. The data of Figure 5.6 was also added to this plot. It is seen that count rates become less dependent on temperature with increasing

signal levels. This shows that temperature affects predominantly the dark counts, and therefore its effect on the total count rate will be at most a few kHz, which is the highest dark count rate observed in Figure 5.6 (corresponds to no cooling, or in other words the room temperature case).

5.6 SNR in Detection with APDs

An intensity measurement done with a photon detector inevitably involves shot noise that is well described by Poisson distribution. If shot noise were the only type of noise in an APD reading, one would expect – based on Poisson distribution – the variance of a set of readings to be equal to the mean of this set. In other words the SNR would be equal to the square root of the signal. To test this idea, the dynamic range measurements' data (Figure 5.1 and Table 5.2) was replotted on logarithmic scales with the y-axis denoting SNR (i.e. standard deviation of a set of count rates divided by the mean count rate), and the x-axis as the signal (mean count rate), as shown in Figure 5.8 for IDQ-20 and PE-1 APDs. A line with slope $\frac{1}{2}$ and passing through (0,0) was also plotted for comparison (green line). For a square root relation between SNR and signal, the data points are expected to lie around this line. Each data point was calculated from a 20s-long measurement recorded with 1s resolution (i.e. each standard deviation and mean pair was calculated from a set of 20 count rates). For low count rates, the SNR-signal relation follows the $\frac{1}{2}$ slope line, indicating that the dominant form of noise is the shot noise. With increasing count rates, deviations occur from the Poisson distribution. These deviations are more pronounced for the IDQ-20 APD.

A similar analysis can be done on the data of Figure 5.5 to see the relation between SNR and bias voltage. In this graph, the data taken in the presence of laser illumination have common bias voltages (i.e. the x-coordinates of the data points of the top 5 curves are common). This makes it possible to recover a separate SNR versus signal relation for each bias voltage (albeit with 5 data points) from this graph. The graph in Figure 5.9 shows this analysis. Each different symbol in this graph corresponds to a particular bias voltage (there are 12 of them). The $\frac{1}{2}$ slope line was plotted again for comparison. The

data recorded with bias voltages until $V_{op} = -26.20V$ obey Poisson distribution for low count rates and start deviating from it at count rates around 10^4 . This behavior is similar to the one observed with IDQ-20 (see Figure 5.8). For bias voltages beyond $V_{op} = -26.20V$, the relation between SNR and count rates is considerably different than what one would expect from a Poisson distribution. Considering the sharp increase in dark counts for $|V_{op}| > 26.20V$ (see Figure 5.5), the same graph was also plotted (not shown) using dark-count-subtracted values, but the deviation from Poisson distribution for $|V_{op}| > 26.20V$ did not improve. This reveals that starting from $V_{op} = -26.20V$, other types of noise (for example thermal noise) are getting involved in APD's operation.

Similar to intensity and bias voltage, temperature dependence of SNR was also studied. For this purpose, the data of Figure 5.7 was replotted as an SNR versus detection rate relation in Figure 5.10. Each different symbol in this graph corresponds to a particular temperature. Although the number of datapoints is a little low, a similar conclusion can be deduced here too: The relation between SNR and detection rates obeys Poisson statistics at low detection rates ($<20kHz$), and deviates from it as the detection rates increase. In addition to SNR, the noise itself was also studied as a function of temperature. Table 5.3 lists results of measurements with the IDQ-D2 diode at various temperatures. The mean detection rate was kept constant at $\approx 5kHz$, a rate that corresponds to the Poisson region of Figure 5.10. As suggested by this list, temperature has no effect on standard deviations of rates. The last column presents the result of a similar measurement with PE-1 APD, which has significantly less noise.

FB- (mV) \pm std	Average photon rate (photons/s)	Photon rate standard deviation (photons/s)
250.186 \pm 0.004	5.1836×10^3	80
350.529 \pm 0.209	5.0174×10^3	79
450.808 \pm 0.113	5.0296×10^3	83
568.089 \pm 0.050	5.2004×10^3	84
PE-1 APD	5.1703×10^3	71

Table 5.3: Noise present in detection rates of IDQ-D2 diode at different temperatures, and PE-1 APD at its fixed operation conditions. Measurement time was 12 minutes for all cases.

5.7 Conclusion

Dynamic range, dark count rate, linearity, and stability of several APDs have been determined. The Perkin Elmer APDs were more stable as compared to IDQ APDs. Detection rate was studied as a function of bias voltage and temperature. While bias voltage had a dramatic effect on detection rate, temperature was important mainly for the dark counts. Afterpulses could not be studied quantitatively. SNR was analyzed as functions of intensity, bias voltage, and temperature. For all cases, SNR followed Poisson statistics at low count rates, and deviated from it as the count rate increased. The deviations have been interpreted as contributions from thermal noise sources. Perkin Elmer APDs were closer to Poisson statistics as compared to IDQ APDs.

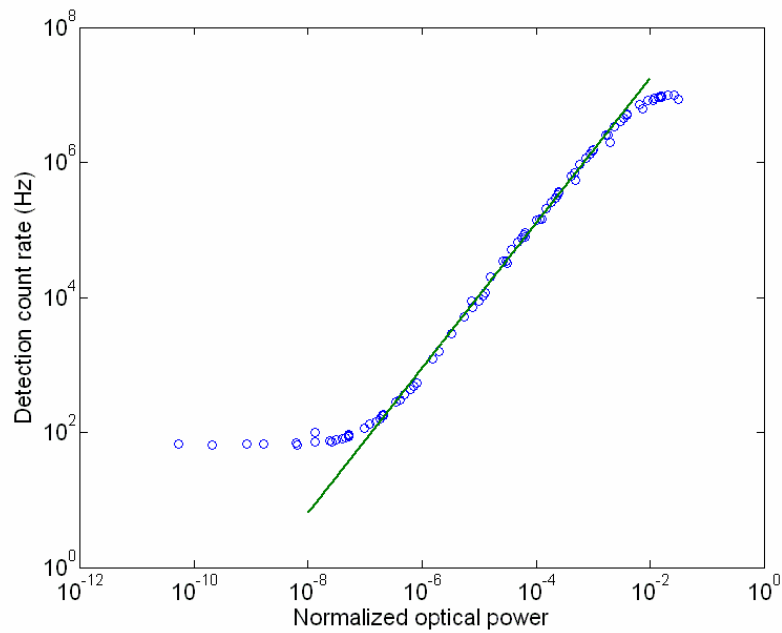


Figure 5.1: Detection rate as a function of normalized laser intensity for PE-1 APD. The green line is a fit to data points having count rates from 10^2 to 10^6 Hz. The graph reveals dynamic range, linearity, and dark counts of the APD. Each datapoint is obtained from a 20-s long measurement.

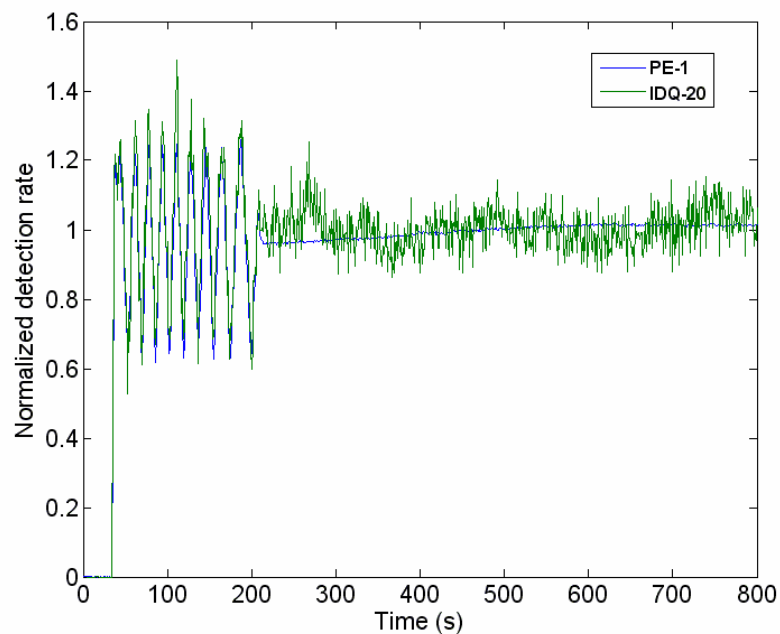


Figure 5.2: Comparison of IDQ-20 and PE-1 APDs for stability.

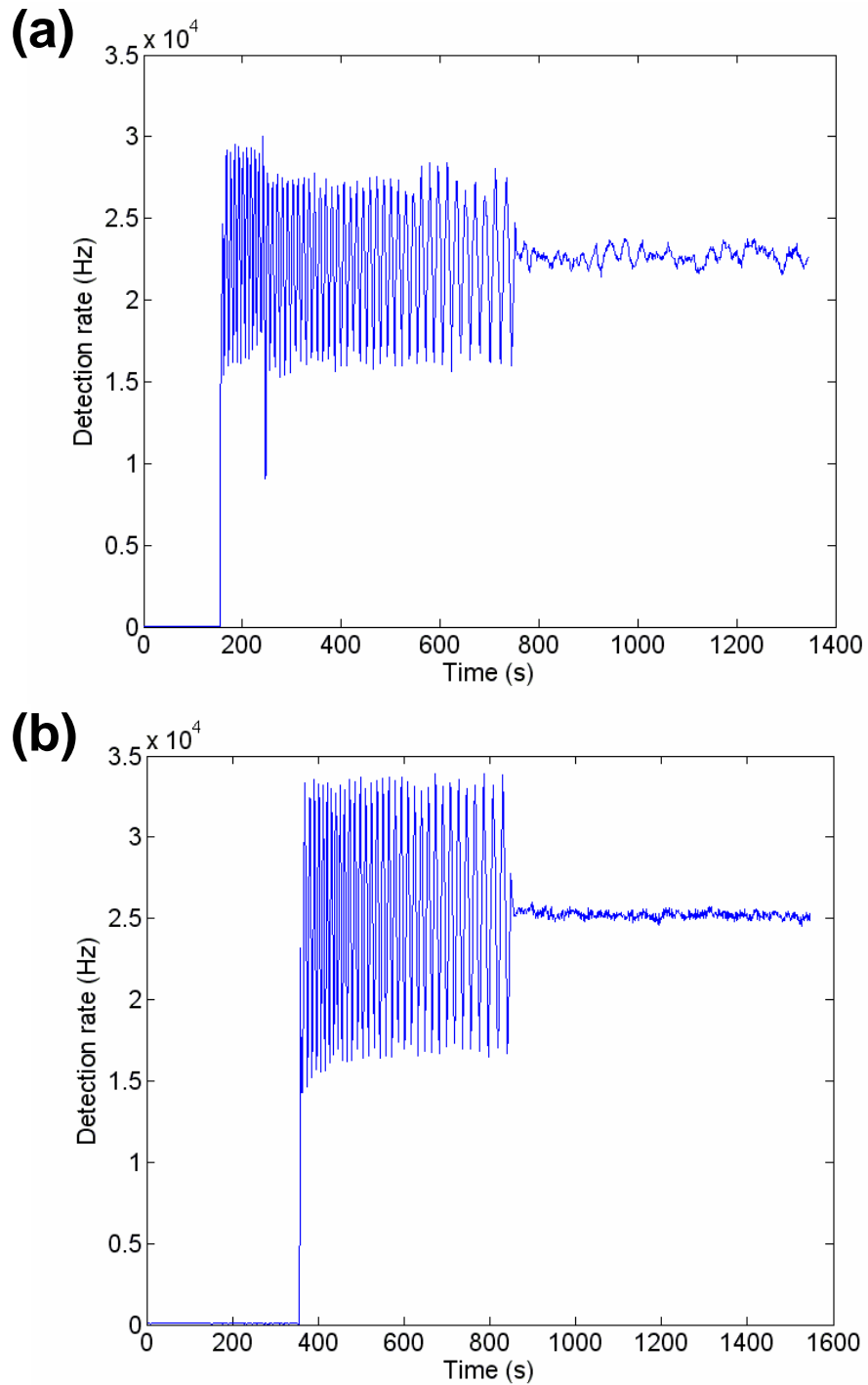


Figure 5.3: Comparison of (a) IDQ-20 and (b) PE-1 APDs for stability. Laser intensity was adjusted to yield similar count rates at both APDs.

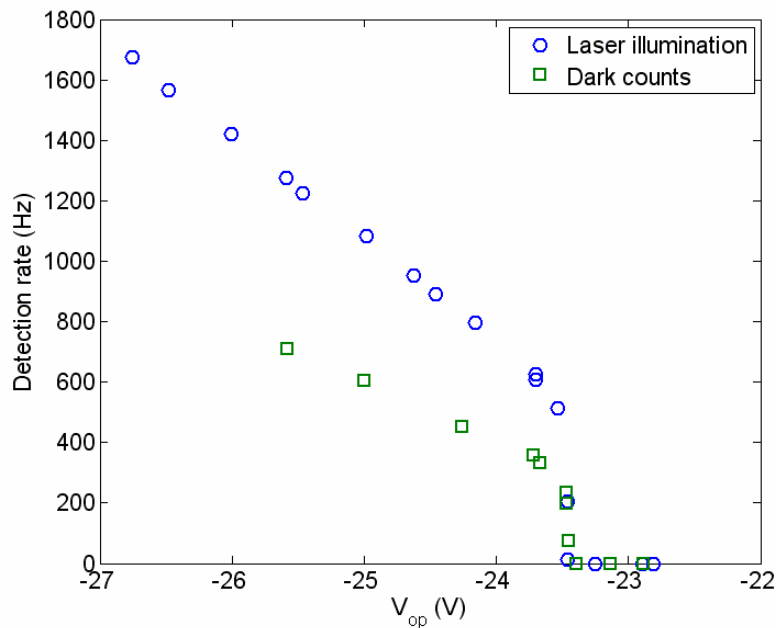


Figure 5.4: Detection rate as a function of bias voltage for IDQ-D1. Set temperature was at $FB+ = 560\text{mV}$, but discovered to have no effect on the actual temperature ($FB-$ fixed at $\approx 1500\text{mV}$).

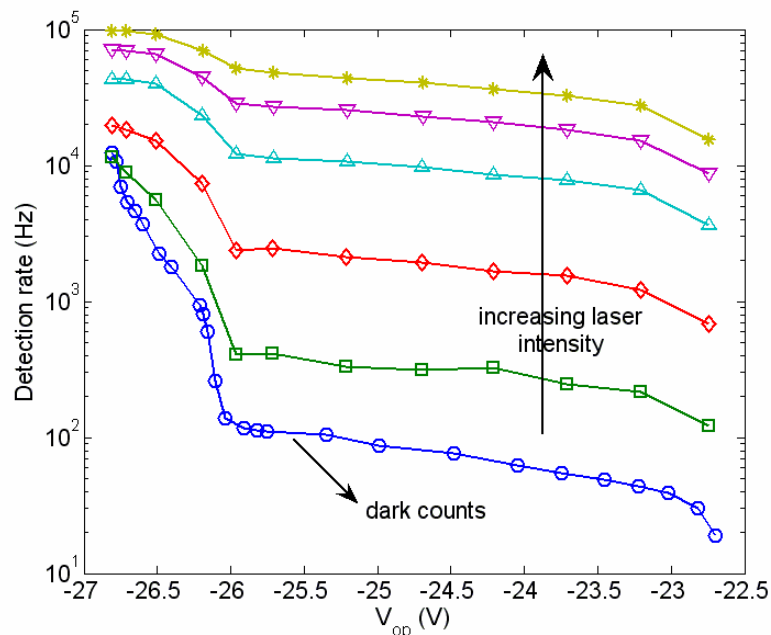


Figure 5.5: Detection rate as a function of bias voltage for IDQ-D2. Diode temperature was constant at $FB- = 501.98\text{mV}$. For all laser intensities, detection rate becomes 0 at $V_{op} = -22.6\text{V}$. The datapoints with 0 detection rate could not be shown due to logarithmic y-axis. Each datapoint is obtained from a 120s-long measurement.

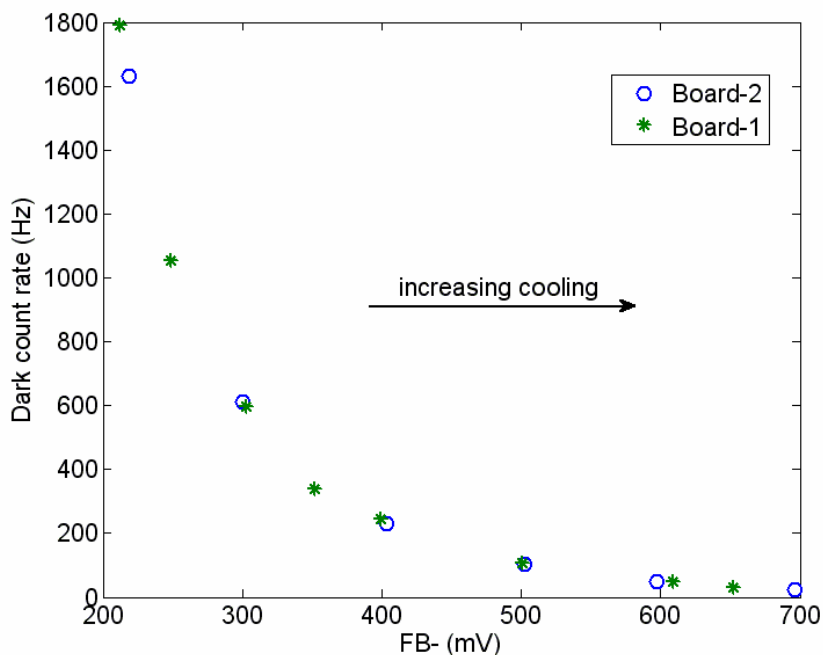


Figure 5.6: Dark count rate as a function of temperature for IDQ-D2. Bias voltage was constant at $V_{op} = -25.3V$.

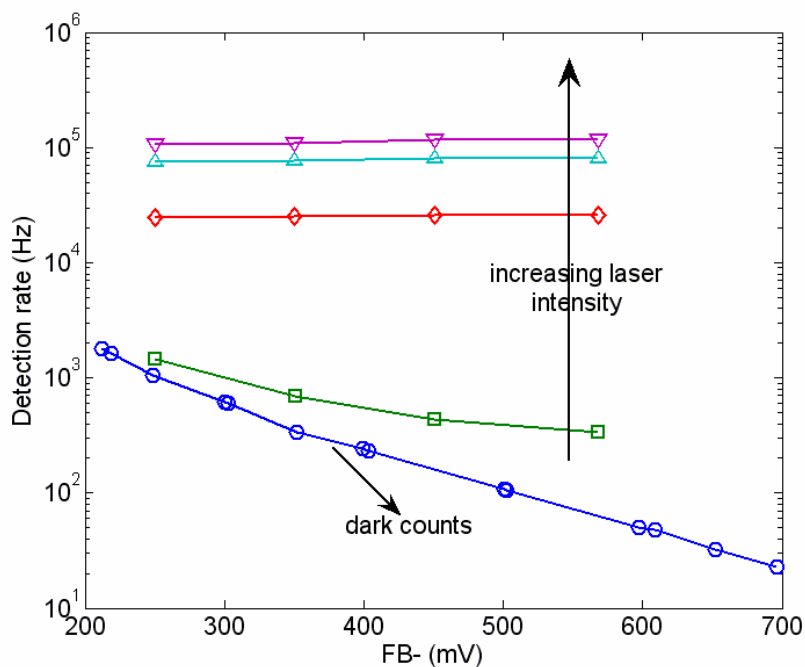


Figure 5.7: Detection rate as a function of temperature for IDQ-D2. Bias voltage was constant at $V_{op} = -25.3V$. Each datapoint is obtained from a 120s-long measurement.

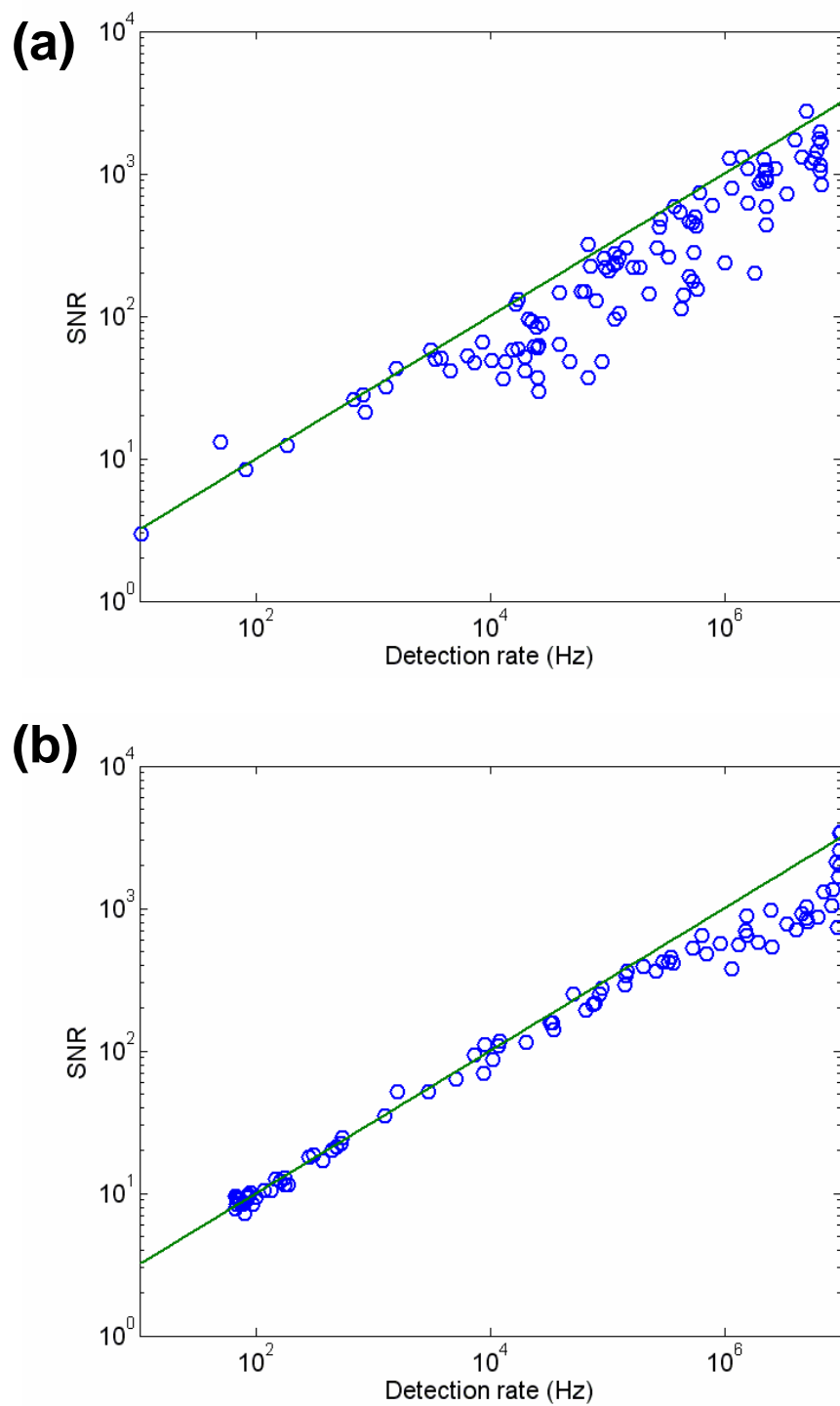


Figure 5.8: SNR as a function of detection rate for (a) IDQ-20, and (b) PE-1 APDs.

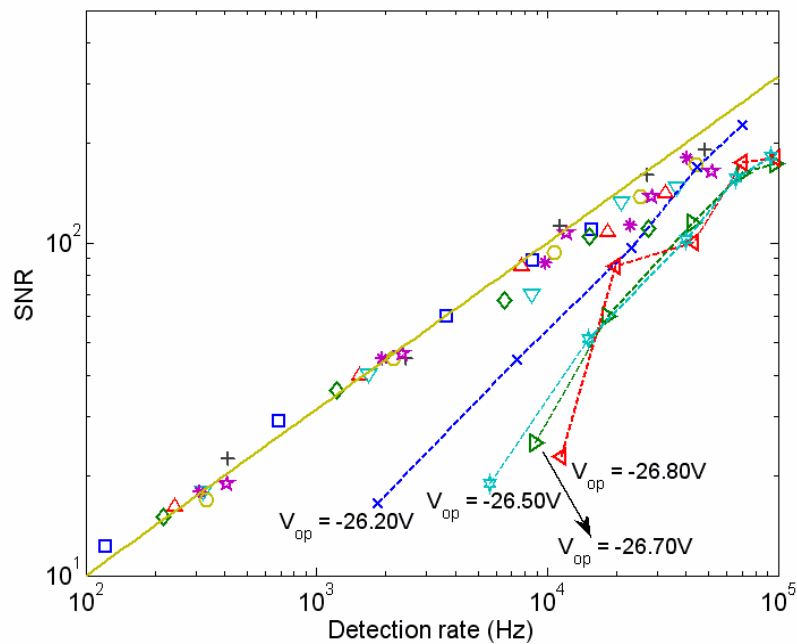


Figure 5.9: SNR as a function of detection rate for IDQ-D2 APD operated with different bias voltages.

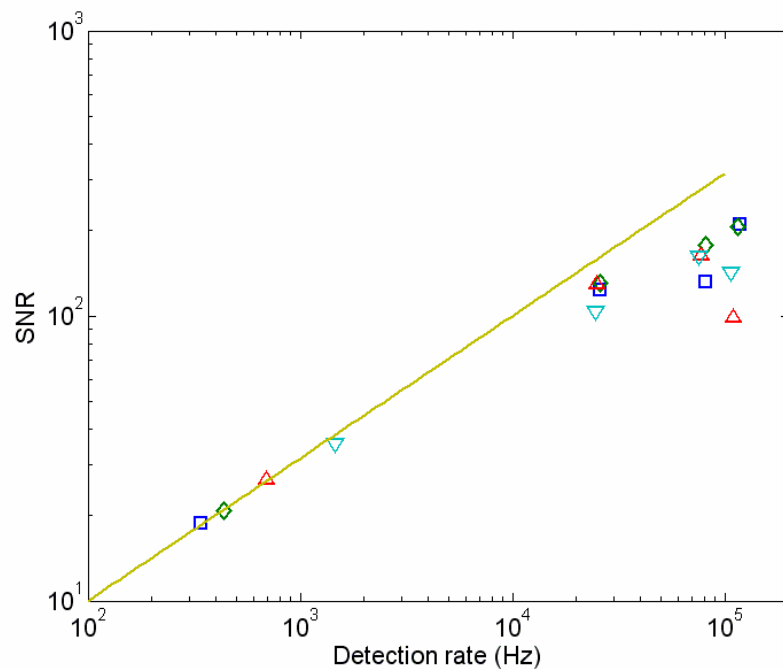


Figure 5.10: SNR as a function of detection rate for IDQ-D2 APD operated with different diode temperatures. Bias voltage was constant at $V_{op} = -25.3V$.

Chapter 6

CONCLUSION

This doctoral study was about single molecule experiments based on far field optical detection techniques. It involved both developing of the necessary infrastructure, and putting them into use for original research.

The infrastructure consists of a room temperature setup for wide-field imaging and confocal detection of single molecules, and a cryostat setup for low temperature experiments. The wide-field imaging can be done under both parallel and TIRF illuminations. A 1.49 NA oil objective and a state of the art EM-CCD camera are employed for this purpose. The confocal detection part uses a fast, closed-loop piezo scanner with capacitive position sensors and $30 \times 30 \times 10 \mu\text{m}^3$ scanning range to obtain confocal images of the sample and position a point of interest onto the focal spot. Possible point measurements include time trace recording, coincidence counting, and FCS. Detection is done via two APDs, which eliminates dead time in coincidence counting and FCS, and offers the possibility of two-channel operation in area scanning and time trace recording. Time trace recording can be done either synchronously or asynchronously with their benefits and drawbacks as summarized in Table 2.1. A special chamber was developed for FCS studies in volatile organic solvents. The cryostat system uses a pulse tube cooler, which brings a different design as compared to traditional bath cryostats. Some difficulties were encountered as described in Section 2.4, but these were related with the sample rather than the infrastructure. The cryostat can readily achieve 6K, suggesting that the time and effort invested in this setup are going to pay off soon with a change of the sample of interest. Self assembled quantum dots for example can be suitable for vacuum environment, as suggested by the use of electron microscopy for

their imaging. Although not a strict requirement, confocal imaging capability can be considered as a future extension to this setup. The excitation sources include a 532nm cw diode laser, a tunable subpicosecond pulsed fiber laser (Toptica FSS) with tunability range from 520-700nm and repetition rate of 80MHz, and a mode-locked Ti:Sa laser with second harmonic generation extension and again 80MHz repetition rate. There is also a 750mm focal length monochromator equipped with a spectroscopy camera that can be used interchangeably between room and low temperature setups.

After finishing with the infrastructure, the confocal detection part of the room temperature setup was used for characterizing fluorescence properties of single terrylene molecules embedded in anthracene thin films. This guest-host system has not been studied at room temperature before. The films were prepared by spin-coating on glass substrates. Polarization dependent fluorescence measurements on the single molecule level revealed that terrylene molecules were oriented nearly in-plane with the anthracene film. Typical measured fluorescence lifetime of terrylene was 3.6ns, and photon count rate at saturation was 750kHz. A statistical analysis of 104 molecules indicated that on average 1.6×10^6 photons can be detected from a single terrylene molecule before it photobleaches. These results rendered terrylene-anthracene a promising guest-host system for room temperature single molecule experiments.

Another original topic has been studied with the wide-field part of the room temperature setup. The motivation of this study was to improve position estimation in SMT. In order to achieve this, a new imaging model was proposed that takes into account the motion of the molecule during the exposure time of a frame. Since this model better represented the real imaging process, it yielded more accurate position estimates for a moving molecule as compared to models assuming stationary emitters. As inherently including motion, the proposed model also allowed molecules' velocity to be estimated from single frame data. The model parameters were estimated by a maximum likelihood algorithm, where the Poisson nature of the photon emission and detection events was used to derive the likelihood function. The position and velocity estimates obtained from individual frames were further fed into a Kalman filter for

tracking. The performance of the algorithm was evaluated by CRLB calculations, simulations, and model experiments with a piezo-stage. Tracking of molecules moving as fast as 7pixels/frame (12.6 μ m/s) has been demonstrated within a mean error of 0.42pixel (37.43 nm).

The thesis also involved characterization of APD detectors. Dynamic range, dark counts, linearity and stability of several APDs were studied. Commercial evaluation boards were used to gain insight about the roles of bias voltage and diode temperature in the operation of an APD. While bias voltage had significant effect on count rates both in the presence and absence of illumination, the effect of temperature was limited to the dark counts. The noise–signal relation obeyed Poisson statistics up to some signal level, and started deviating from it afterwards. This has been interpreted as other sources of noise appearing in addition to the inherent shot noise.

In conclusion, this doctoral study leaves behind valuable infrastructure and original scientific contributions to the field of single molecule research. These will hopefully be benefited in future experiments as well.

Appendix A

USER'S MANUAL FOR THE CONFOCAL SETUP SOFTWARE

A.1 Introduction

Confocal Setup Software is a program for sample scanning confocal microscopy, time correlated single photon counting, and fluorescence correlation spectroscopy. It is a common platform for realizing measurements, keeping record of relevant parameters, data retrieval and analysis. This appendix is intended to be a manual for the everyday user (technical details can be found in Chapter 2). It starts with an overview of the basic concepts and parts within the program. The interfaces for various types of measurements are explained next, and followed by a section on analyses.

A.2 Overview

A.2.1 Data Handling

A session is a concept introduced for data handling within the program. It refers to a collection of measurements or analyses brought together under a common name, to be called `SessionName` hereafter. Each session comprises a binary registry file with extension `*.s` (i.e. `SessionName.s`), and an associated folder to this file with name `SessionName_Files`. The registry file stores relevant parameters for all the measurements or analyses within the session, whereas the folder serves as a place to record or call back the raw data.

For proper operation of the program, the `*.s` file and its folder should be located in the same directory, and their names should preserve the original format (i.e. `SessionName.s`, and `SessionName_Files`). As long as these restrictions are met, they can be copied to other directories or renamed (i.e. the `SessionName` part) as appropriate. Likewise, the user can continue working with the same session at different times. For example he can keep taking his measurements over a week to the same session, or analyze his data afterwards.

A.2.2 Getting Started

The program can be started either directly by double-clicking on the Windows self-executable file (extension: `*.exe`), or through Matlab by running the script file (extension: `*.m`). It may take about a minute for NI-DAQmx library to be loaded and

necessary interfaces to be generated. A splash box appears during this period to provide feedback to the user, so that he doesn't click/run the program file multiple times.

Two warning messages may appear at this stage:

- i) The *Library not found* warning shown below appears if the NI-DAQmx library is not installed on the computer¹. In this case the program can be used for viewing or analyzing previous data, but not for acquiring new data.

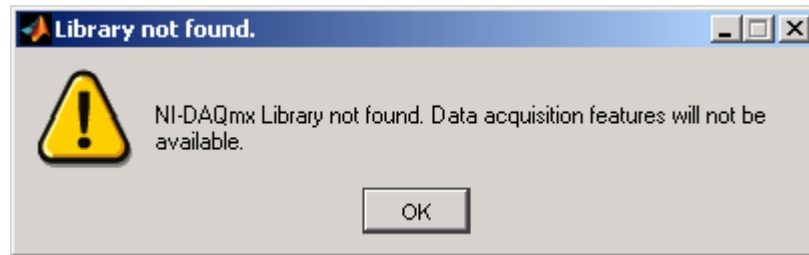


Figure A.1: *Library not found* warning.

- ii) The *Scanner not ready* warning shown below appears if the scanner is off, or any of the offsets is negative. More information about offsets is provided in section A.3.1. After confirming this warning, if the user will not need the scanner in his measurements, he continues without any further steps. On the other hand if his measurements require the scanner, before starting measurements, he must follow **Settings > Scan** in the menu, and have the offset read (described in section A.3.1).



Figure A.2: *Scanner not ready* warning.

When the program is ready, a large window entitled *Confocal Setup Software* appears, as shown in Figure A.3: This is the top-level window within the program, and covers the whole screen, assuming that the Windows toolbar is in its default configuration (i.e. visible, single line, and located at the bottom of the screen). The *Confocal Setup Software* window consists of three separate panels, and a menu bar.

¹The program assumes that if NI-DAQmx library is installed on a computer, it is the computer to be used for measurements (i.e. it has a PCIe-6363 data acquisition card as Device-1).

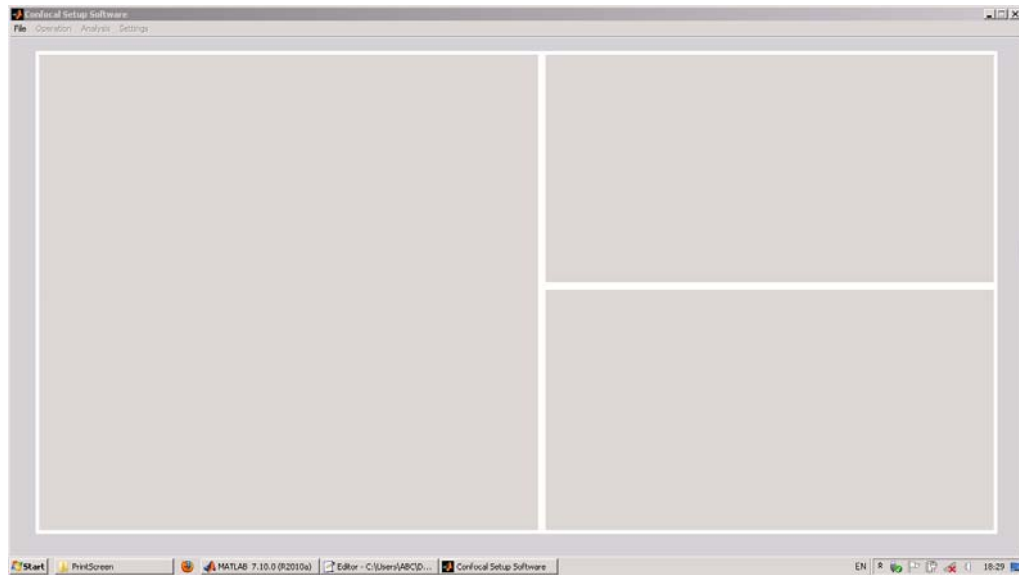


Figure A.3: Blank *Confocal Setup Software* window.

The larger panel on the left is the *main panel*. Most of the actions within the program take place in this panel. These include device control, data acquisition, real-time displaying, or retrieving data. The *main panel* attains different configurations based on the type of measurement or data. In general, it includes an axes and relevant control buttons. The top panel on the right is the *information panel*. It is essentially a textbox that displays the properties of a measurement or analysis that is either currently being done, or present in the session. The bottom panel is the *explorer panel*, and provides access to all the measurements or analyses within the session. More information on the *explorer panel* will follow as its components become visible.

The menu bar, located at the top, is activated by mouse clicks. Clicking a menu displays a pull-down list below it, which remains displayed until: i) an item on the list is selected, ii) another menu is pulled down, or iii) anywhere else in the screen is clicked. Some of the menu items can also be activated by their accelerators (i.e. Ctrl + Letter, indicated next to them). The menus and their items are given in the following table.

File	Operation	Analysis	Settings
New Ctrl+N	Z Scan	Correlation	Scan
Open Ctrl+O	Area Scan	FCS Fitting	Time Trace
Export	Time Trace		TAC
Exit	TCSPC		
	FCS		

Table A.1: Menus, and their items in the *Confocal Setup Software*.

When the program starts, only the **New**, **Open**, and **Exit** items of the **File** menu is active; all the remaining menus/items in the above list are inactive (indicated by their

gray color). This compels the user to take one of the following actions: i) start a new session, ii) open an existing session, or iii) quit the application.

When the **New** item is clicked, a standard dialog box entitled *Save As* appears to select or create the directory, and give the session name.

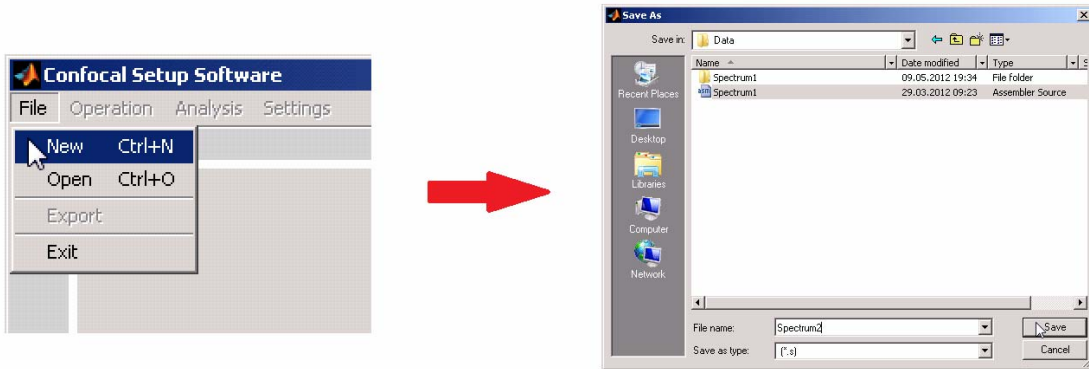


Figure A.4: Starting a new session.

Upon clicking **Save** in the *Save As* window, the session file and folder (Spectrum2.s, and Spectrum2_Files for the above example) are generated within the selected directory², and the blank *Confocal Setup Software* window (Figure A.3) takes the following form shown in Figure A.5:

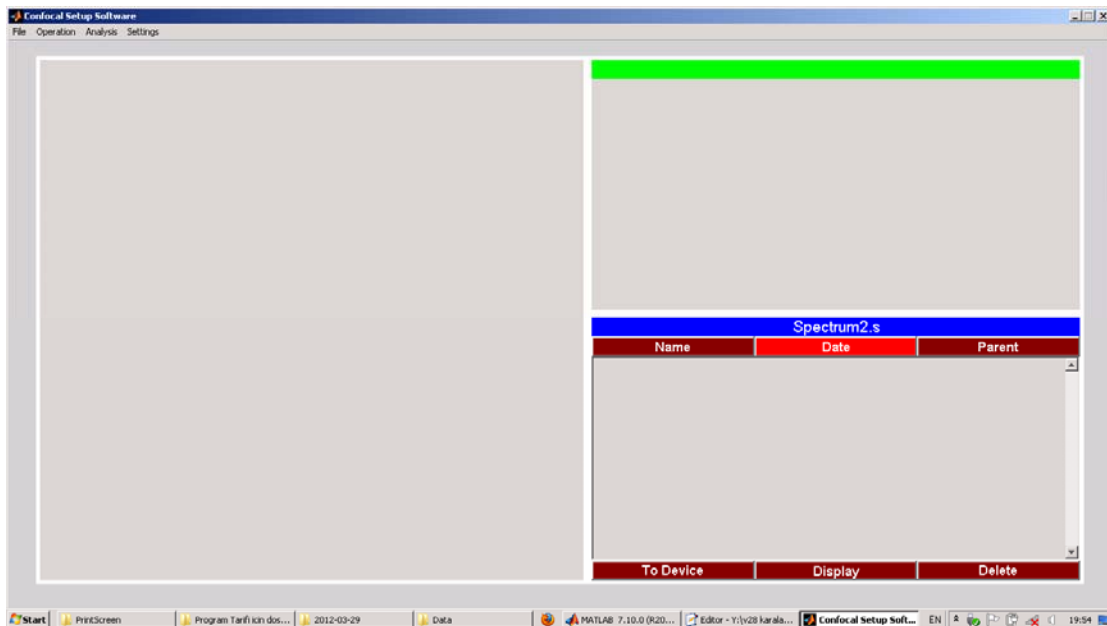


Figure A.5: *Confocal Setup Software* window, after a new session is defined.

² The user is warned in case of overwrite.

Once a new session is defined, other applicable menus/items become active, a green title bar appears in the *information panel*, and all the components of the *explorer panel* become visible with the session name displayed in the blue title bar. Since there are yet no measurements in the session, the *explorer panel's* list and the *information panel* remain blank.

In alternative to defining a new session, the user may also prefer to work with an existing one. In this case, he clicks on **File > Open** in the menu. This brings a standard dialog box with title *Select a session file*, to select the directory and the session to open.

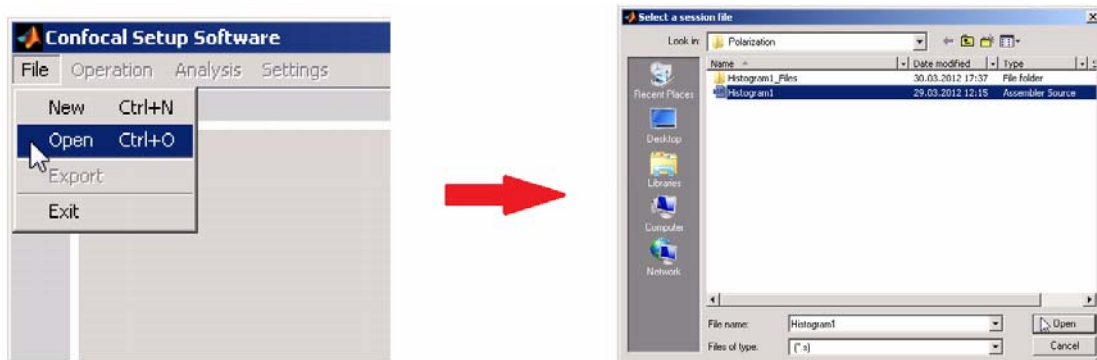


Figure A.6: Opening an existing session.

Upon clicking **Open** in the *Select a session file* window, the selected session opens, and the blank *Confocal Setup Software* window (Figure A.3) takes the following form shown in Figure A.7:

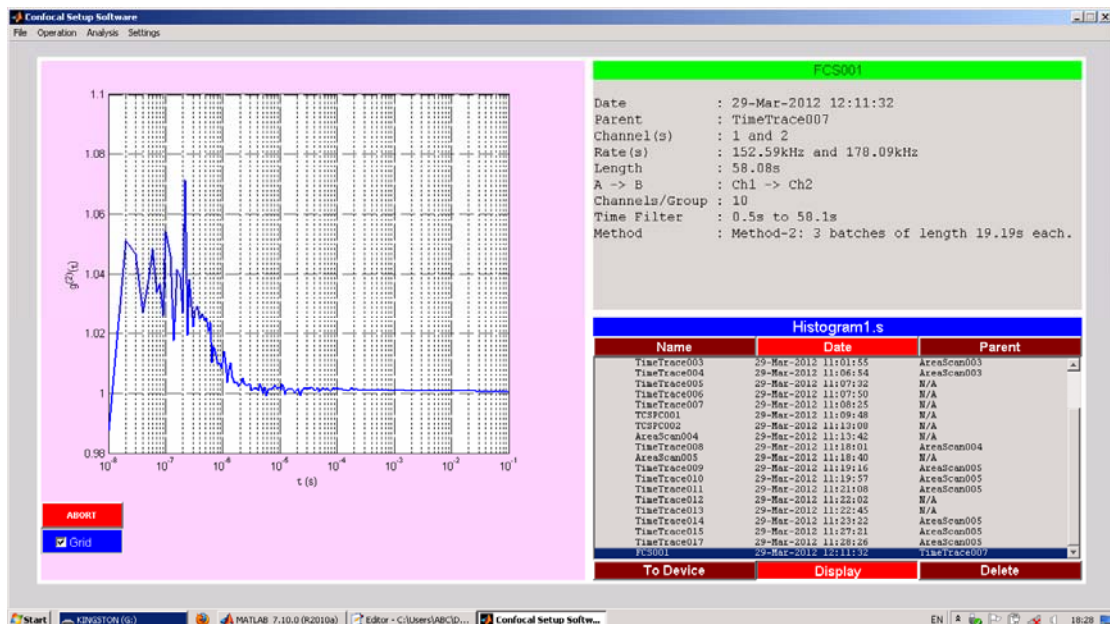


Figure A.7: *Confocal Setup Software* window, after an existing session is opened.

When an existing session is opened, all the measurements or analyses within that session are listed in the *explorer panel*. The last one of these measurements or analyses is displayed in the *main panel*, and the relevant experimental details are provided in the *information panel*.

A.2.3 Explorer panel

At this stage it will be convenient to describe the *explorer panel* in more detail over a magnified view (Figure A.8).

Histogram1.s		
Name	Date	Parent
TimeTrace003	29-Mar-2012 11:01:55	AreaScan003
TimeTrace004	29-Mar-2012 11:06:54	AreaScan003
TimeTrace005	29-Mar-2012 11:07:32	N/A
TimeTrace006	29-Mar-2012 11:07:50	N/A
TimeTrace007	29-Mar-2012 11:08:25	N/A
TCSPC001	29-Mar-2012 11:09:48	N/A
TCSPC002	29-Mar-2012 11:13:08	N/A
AreaScan004	29-Mar-2012 11:13:42	N/A
TimeTrace008	29-Mar-2012 11:18:01	AreaScan004
AreaScan005	29-Mar-2012 11:18:40	N/A
TimeTrace009	29-Mar-2012 11:19:16	AreaScan005
TimeTrace010	29-Mar-2012 11:19:57	AreaScan005
TimeTrace011	29-Mar-2012 11:21:08	AreaScan005
TimeTrace012	29-Mar-2012 11:22:02	N/A
TimeTrace013	29-Mar-2012 11:22:45	N/A
TimeTrace014	29-Mar-2012 11:23:22	AreaScan005
TimeTrace015	29-Mar-2012 11:27:21	AreaScan005
TimeTrace017	29-Mar-2012 11:28:26	AreaScan005
FCS001	29-Mar-2012 12:11:32	TimeTrace007

To Device Display Delete

Figure A.8: Magnified view of the *explorer panel*.

The *explorer panel* consists of a blue title bar that shows the name of the current session, a list box with a slider that provides access to all the measurements or analyses within the session, and six buttons organized in two groups at the top and bottom of the list box. The buttons on the top row (**Name**, **Date**, and **Parent**) are toggle buttons that both serve as headers to the name, date, and parent columns of the list box, and also used to sort them according to one of these attributes. The active attribute for sorting takes a red color, while others remain brown. The user can change the active attribute for sorting by clicking on the desired button. Default attribute is **Date**. The measurement/analysis names are given based on type of the measurement/analysis, and they are not editable. Therefore sorting by name is equivalent to sorting by type.

The buttons on the bottom row are for different purposes. The **To Device** pushbutton applies the parameters of a previously recorded measurement as the current values. It is intended to be used in cases where the user wants to take a measurement with the same parameters as those of a previous one. Instead of changing all the parameters manually, he can select a suitable measurement from the list, and press **To Device**.

The **Display** toggle button is to display a measurement or analysis in the session. This is not to be confused with the parameters of the measurement/analysis. The parameters always appear in the *information panel*, regardless of the **Display** toggle button. In addition, when **Display** is pressed (i.e. when it has red color), the data of a measurement/analysis selected in the list is displayed in the *main panel*. When **Display** is depressed (i.e. when it has brown color), the data is not displayed in the *main panel*; only the parameters appear in the *information panel*. Note that depressing **Display** just turns off the display mode, but does not clear the *main panel*. Therefore the user must make sure that the **Display** button is red, before relating the data in the *main panel* to the selected measurement/analysis in the list, or to the parameters in the *information panel*. The **Display** button gets automatically depressed during any type of data acquisition.

The **Delete** pushbutton is to delete a measurement or analysis in the session. This action deletes the raw data from the session folder, and modifies the session file accordingly. The numbers of the remaining measurements/analyses remain unaltered. For example, `TimeTrace016` was apparently deleted in Figure A.6, but this did not make `TimeTrace017` renamed as “TimeTrace016”. The **Delete** button should be used with extreme care. Pressing this button deletes the selected measurement/analysis permanently, and without any further confirmation.

A.3 Data Acquisition Settings

For all the measurements in the program, the experimental parameters can be accessed either under the relevant **Settings** menu item, or from the **Options** button of the corresponding interface to be displayed on the *main panel*. The **Settings** menu items are devoted for more fundamental parameters, that are likely to remain in their default values for most of the time, or rarely changed throughout a session. The **Options** button on the other hand provides access to parameters that will be changed more frequently, as for example at every measurement. The parameters under the **Settings** menu items also have higher precedence: Changes in some of these parameters may affect other parameters given access by the **Options** button, but not vice versa.

As shown in Table A.1, the **Settings** menu has the **Scan**, **Time Trace**, and **TAC** items. Clicking on these items brings up the *Area Scan Settings*, *Time Trace Settings*, and *TAC Settings* windows respectively. A description of the settings in these windows will be given next.

A.3.1 Area Scan Settings

The *Area Scan Settings* window shown in Figure A.9 contains the following controls as explained below:

- **Points/pixel** edit box: Scanning task is performed via waveforms (i.e. position versus time data) commanded to the piezo stage. The Points/pixel parameter determines the number of points in a waveform. The higher the Points/pixel parameter, the more the data points, and consequently the smoother the

waveform becomes. By the same token, a lower Points/pixel parameter results in a more “step-wise” waveform. Points/pixel can take integer values between 1 and 20. The default value is 20. This parameter also applies for the Z Scan.

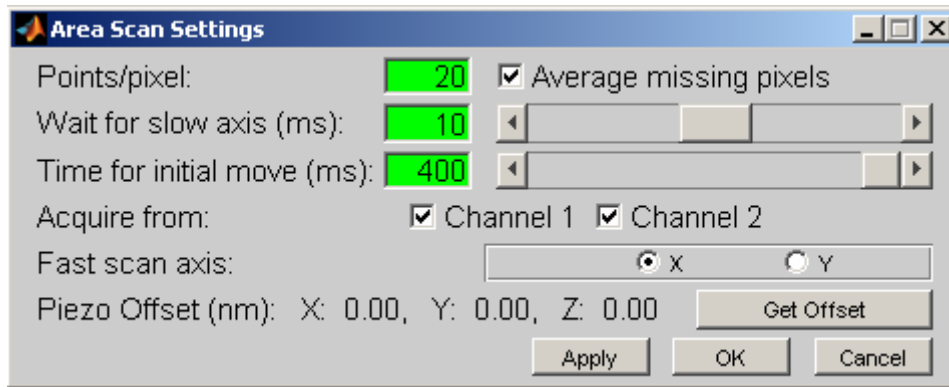


Figure A.9: Area Scan Settings window.

- **Average missing pixels** checkbox: There is always a mismatch between the commanded waveform, and the actual path of the scanner. In some cases, like small pixel sizes or fast scan speeds, the scanner may not spend time uniformly on each pixel, and may even totally miss some of them. When this option is checked, such missing pixels are attained the average value of their 4 (3 or 2 when the missing pixel is at the edges or on the corners) neighboring pixels. The averaging is done after the image is acquired. This parameter also applies for the Z Scan.
- **Wait for slow axis** edit box and slider: This parameter controls the time (in ms) that the fast axis waits at line edges, for the slow axis to step to the next line. Available values are between 0.1 and 20 ms, with the default value being 10 ms. The **Wait for slow axis** parameter can be set either from the edit box with arbitrary resolution, or from the slider with 5 ms coarse- and 1 ms fine resolutions.
- **Time for initial move** edit box and slider: This parameter controls the time (in ms) that the scanner moves to the starting point of the scanning task (lower left corner of the image to be scanned). Available values are between 2 and 400 ms, with the default value being 400 ms. The **Wait for slow axis** parameter can be set either from the edit box with arbitrary resolution, or from the slider with 50 ms coarse- and 5 ms fine resolutions. This parameter also applies for the point measurements (in positioning of the scanner to the desired point), and Z Scan.
- **Acquire from** checkboxes: These checkboxes are for selecting channels to be used in data acquisition. An unavailable channel can be disabled here to save run time and disk space. When a channel is disabled, all the features associated with this channel are grayed-out in the rest of the program. At least one channel

should be enabled. The same control can also be accessed through the *Time Trace Settings* window.

- **Fast scan axis** button group: Using radio buttons, either the **X** or the **Y** axis can be set as the fast scan axis. X-axis is the default selection.
- **Get Offset** pushbutton: Reads the offset between the commanded and actual positions³, and displays the result on the same line. Since this offset is going to be taken into account in all coming scanner tasks, the program checks for it automatically when it starts. The program can correct only positive offsets, and throws the warning message of Figure A.2 if the scanner is off, or any of the offsets is negative. To read the offsets, the user must turn on the scanner and click on **Get Offset**. If the warning message appears again, he must adjust the offset potentiometers on the scanner controller to have a positive offset. The offsets will be displayed only when all of them are positive, and will be assumed to be zero otherwise. It is a good practice to start from higher values, click on **Get Offset**, adjust the potentiometers, click on **Get Offset** again, and repeat this procedure until the offsets are ~ 50 nm.
- **Apply** pushbutton: Applies the changes.
- **OK** pushbutton: Applies the changes, and closes the *Area Scan Settings* window.
- **Cancel** pushbutton: Ignores the changes, and closes the *Area Scan Settings* window. The “close window” button on the upper right corner is equivalent to **Cancel**.

A.3.2 Time Trace Settings

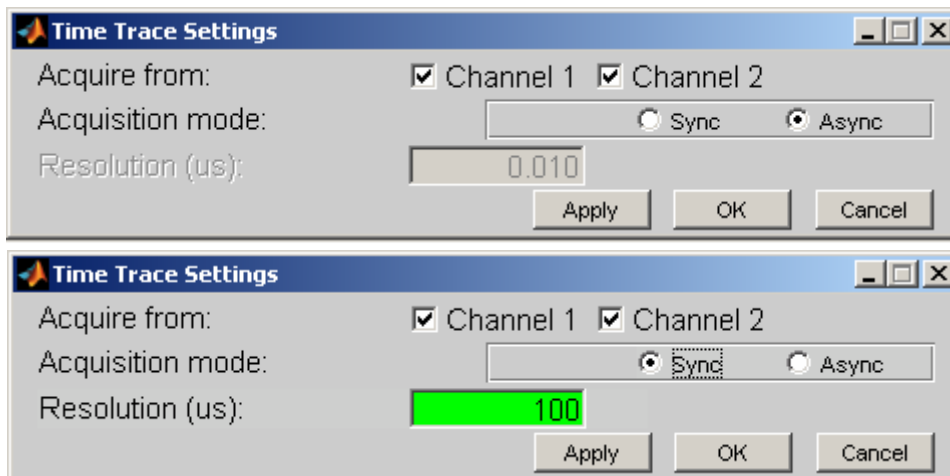


Figure A.10: *Time Trace Settings* window, with the **Acquisition mode** selected as **Async** (top) and **Sync** (bottom).

³ Offset is defined as (actual position) – (commanded position).

The *Time Trace Settings* window shown in Figure A.10 contains the following controls as explained below:

- **Acquire from** checkboxes: These checkboxes are for selecting channels to be used in data acquisition. An unavailable channel can be disabled here to save run time and disk space. When a channel is disabled, all the features associated with this channel are grayed-out in the rest of the program. At least one channel should be enabled. The same control can also be accessed through the *Area Scan Settings* window.
- **Acquisition mode** button group: Using radio buttons, either synchronous (**Sync**) or asynchronous (**Async**) acquisition modes can be selected. **Async** is the default selection.
- **Resolution** edit box: Sets the time resolution of synchronous acquisition. Allows values between 1 μ s and 1 s with 1 μ s resolution. Default value is 100 μ s. Changes in resolution may cause changes in binning and window times in the *Time Trace Options* window. The order of precedence is resolution > binning > window (see Section A.4.3). When the acquisition mode is **Async**, the **Resolution** edit box gets disabled and displays a fixed resolution of 0.01 μ s (Figure A.10; top).
- **Apply** pushbutton: Applies the changes.
- **OK** pushbutton: Applies the changes, and closes the *Time Trace Settings* window.
- **Cancel** pushbutton: Ignores the changes, and closes the *Time Trace Settings* window. The “close window” button on the upper right corner is equivalent to **Cancel**.

A.3.3 TAC Settings

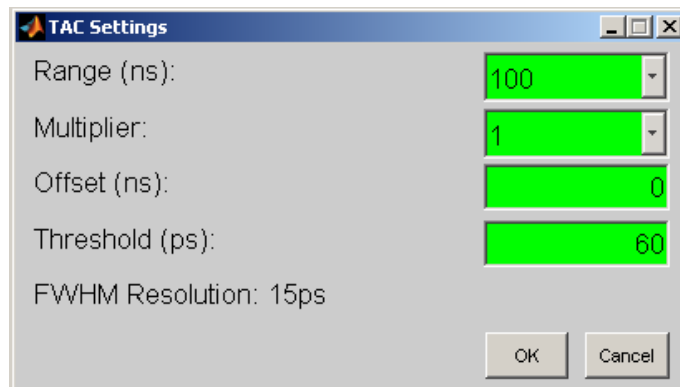


Figure A.11: *TAC Settings* window.

The *TAC Settings* window shown in Figure A.11 contains the following controls as explained below:

- **Range** pull-down list: The user selects the “TAC range” set on the device. Default selection is 100 ns.
- **Multiplier** pull-down list: The user selects the “TAC multiplier” set on the device. Default selection is 1.
- **Offset** edit box: The delay between start and stop channels can be entered.
- **Threshold** edit box: Coincidences with time elapsed between their Start-Stop events less than **Threshold**, are not counted.
- **FWHM Resolution**: Shows the specified TAC resolution with current **Range** and **Multiplier** choices.
- **OK** pushbutton: Applies the changes, and closes the *TAC Settings* window.
- **Cancel** pushbutton: Ignores the changes, and closes the *TAC Settings* window. The “close window” button on the upper right corner is equivalent to **Cancel**.

It is important to note that the **Range** and **Multiplier** pull-down lists in the *TAC Settings* window are for providing the experimental conditions to the program. They do not introduce any changes on the hardware. The user must make sure that the selections in the *TAC Settings* window are consistent with the actual settings. In order to facilitate this, a reminder window appears in case of a change in the **Range** or **Multiplier** parameters.

A.4 Measurements

The **Operation** menu involves various types of measurements. These can be classified in two groups as scanner measurements and point measurements. The scanner measurements **Z Scan** and **Area Scan** require a piezo scanner. The point measurements **Time Trace**, **TCSPC**, and **FCS** do not necessarily require a scanner, but can be performed at specific positions within the sample, in the presence of a scanner. The different type of measurements will be described below.

A.4.1 Z Scan

The **Z Scan** measurement mode is designed for intensity versus position measurement along the optical axis. This can be useful for determining the depth resolution of the setup, or measuring the thickness of $\sim\mu\text{m}$ -thick films. The measurement mode is activated by clicking **Operation > Z Scan**. This brings the **Z Scan** interface to the *main panel* (Figure A.12), which consists of an axes box and several control buttons:

The controls in the **Z Scan** interface are explained below:

- **Axis** box: Shows the Intensity (in counts/pixel) versus z-position (in micrometers) data. Y-axis scales automatically depending on the data and **DISPLAY** checkboxes.
- **FIT** pushbutton: Fits a 1-D Gaussian function to the acquired z-profile. Remains disabled until the data is available. The Gaussian is plotted (in green color) together with the data. Its FWHM and center are also displayed in the axis box.

- **SCAN** pushbutton: Starts Z Scan. Disabled during scanning; enabled otherwise.
- **ABORT** pushbutton: Aborts Z Scan. The aborted profile is still recorded with the pixels beyond aborting given zero intensity. Enabled during scanning; disabled otherwise.

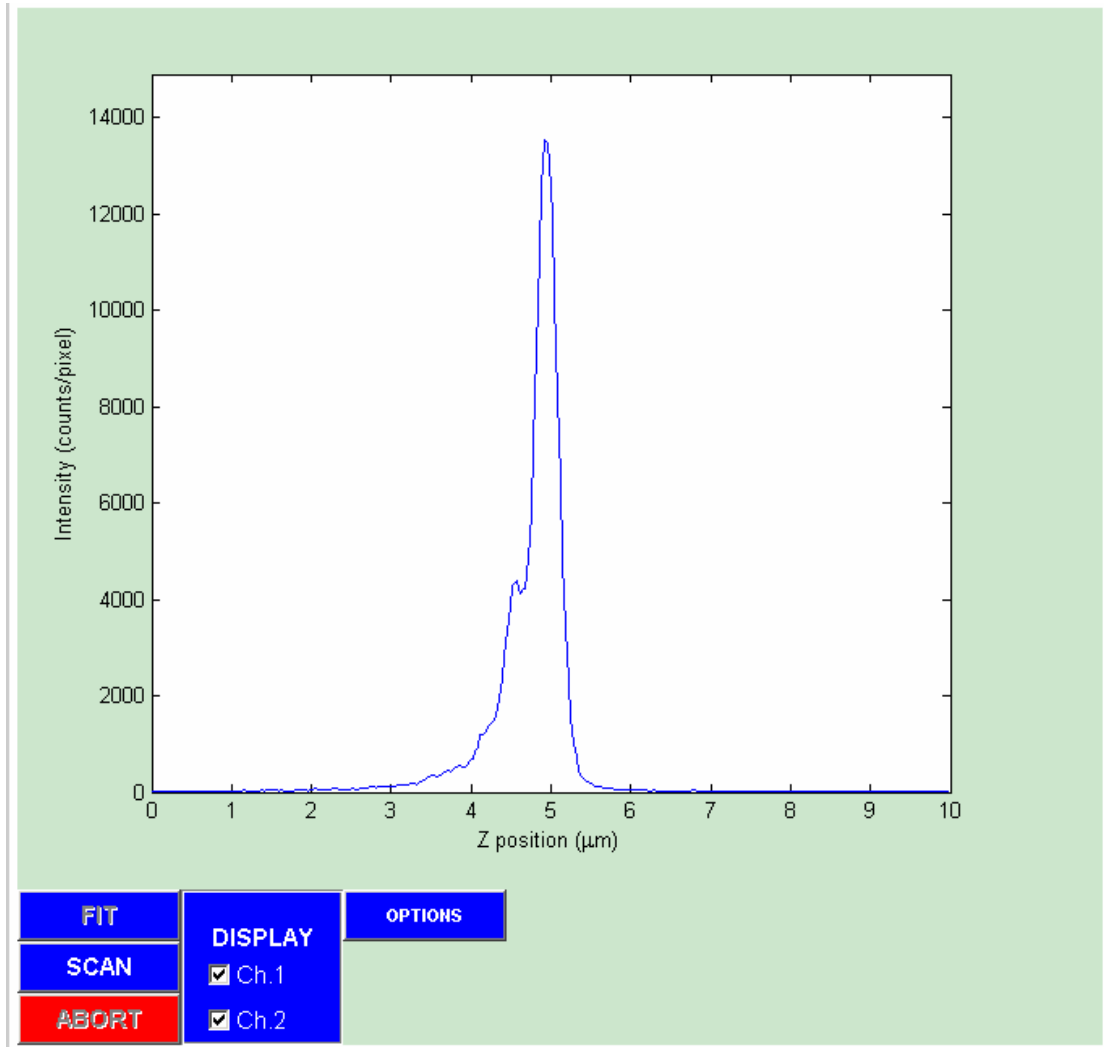


Figure A.12: Z Scan data acquisition interface displayed on the *main panel*.

- **DISPLAY** panel: Contains **Ch.1** and **Ch.2** checkboxes, to control the channel(s) to be displayed on the axis box. While the panel itself is enabled all the time, a checkbox in it gets disabled when the corresponding channel is not selected for data acquisition (from either **Settings > Scan**, or **Settings > Time Trace**).
- **OPTIONS** pushbutton: Opens the *Z Scan Options* window, shown in Figure A.13, and has the following controls:

- **Z start** and **Z end** edit boxes: Start and end positions in μm 's. Allowable values are between 0 and 10 μm , with default values being 0 μm for the start-, and 10 μm for the end position. Any value between these can be entered with arbitrary resolution. Start position doesn't have to be less than the end position. This way, the scan can be done in both upwards or downwards direction.

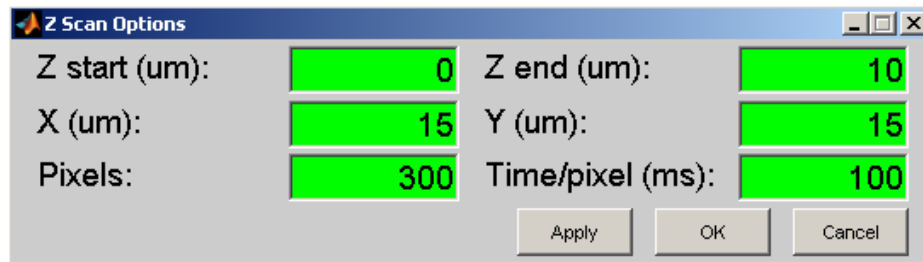


Figure A.13: Z Scan Options window.

- **X** and **Y** edit boxes: X and Y positions in μm 's. Allowable values are between 0 and 30 μm , with default values being 15 μm for both axes. Any value within the allowable range can be entered with arbitrary resolution.
- **Pixels** edit box: Sets the number of pixels in the scan. Allowable values are between 5 and 400, with default 300.
- **Time/pixel** edit box: Sets the integration time in ms's. Allowable values are between 0.1 and 1000 ms, with default 100 ms. Any value within the allowable range can be entered with arbitrary resolution.
- **Apply** pushbutton: Applies the changes.
- **OK** pushbutton: Applies the changes and closes the *Z Scan Options* window.
- **Cancel** pushbutton: Ignores the changes, and closes the *Z Scan Options* window. The "close window" button on the upper right corner is equivalent to **Cancel**.

The Z Scan interface in the data retrieval mode (i.e. when displaying a previously recorded Z Scan data), is very similar to its above-described data acquisition version. The only difference is that the **SCAN**, **ABORT**, and **OPTIONS** pushbuttons are not present in the data retrieval mode.

A.4.2 Area Scan

The Area Scan measurement mode is designed for obtaining intensity images of the sample, at a fixed position along the optical axis. The measurement mode is activated by clicking **Operation > Area Scan**. This brings the Area Scan interface to the *main panel* (Figure A.14), which consists of an axes box and several control buttons:

The controls in the Area Scan interface are explained below:

- **Axis box and color bar:** Shows the intensity map (i.e. image) of the scanned region. A 256-level gray color map is used (cannot be changed). The correspondence between grayscale levels and actual intensities (in counts/pixel) is indicated by the colorbar. By default, the highest- and lowest-intensity pixels among the image are attained white and black colors respectively, while the rest are attained intermediate gray levels according to a simple linear scale.
- **PRESCAN** pushbutton: A shortcut to scan the sample with the following fixed options: Start Point: (0,0) μm ; Size: $30 \times 30 \mu\text{m}^2$; Pixels: 400×400 ; time/pixel: 0.5 ms. Other scan options and settings remain unchanged at their most recent values. The button becomes disabled during scanning; enabled otherwise.

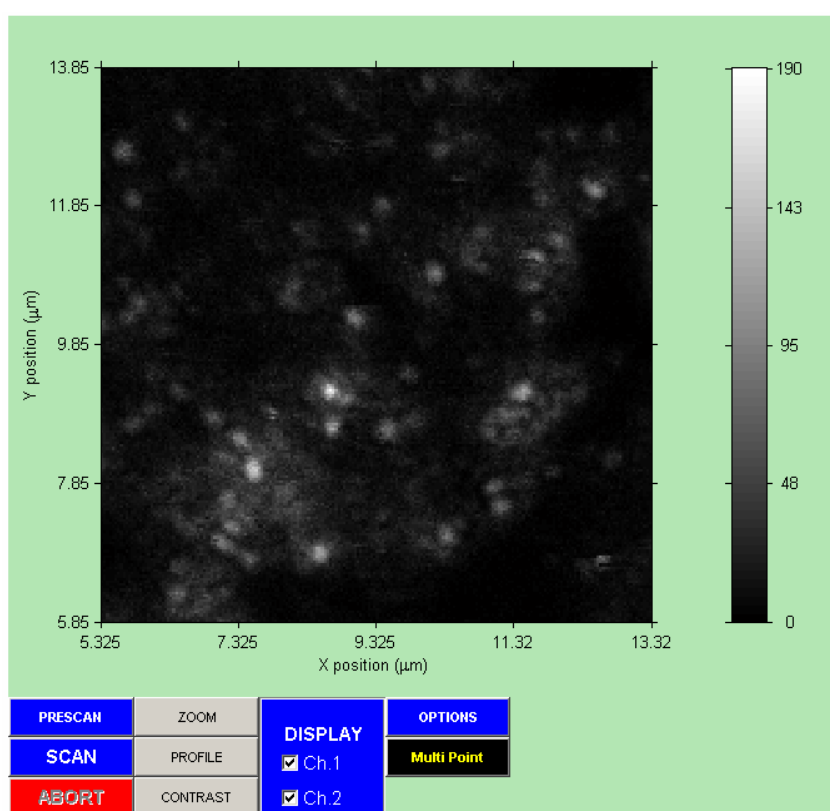


Figure A.14: Area Scan data acquisition interface displayed on the *main panel*.

- **SCAN** pushbutton: Scans the sample with user-defined options (through the *Area Scan Options* window to be introduced below) and settings (as described in Section A.3.1). The button becomes disabled during scanning; enabled otherwise.
- **ABORT** pushbutton: Aborts scanning. The aborted image is still recorded with the pixels beyond aborting given zero intensity. Enabled during scanning; disabled otherwise.
- **ZOOM** pushbutton: Allows zooming into the displayed image.

Upon clicking on **ZOOM**, the mouse cursor switches from arrow to cross. The process continues by left clicking on any corner of the region to be zoomed (Figure A.15; top), dragging the mouse over the region while holding the left button clicked (a rectangle appears during dragging), and then releasing it at the opposite corner (Figure A.15; middle). When the mouse button is released the cursor switches back to arrow, and the selected region covers the axis box (Figure A.15; bottom). Aspect ratio of the axis box may change according to the region. No action is done, if the selected region extends out of the axis box, or if it is smaller than the size of a pixel. If the user clicks **ZOOM**, but then decides not to continue, he can abort by right clicking the mouse. This returns the cursor marker back to arrow again. The zooming procedure described here is not iterative. That is, a zoomed region cannot be zoomed again. Pressing zoom in this case zooms out the -already zoomed- region to the original image.

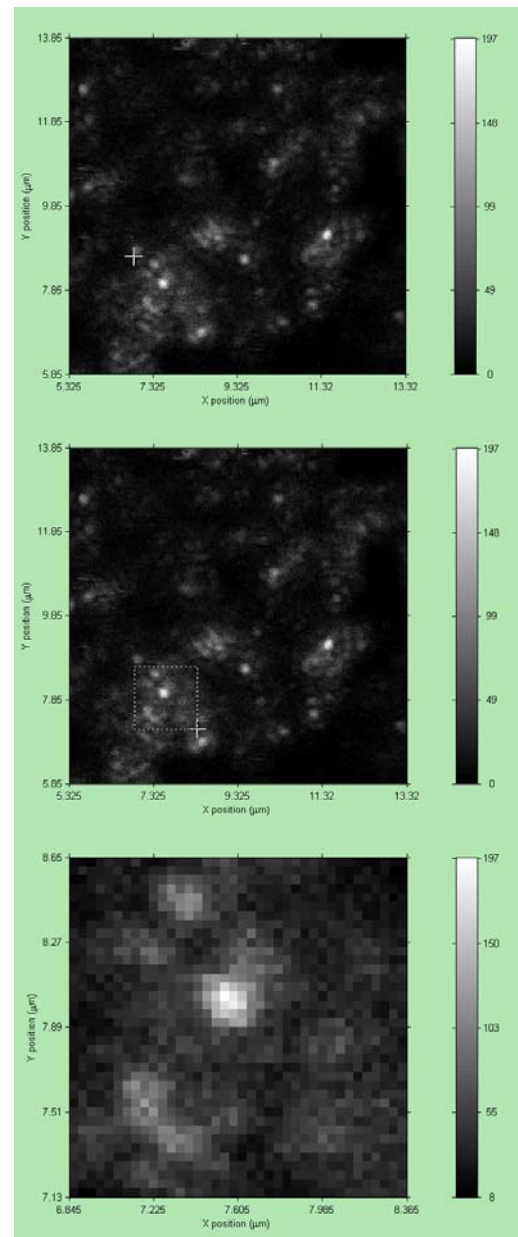


Figure A.15: Steps involved in zooming

- **PROFILE** pushbutton: Plots the intensity versus position data along a line drawn within the image. This can be useful for determining the signal/noise ratio, checking lateral resolution, focus, etc. Profiling can be done over a zoomed image as well. When clicked on **PROFILE**, the mouse cursor switches from arrow to cross. The profile can be started by left clicking and releasing on anywhere in the image (Figure A.16; left). This defines the start point of the profile, and a dotted line appears. The dotted line can then be stretched or

oriented appropriately to bring it onto another position (Figure A.16; right). Right clicking there defines this position as the end point of the profile.

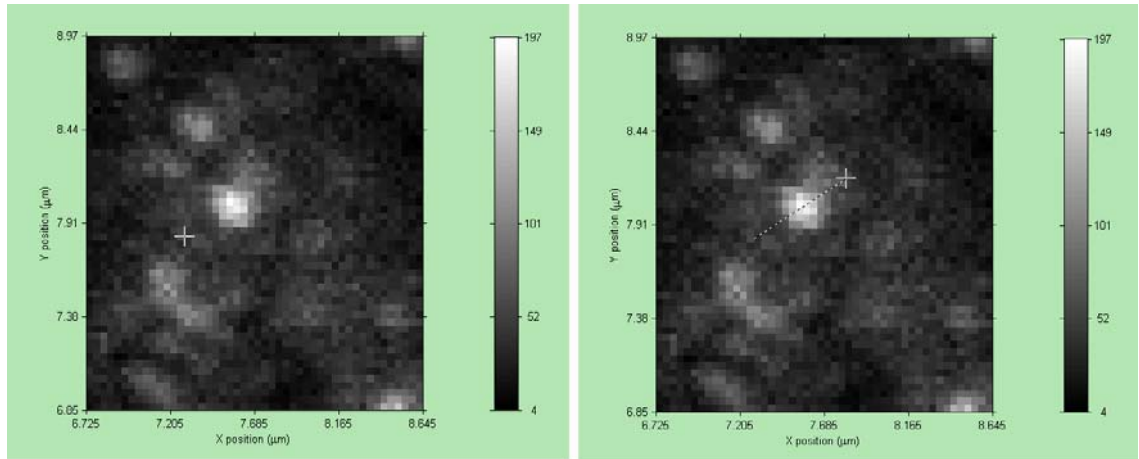


Figure A.16: Steps involved in obtaining profiles.

After right clicking, the cursor switches back to arrow, and the *Profile* window shown in Figure A.17 appears. Besides displaying profiles, the *Profile* window can also be used for fitting 1-D Gaussian function, and exporting the data.

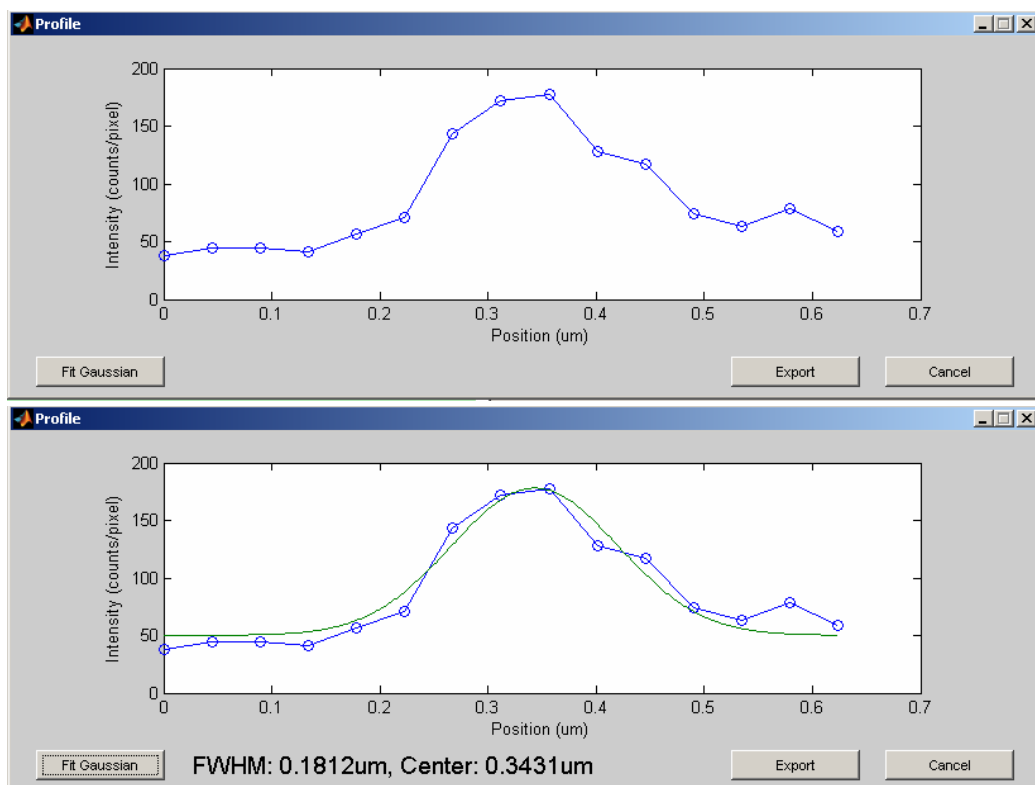


Figure A.17: *Profile* window before (top), and following (bottom) the fit.

- **CONTRAST** pushbutton: Selects area to determine the intensity range corresponding to the color map. Instead of using the whole image's highest- and lowest-intensity pixels (default case), uses the selected area's highest- and lowest-intensity pixels as the coloration range. Some parts of the image outside the chosen area can go beyond the new intensity range, and appear completely black or white.

The procedure is similar to that of zooming. Upon clicking on **CONTRAST**, the mouse cursor switches from arrow to cross. This is followed by left clicking on any corner of the area to be selected (Figure A.18; top), dragging the mouse over the region while holding the left button clicked (a rectangle appears during dragging), and then releasing it at the opposite corner (Figure A.18; middle). When the mouse button is released the cursor switches back to arrow, and color assignment is updated based on the selected region (Figure A.18; bottom). No action is done, if the selected region extends out of the axis box, or if it is smaller than the size of a pixel. If the user clicks **CONTRAST**, but then decides not to continue, he can abort by right clicking the mouse. This returns the cursor marker back to arrow again.

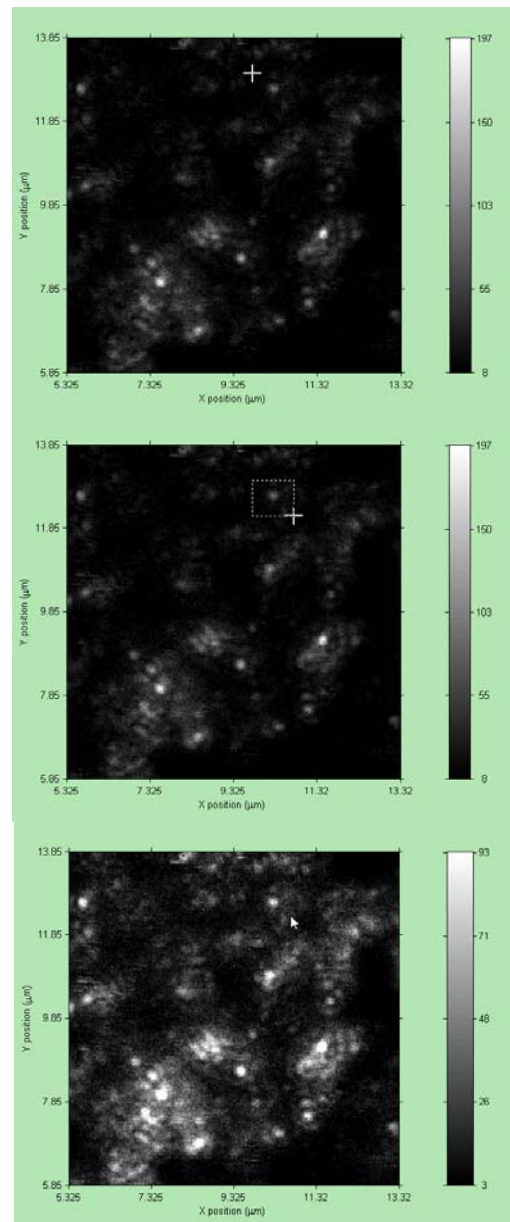


Figure A.18: Steps involved in adjusting contrast.

- **DISPLAY** panel: Contains **Ch.1** and **Ch.2** checkboxes, to control the channel(s) to be displayed on the axis box. While the panel itself is enabled all the time, a checkbox in it gets disabled when the corresponding channel is not selected for data acquisition (from either **Settings > Scan**, or **Settings > Time Trace**).

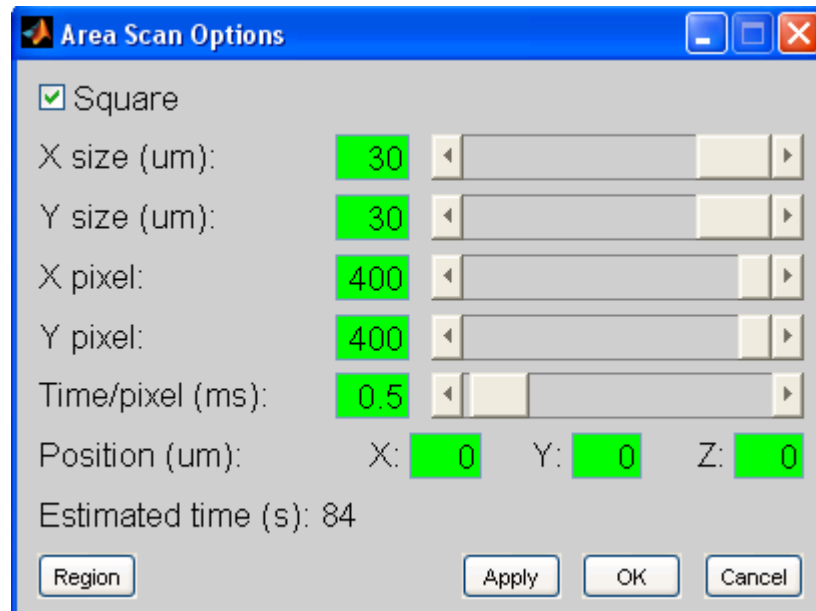


Figure A.19: *Area Scan Options* window.

- **OPTIONS** pushbutton: Opens the *Area Scan Options* window, shown in Figure A.19, and has the following controls:
 - **Square** checkbox: Constrains the **X size** – **Y size**, and **X pixel** – **Y pixel** values to be the same for both axes. Checked by default. If **Square** is unchecked, and then rechecked after some time when the **X size** – **Y size**, and **X pixel** – **Y pixel** values are not equal, the common size and pixel values are set according to following rules: For the pixels, the common pixel value becomes that of the fast axis. For sizes, if there is no limitation from the scanner range, the common value again becomes that of the fast axis. If there is a limitation, the common value is the side of the largest possible square that can fit into the scan range with the current starting positions. In other words, the starting positions are not changed; size is clipped. The constraint imposed by **Square** is handled through sizes, not starting positions.
 - **X size** and **Y size** edit boxes and sliders: **X** and **Y** sizes in μm 's. Allowable values are between 0.1 and 30 μm , with default values being 30 μm for both axes. Certain constraints imposed by **Square** checkbox or by **X** and **Y** edit boxes may apply for the upper limit of the allowable values. The **X size** and **Y size** parameters can be set either from the edit

- boxes with arbitrary resolution, or from the sliders with 10 μm coarse- and 1 μm fine resolutions.
- **X pixel** and **Y pixel** edit boxes and sliders: Set the number of pixels along the x- and y-axis. If **Square** is checked, changing one of **X pixel** or **Y pixel** also changes the other. Allowable values are between 10 and 400, with default 400. The **X pixel** and **Y pixel** parameters can be set either from the edit boxes with 1 pixel resolution, or from the sliders with 50 pixel coarse- and 10 pixel fine resolutions.
 - **Time/pixel** edit box and slider: Sets the integration time in ms's. Allowable values are between 0.1 and 20 ms, with default 0.5 ms. Any value within the allowable range can be entered either from the edit box with 0.1 ms resolution, or from the slider with 5 ms coarse- and 0.5 ms fine resolutions.
 - **Position** edit boxes: The **X** and **Y** edit boxes set the coordinates (in μm 's) of the initial position, which is the lower left corner of the scan area. The lower limit for the allowable values is 0 μm , while the upper limit depends on **X size** and **Y size**, and the range of the scanner ($30 \times 30 \mu\text{m}^2$). The **Z** edit box sets the position of the scan plane along the optical axis. Allowable values are between 0 and 10 μm . For all three edit boxes, default values are 0 μm , and entries can be done with arbitrary resolution.
 - **Estimated time** information: Displays the time it will take for scanning. Depends on **X pixel**, **Y pixel**, **Time/pixel**, and **Wait for slow axis** (in the *Area Scan Settings* window). The **Estimated time** information is updated even if the changes on relevant parameters are not applied. This way, the user may reconsider his entries, based on the time he will need to wait.
 - **Region** pushbutton: Makes it possible to interactively select a smaller scan region within a previous scan. The procedure is very similar to those of **ZOOM** and **CONTRAST** (i.e. left clicking on one corner, dragging while holding the mouse button, releasing at the opposite corner. Right clicking to cancel at an intermediate time). The **X size**, **Y size**, and **Position** parameters are updated according to the selected region, and the **Parent** attribute of the prospective scan is set as the image over which the selection is made. **Square** checkbox gets unchecked automatically when **Region** is used.
 - **Apply** pushbutton: Applies the changes.
 - **OK** pushbutton: Applies the changes and closes the *Area Scan Options* window.
 - **Cancel** pushbutton: Ignores the changes, and closes the *Area Scan Options* window. The "close window" button on the upper right corner is equivalent to **Cancel**.

- **Multi Point** pushbutton: Used for selecting specific positions within a scanned region. Intended for subsequent point measurements at these specific positions. The program has a list, where the coordinates (including z) and parents (i.e. the image name: for example *AreaScan001*) of the selected points are stored. When **Multi Point** is pressed, the *Multi Point* window (Figure A.20) showing the x, and y positions of this list appears, and the mouse pointer switches from arrow to cross. New points can be added to the list by left clicking over the image with the mouse. No action takes place when points outside the axis box are clicked. Right clicking terminates selection. Existing points in the list can be cleared using the **Delete** or **Delete All** buttons. Multi point selection can be done over zoomed images as well. It is a good practice to zoom into the region of interest first, and select afterwards.

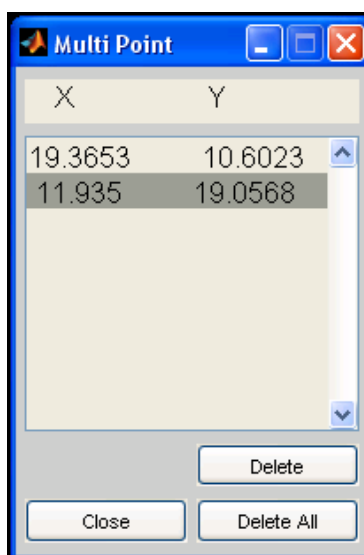


Figure A.20: *Multi Point* window.

The Area Scan interface in the data retrieval mode (i.e. when displaying a previously recorded image), is very similar to its above-described data acquisition version. The only difference is that the **PRESCAN**, **SCAN**, and **ABORT** pushbuttons are not present in the data retrieval mode (Figure A.21). **Options** and **Multi Point** pushbuttons bring out the same windows as in the data acquisition mode.

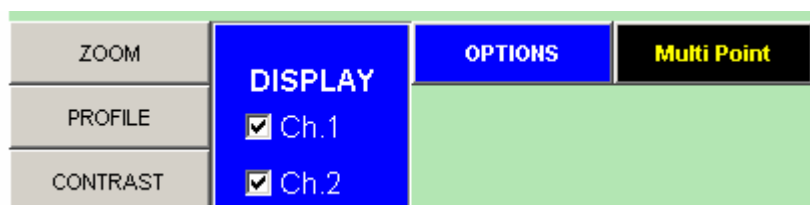


Figure A.21: Controls of the Area Scan interface in the data retrieval mode.

A.4.3 Time Trace

The Time Trace measurement mode is designed for obtaining intensity as a function of time, at fixed positions within the sample. The measurement mode is activated by clicking **Operation > Time Trace**. This brings the Time Trace interface to the *main panel* (Figure A.22), which consists of an axes box and several control buttons:

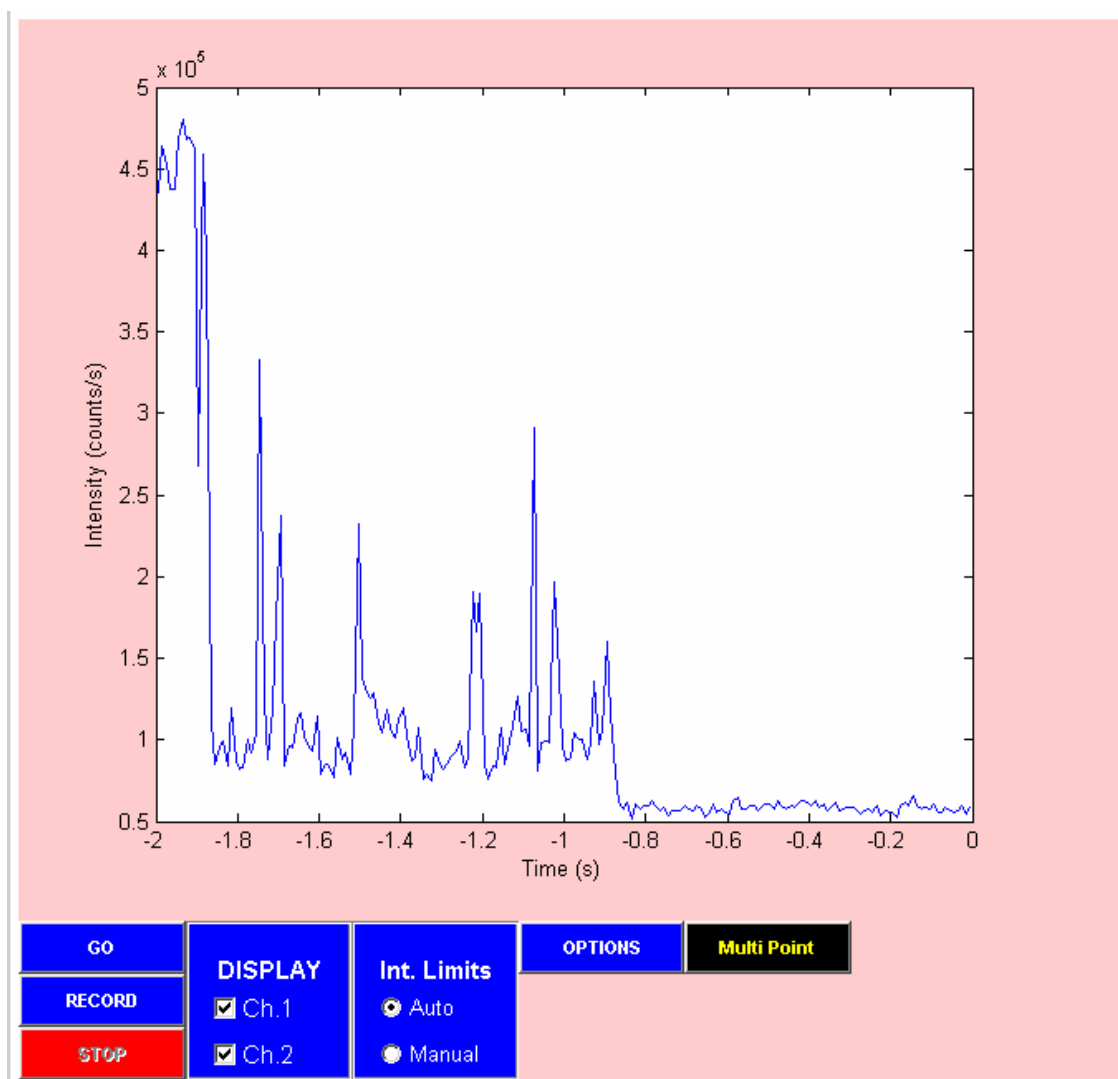


Figure A.22: Time Trace data acquisition interface displayed on the *main panel*.

The controls in the Time Trace interface are explained below:

- **Axis box:** Shows intensity (in counts/s) as a function of time (in s), within a certain time range called window (the window is 2 s in Figure A.22). The negative values in the time axis are to indicate past data.
- **GO pushbutton:** Acquires and displays data without recording. Intended for preparatory tasks like validating sample or parameters, optical alignment etc.

Data is acquired and displayed continuously until the user clicks on **STOP**. Becomes disabled during data acquisition; enabled otherwise.

- **RECORD** pushbutton: Acquires, displays, and records data (i.e. virtually same as **GO**; in addition records data). Recording can be terminated by one of three alternative options set by the **Record for** checkboxes in the *Time Trace Options* window (described below). The button becomes disabled during data acquisition; enabled otherwise.
- **STOP** pushbutton: Stops data acquisition. Enabled during data acquisition; disabled otherwise.
- **DISPLAY** panel: Contains **Ch.1** and **Ch.2** checkboxes, to control the channel(s) to be displayed on the axis box. While the panel itself is enabled all the time, a checkbox in it gets disabled when the corresponding channel is not selected for data acquisition (from either **Settings > Scan**, or **Settings > Time Trace**).
- **Int. Limits** panel: Contains the **Auto** and **Manual** radio buttons, to control the intensity axis limits of the axis box. Default option is **Auto**. When **Auto** is selected, the intensity axis is adjusted automatically based on the incoming data, and channel selections in **DISPLAY**. When **Manual** is selected, the **Upper Limit** and **Lower Limit** edit boxes appear next to the **Int. Limits** panel, to enter the intensity limits in kHz with arbitrary resolution. Default values for the limits are 100 and 0 kHz. Lower limit cannot be greater than the upper one. The **Upper Limit** and **Lower Limit** edit boxes disappear when **Auto** is selected.

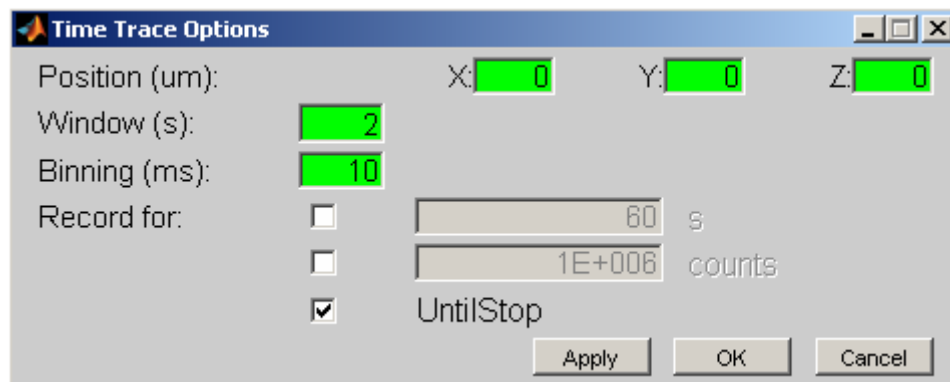


Figure A.23: *Time Trace Options* window.

- **OPTIONS** pushbutton: Opens the *Time Trace Options* window, shown in Figure A.23, and has the following controls:
 - **Position** edit boxes: **X**, **Y**, and **Z** positions in μm 's. Allowable values are between 0 and 30 μm , with default values being 0 μm for all coordinates. Any value within the allowable range can be entered with arbitrary resolution. Note that the values entered here apply to other point measurements as well (i.e. TCSPC and FCS).

- **Window** edit box: sets window time in seconds. Allowable values depend on binning time. Window should be an even integer multiple of binning: $2N \times \text{binning}$, where N can be between 10 and 500 (i.e. there will always be even number of data points in the axes box, and they will be between 20 and 1000). Default value is 2 s. Entries not obeying these restrictions are corrected automatically. Moreover changes in binning time may cause changes in the window time (but not vice versa; i.e. binning time has precedence over window time).
- **Binning** edit box: sets binning time in milliseconds. Should be an integer multiple of resolution. Default value is 10 ms. Entries not obeying this restriction are corrected automatically. Changes in resolution may cause changes in the binning time (but not vice versa; i.e. resolution has precedence over binning time). Similarly, changes in binning time may cause changes in window time. The order of precedence among resolution, binning and window is (from higher to lower): resolution > binning > window.
- **Record for** checkboxes: Determine the data recording mode. In the default **Until Stop** mode, data is continuously recorded until the user clicks **STOP**. In the **finite counts** mode, data recording continues until as many counts as in the finite counts edit box are recorded. The target number of counts applies cumulatively for both channels. Similarly in the **finite time** mode, data recording continues until the target time in the finite time edit box elapses. Values for the target time can be entered with resolution equal to binning time, and minimum allowable value of 0.5 s. For both **finite counts** and **finite time** modes, clicking on **STOP** terminates recording at any time, regardless of the target counts or time set. The **Record for** preferences set here does not affect other point measurement types.
- **Apply** pushbutton: Applies the changes.
- **OK** pushbutton: Applies the changes and closes the *Time Trace Options* window.
- **Cancel** pushbutton: Ignores the changes, and closes the *Time Trace Options* window. The “close window” button on the upper right corner is equivalent to **Cancel**.
- **Multi Point** pushbutton: Puts the **RECORD** button into a “for loop”, for all the positions in the multi point list. The current **Record for** option applies in all of the measurements. The **Multi Point** button gets disabled during acquisition, and displays the number of the point in the multi point list. It is not possible to break the “for loop”, but individual multi point measurements can be terminated one by one (at any time) by clicking on **STOP**.

The Time Trace interface in the data retrieval mode (i.e. when displaying a previously recorded time trace), is slightly different than its above-described data acquisition version. As the first difference, the acquisition-related **GO**, **RECORD**,

STOP, **OPTIONS**, and **Multi Point** pushbuttons are not present in the data retrieval mode (Figure A.24). As the second difference, an additional axis box and a slider are introduced. While the additional axis box on the top provides an overview of the whole trace, the slider (above the control buttons) allows the user to slide the window through the data. A green box within the overview axis marks the window size and position with respect to the whole trace.

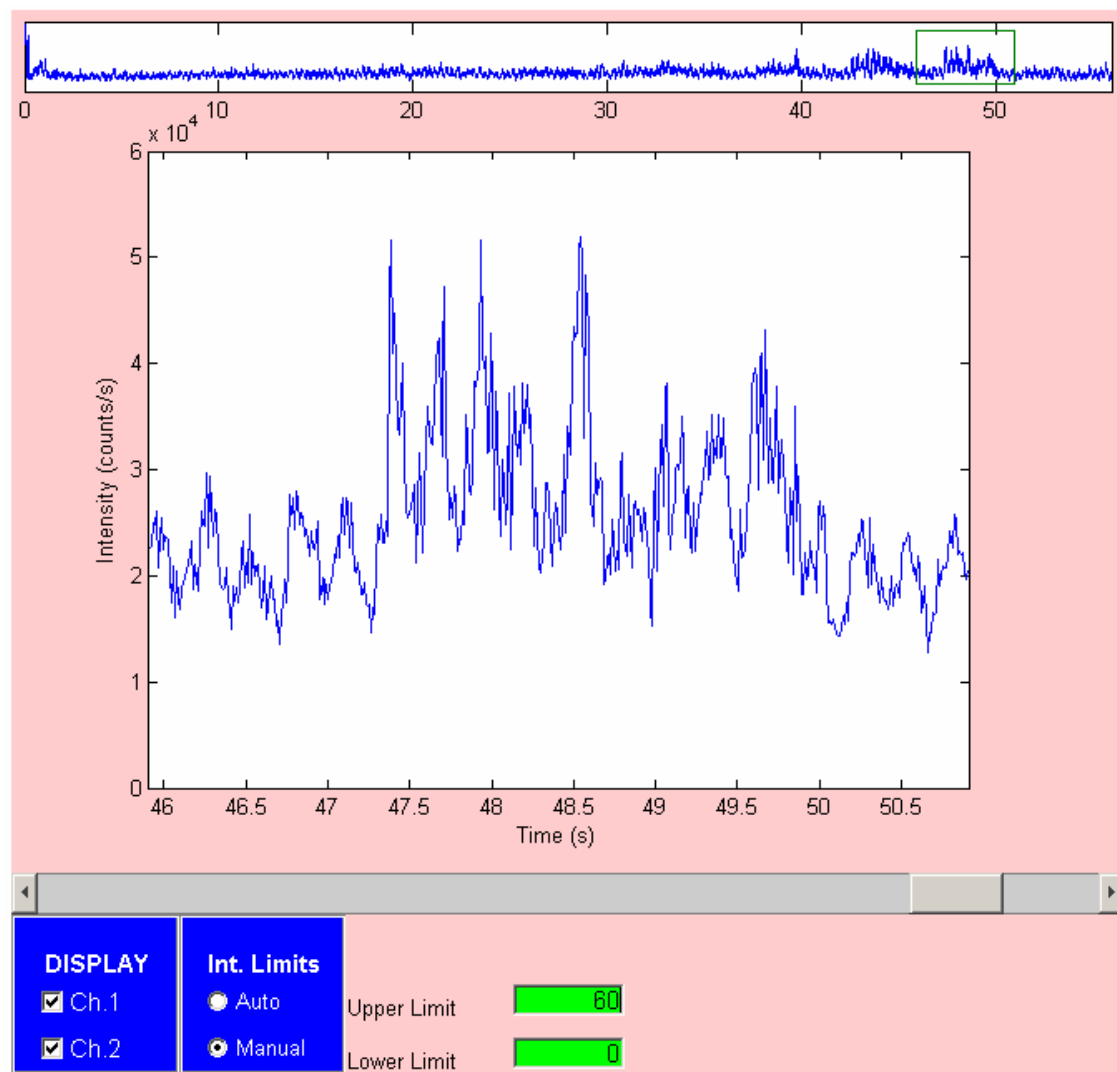


Figure A.24: Time Trace interface in the data retrieval mode, displayed on the *main panel*.

A.4.4 TCSPC

The TCSPC measurement mode is designed for obtaining TCSPC histograms, at fixed positions within the sample. The measurement mode is activated by clicking

Operation > **TCSPC**. This brings the TCSPC interface to the *main panel* (Figure A.25), which consists of an axes box and several control buttons:

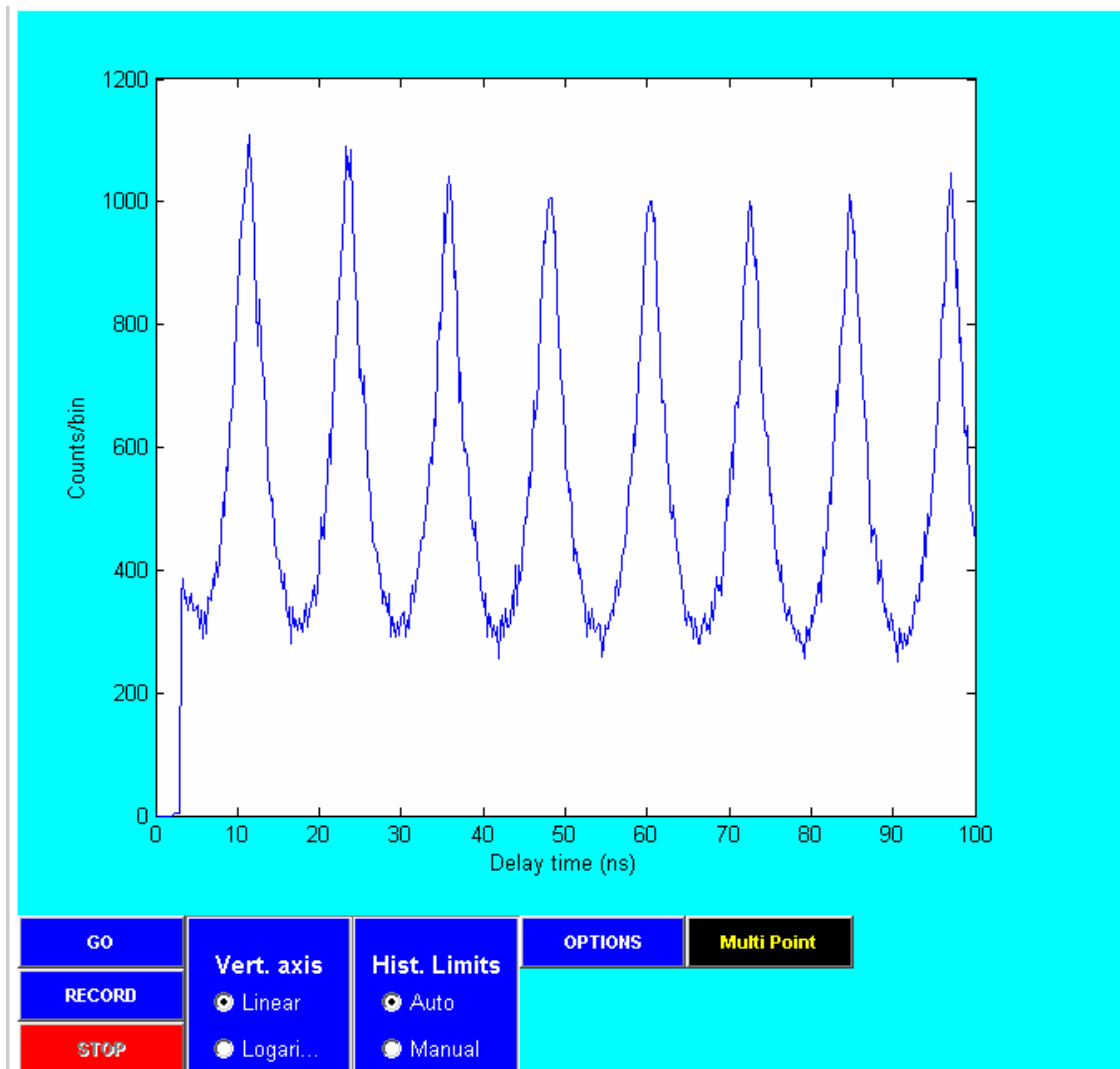


Figure A.25: TCSPC data acquisition interface displayed on the *main panel*.

The controls in the TCSPC interface are explained below:

- **Axis box:** Shows a histogram of coincidence counts as a function of delay time (in ns).
- **GO** pushbutton: Acquires and displays data without recording. Intended for preparatory tasks like validating sample or parameters, adjusting laser intensity etc. Data is acquired and displayed continuously until the user clicks on **STOP**. Becomes disabled during data acquisition; enabled otherwise.

- **RECORD** pushbutton: Acquires, displays, and records data (i.e. virtually same as **GO**; in addition records data). Recording can be terminated by one of three alternative options set by the **Record for** checkboxes in the *TCSPC Options* window (described below). The button becomes disabled during data acquisition; enabled otherwise.
- **STOP** pushbutton: Stops data acquisition. Enabled during data acquisition; disabled otherwise.
- **DISPLAY** panel: Contains **Ch.1** and **Ch.2** checkboxes, to control the channel(s) to be displayed on the axis box. While the panel itself is enabled all the time, a checkbox in it gets disabled when the corresponding channel is not selected for data acquisition (from either **Settings > Scan**, or **Settings > Time Trace**).
- **Vert. axis** panel: Contains the **Linear** and **Logarithmic** radio buttons, to control the counts axis scaling of the histogram. Default option is **Linear**.
- **Hist. Limits** panel: Contains the **Auto** and **Manual** radio buttons, to control the counts axis limits of the histogram. Default option is **Auto**. When **Auto** is selected, the counts axis is adjusted automatically based on the incoming data. When **Manual** is selected, the **Upper Limit** and **Lower Limit** edit boxes appear next to the **Int. Limits** panel, to enter the count limits with arbitrary resolution. Default values for the limits are 500 and 0. Lower limit cannot be greater than the upper one. The **Upper Limit** and **Lower Limit** edit boxes disappear when **Auto** is selected.

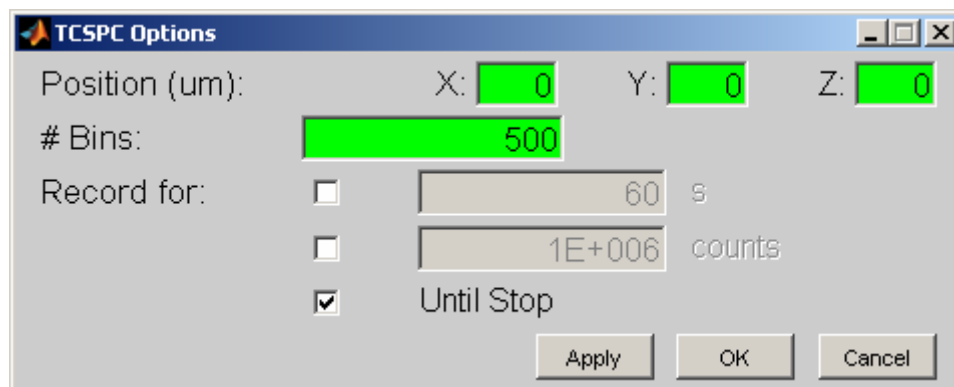


Figure A.26: *TCSPC Options* window.

- **OPTIONS** pushbutton: Opens the *TCSPC Options* window, shown in Figure A.26, and has the following controls:
 - **Position** edit boxes: **X**, **Y**, and **Z** positions in μm 's. Allowable values are between 0 and 30 μm , with default values being 0 μm for all coordinates. Any value within the allowable range can be entered with arbitrary resolution. Note that the values entered here apply to other point measurements as well (i.e. Time Trace and FCS).

- **# Bins** edit box: Sets the number of bins in the histogram. Allowable values are between 20 and 2000, with default 500.
- **Record for** checkboxes: Determine the data recording mode. In the default **Until Stop** mode, data is continuously recorded until the user clicks **STOP**. In the **finite counts** mode, data recording continues until as many counts as in the finite counts edit box are recorded. Similarly in the **finite time** mode, data recording continues until the target time in the finite time edit box elapses. Values for the target time can be entered with 0.5 s resolution. For both **finite counts** and **finite time** modes, clicking on **STOP** terminates recording at any time, regardless of the target counts or time set. The **Record for** preferences set here does not affect other point measurement types.
- **Apply** pushbutton: Applies the changes.
- **OK** pushbutton: Applies the changes and closes the *TCSPC Options* window.
- **Cancel** pushbutton: Ignores the changes, and closes the *TCSPC Options* window. The “close window” button on the upper right corner is equivalent to **Cancel**.
- **Multi Point** pushbutton: Puts the **RECORD** button into a “for loop”, for all the positions in the multi point list. The current **Record for** option applies in all of the measurements. The **Multi Point** button gets disabled during acquisition, and displays the number of the point in the multi point list. It is not possible to break the “for loop”, but individual multi point measurements can be terminated one by one (at any time) by clicking on **STOP**.

The TCSPC interface in the data retrieval mode (i.e. when displaying a previously recorded TCSPC histogram), is very similar to its above-described data acquisition version. Only the **Vert. axis** and **Hist. Limits** panels are present in this case.

A.4.5 FCS

An FCS measurement involves recording a Time Trace, and correlating it. In other words, FCS is the name of an analysis; the raw data file is a Time Trace. The main purpose of the FCS interface is to provide the user a feedback about the FCS curve on the fly, while the Time Trace data is being recorded. If this feedback is not critical, the user may prefer to record the data through the Time Trace interface as well. The real time FCS capability is limited to asynchronous detection mode.

The FCS curve calculated in real time is not stored, because a better (less noisy) curve can always be calculated afterwards from the Time Trace data. If the noisy curve is still needed for some other reasons, it can be exported using **File > Export**, before proceeding with the next measurement.

The FCS measurement mode is activated by clicking **Operation > FCS**. This brings the FCS interface to the *main panel* (Figure A.27), which consists of an axes box and several control buttons:

The controls in the FCS interface are explained below:

- **Axis box:** Shows the correlation function $g^2(\tau)$ as a function of the lag time τ (in s). The τ axis has logarithmic scaling.
- **GO pushbutton:** Acquires and displays data without recording. Intended for preparatory tasks like validating sample or parameters, adjusting laser intensity etc. Data is acquired and displayed continuously until the user clicks on **STOP**. Becomes disabled during data acquisition; enabled otherwise.

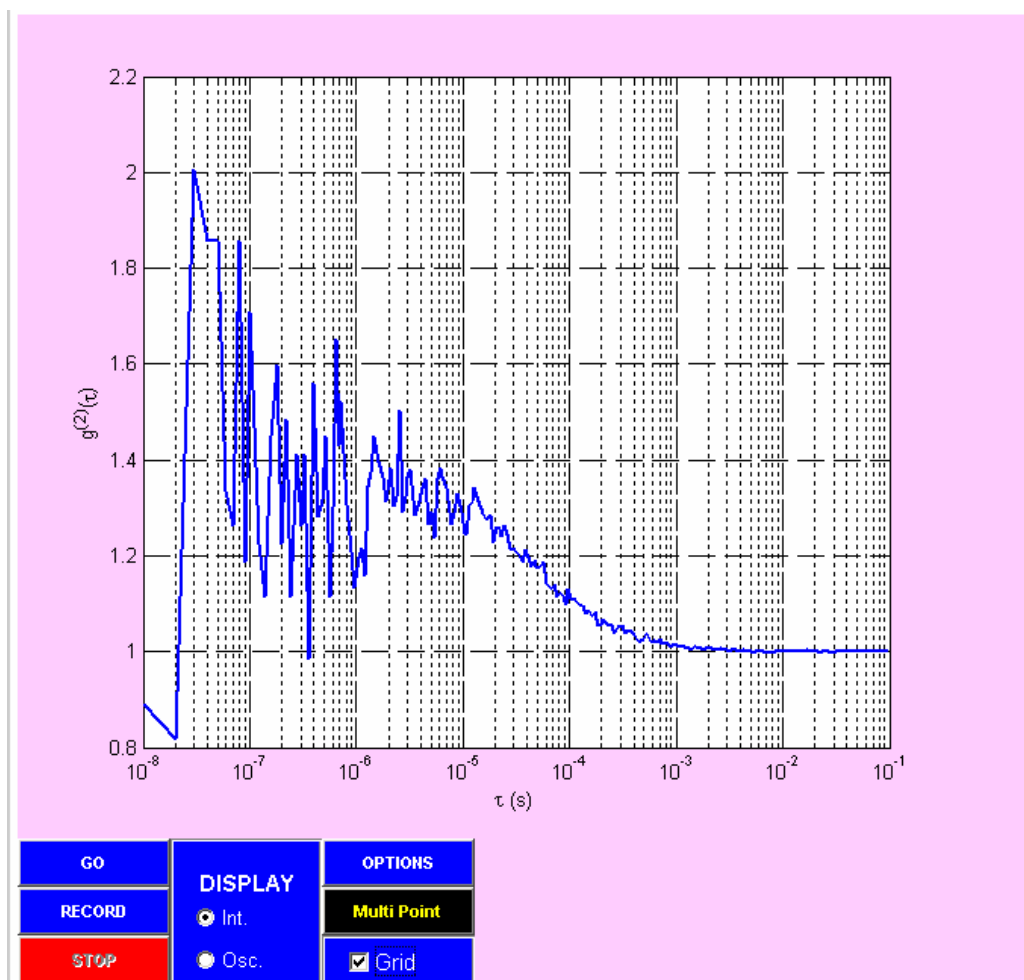


Figure A.27: FCS data acquisition interface displayed on the *main panel*.

- **RECORD pushbutton:** Acquires, displays, and records data (i.e. virtually same as **GO**; in addition records data). Recording can be terminated by one of two alternative options set by the **Record for** checkboxes in the *FCS Options* window (described below). The button becomes disabled during data acquisition; enabled otherwise.
- **STOP pushbutton:** Stops data acquisition. Enabled during data acquisition; disabled otherwise.

- **DISPLAY** panel: Contains **Int.** and **Osc.** radio buttons, to control the display mode. When the default **Int.** option is selected, the correlation curve continues to accumulate in time, and updated at 1 s intervals (fixed). When **Osc.** is selected, the display is again updated in every 1 s, but no accumulation is performed. In other words, correlation curves calculated from 1 s long batches are displayed repeatedly. This usually makes sense only with strong signal levels. The user can switch between **Int.** and **Osc.** modes during acquisition.

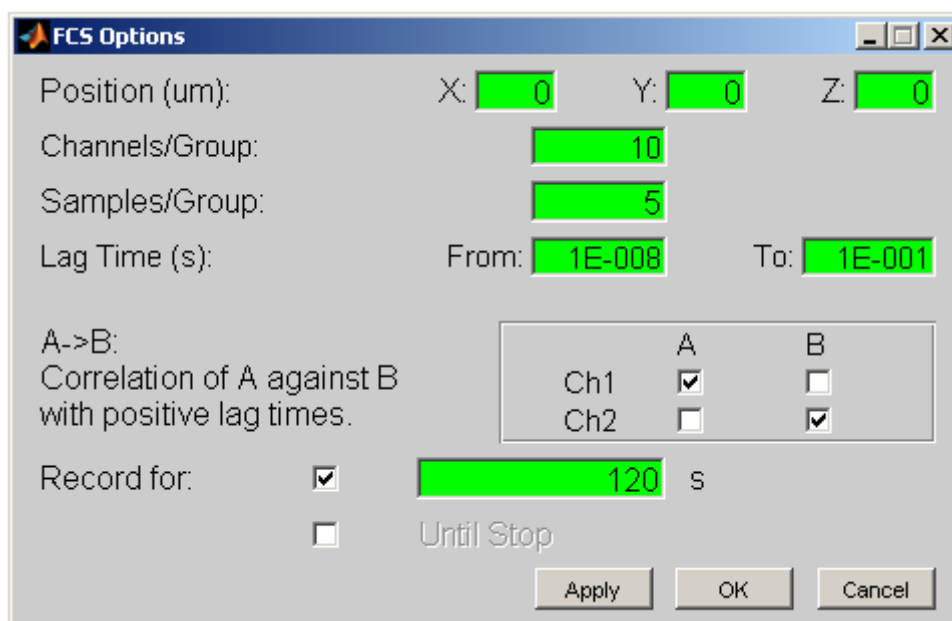


Figure A.28: *FCS Options* window for real-time correlation.

- **OPTIONS** pushbutton: Opens the *FCS Options* window, shown in Figure A.28, and has the following controls:
 - **Position** edit boxes: **X**, **Y**, and **Z** positions in μm 's. Allowable values are between 0 and 30 μm , with default values being 0 μm for all coordinates. Any value within the allowable range can be entered with arbitrary resolution. Note that the values entered here apply to other point measurements as well (i.e. Time Trace and TCSPC).
 - **Channels/Group** edit box: Sets the number of channels per group in the correlation curve. Allowable values are between 1 and 20, with default 10. This parameter controls the balance between “resolution coarsening” of the time trace data, and the lag time⁴. The default value 10 should be suitable for most cases.

⁴ Details are discussed in Opt. Lett. 11 p3583. With the original terminology of this article, the Channels/Group parameter is designated by “B”.

- **Samples/Group** edit box: Sets the number of data points per group in the correlation curve. Allowable values are between 1 and the number of channels set by the **Channels/Group** edit box (default value 5). This parameter enables calculating the correlation curve only for the indicated number of channels per group, without spoiling the resolution-lag time balance. It is intended for saving run time during real-time correlation.
- **Lag Time** edit boxes: Sets the lag time limits in seconds for the real-time correlation. Allowable values are between 10^{-8} and 10^{-1} s. The lower limit should be less than the upper one.
- **A → B** channel selection panel: **A** and **B** are the virtual input channels to be correlated. The **A → B** panel handles the mapping between virtual and real channels. For example by checking **Ch.1** for both **A** and **B**, one obtains an autocorrelation of **Ch.1**. Similarly, by checking **Ch.1** in **A**, and **Ch.2** in **B**, one obtains a cross correlation of **Ch.1** against **Ch.2**. A channel becomes disabled if it is not selected for data acquisition (from either **Settings > Scan**, or **Settings > Time Trace**).
- **Record for** checkboxes: Determine the data recording mode. In the default **finite time** mode, data recording continues until the target time in the finite time edit box elapses. Clicking on **STOP** terminates recording at any time, regardless of the target time. Values for the target time can be entered with a minimum value and resolution of both 0.5 s. In the **Until Stop** mode, data is continuously recorded until the user clicks **STOP**. The **Record for** preferences set here does not affect other point measurement types.
- **Apply** pushbutton: Applies the changes.
- **OK** pushbutton: Applies the changes and closes the *FCS Options* window.
- **Cancel** pushbutton: Ignores the changes, and closes the *FCS Options* window. The “close window” button on the upper right corner is equivalent to **Cancel**.
- **Multi Point** pushbutton: Puts the **RECORD** button into a “for loop”, for all the positions in the multi point list. The current **Record for** option applies in all of the measurements. The **Multi Point** button gets disabled during acquisition, and displays the number of the measurement in the multi point list. It is not possible to break the “for loop”, but individual measurements can be terminated one by one (at any time) by clicking on **STOP**.
- **Grid** checkbox: turns on/off the grid in the axes box.

The FCS interface in the data retrieval mode is much simpler than its above-described data acquisition version. It is merely for displaying FCS curves that are either previously calculated and stored, or being calculated currently⁵. The only control

⁵ Calculating FCS curves from Time Trace data will be explained in the next section.

buttons are **Abort**, to abort the calculation of an FCS curve, and **Grid**, to turn on/off the grid on the displayed curve.

A.5 Analysis

The analyses within the Confocal Setup Software are currently limited to FCS measurements. These can be activated by clicking on the **Correlation** and **FCS Fitting** items under the **Analysis** menu.

A.5.1 Correlation

This analysis calculates the correlation function from recorded Time Traces (both asynchronous and synchronous acquisition modes). For this, the Time Trace to be correlated should be displayed on the main panel (i.e. the Time Trace should be selected from the list in the *explorer panel*, and the **Display** button should appear red). Once the Time Trace is displayed, clicking on **Analysis > Correlation**, brings the *FCS Options* window shown in Figure A.29.

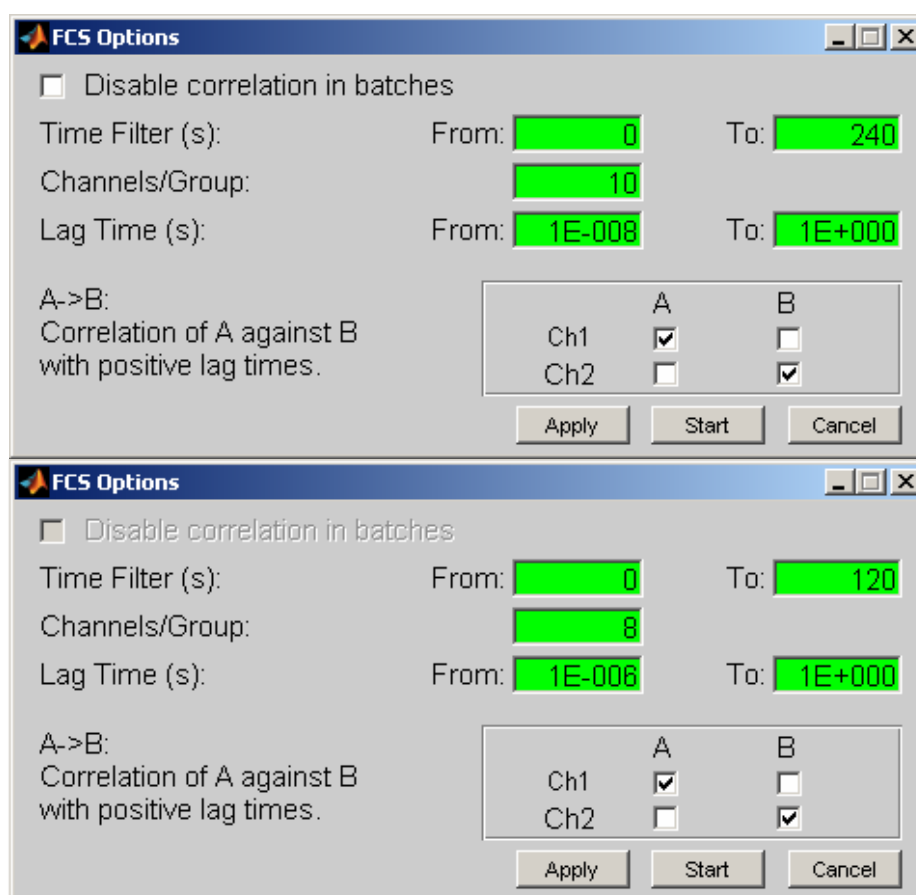


Figure A.29: *FCS Options* window for correlating Time Traces recorded with **Async** (top) or **Sync** (bottom) acquisition modes.

While this window is similar to the one brought by the **OPTIONS** button of the FCS measurement interface (Figure A.28), there are some differences as well. The elements of the window are explained below:

- **Disable correlation in batches** checkbox: Applicable only to asynchronous Time Traces. For an asynchronous Time Trace, there are three alternative correlation methods:
 - **Method-1:** For cases with less than 4×10^6 photon detection events per channel, the program transfers all the data to the memory in one step, and calculates the correlation function relatively quickly.
 - **Method-2:** For cases when there are more than 4×10^6 photon detection events per channel, the program divides the data into as few as possible batches of equal length (in time; not in photon numbers), and processes each batch as in **Method-1**. The final correlation curve is given by the average of the curves from batches.
 - **Method-3:** As a third alternative, the program can transfer the data and correlate together. This is slower than having the data in memory, but may be the only applicable method depending on certain conditions, especially the maximum lag time parameter.

The precedence among these methods is as follows: **Method-1** is applied whenever possible (other methods cannot be used in this case). When this is not possible, the applicability of **Method-2** is checked. If it is applicable, and if the **Disable correlation in batches** checkbox is unchecked, then **Method-2** is applied. If **Method-2** is not applicable, or if it is applicable but the **Disable correlation in batches** checkbox is checked, then **Method-3** is applied. In other words, the **Disable correlation in batches** checkbox gives the user the freedom to choose between **Method-2** and **Method-3**, when both are possible. It is by default unchecked (i.e. **Method-2** is applied when both **Method-2** and **Method-3** are possible), however if the user for some reason wants to have the data correlated in one piece, he can check this checkbox and compel the program to use **Method-3** (at the expense of longer calculation time).

- **Time Filter** edit boxes: Enables the user to limit the calculation of the correlation function to the segment between **From** and **To** edit boxes. Default values are assigned to cover the whole trace. This feature can be useful in excluding some unwanted parts from the analysis (for example a burst in an FCS measurement, or after bleaching in a single molecule trace).
- **Channels/Group** edit box: Essentially same as the one in the real-time *FCS Options* window (Figure A.28). Sets the number of channels per group in the correlation curve, and thereby controls the balance between “resolution coarsening” of the time trace data, and the lag time. Default values are 10 for asynchronous time traces, and 8 for synchronous ones. Minimum allowable value is 1, with no restriction on the maximum value. The default values should be appropriate for most cases.

- **Lag Time** edit boxes: Sets the lag time limits in seconds. Allowable values are between resolution and the length of the trace set by **Time Filter** edit boxes.
- **A → B** channel selection panel: Same as the one in the real-time *FCS Options* window (Figure A.28). Handles the mapping between virtual and real channels.
- **Apply** pushbutton: Applies the changes.
- **Start** pushbutton: Applies the changes, closes the *FCS Options* window, and starts correlation. Upon pressing start, the main panel switches from Time Trace retrieval interface to FCS retrieval interface, where the correlation progress can be followed, and aborted at any time using the **ABORT** button. Following completion or abort, the resulting FCS curve is recorded with name FCSXXX (for example FCS001), and immediately retrieved from the session. This is the only measurement/analysis that leaves the **Display** button (in the *explorer panel*) selected.
- **Cancel** pushbutton: Ignores the changes, and closes the *FCS Options* window. The “close window” button on the upper right corner is equivalent to **Cancel**.

A.5.2 FCS Fitting

This analysis is for fitting correlation curves calculated as described in the previous section. For this, the FCS to be fitted should be displayed on the main panel (i.e. the FCS should be selected from the list in the *explorer panel*, and the **Display** button should appear red). Once the FCS is displayed, clicking on **Analysis > FCS Fitting** does two things: i) transfers the FCS curve from FCS retrieval interface to FCS FIT interface and displays it on the *main panel* as shown in Figure A.30, and ii) brings up the *FCS Options* window shown in Figure A.31.

The elements in the *FCS Fitting* window are explained below:

- **Model** pull-down list: Allows for selection of the fitting model. Currently there are two models: **Diffusion with Triplet** and **Pure Diffusion**. **Diffusion with Triplet** is the default model.
- **Show** pushbutton: Shows the selected model equation in a separate window.
- **Number of Components** panel: Configures the number of components in the model (i.e. the maximum value of the summation index n in the equations). When **Auto** is checked, the program gradually increases the number of components as long as the corresponding diffusion times ($\tau_{D,i}$'s) in the resulting fit have non-overlapping confidence intervals. The procedure is stopped when any two diffusion times have overlapping confidence intervals, or when the maximum number of components set by the user in the **Max n** edit box is reached. The default value for **Max n** is 5, with minimum 2, and no upper limit. When **Fixed** is checked, the number of components is set by the user through

the **n** edit box. The default value for **n** is 1, with minimum again 1, and no upper limit⁶.

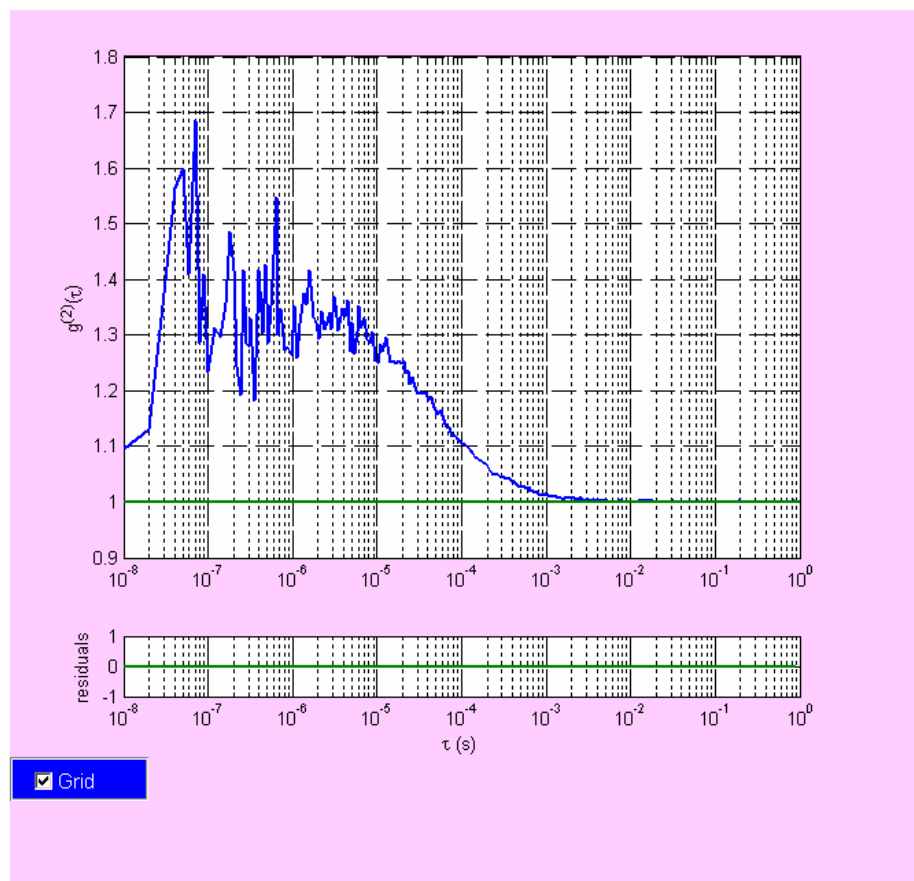


Figure A.30: FCS FIT interface with the curve to be fitted, displayed on the *main panel*.

- **Tau Interval** edit boxes: Sets the lag time range in seconds, to be used in fitting. Data corresponding to lag times shorter than **From** or longer than **To** are not considered in the fit. Allowable values are limited by the minimum and maximum lag times in the correlation curve. Default values cover the whole data. This feature can be useful for example in preventing a noisy end from spoiling the fit.
- **Parameter list**: Lists the parameters in the configured model, along with their lower (**Min**) and upper (**Max**) bounds, and start values (**Start**). Upon fitting, the fit values (**Fit**) and 95 % confidence intervals (**95% Conf. Int.**) also appear in the neighboring columns. The **Start** values are editable within their

⁶ In fact there is an upper limit for the number of components set by the number of data points in the FCS curve, but this is not considered in the **Max n** or **n** edit boxes. The program yet displays a reminder if that limit is reached during fitting.

corresponding **Min-Max** values, and the **Min**, **Max** values are also editable within their physically meaningful ranges. As an example to physically meaningful range, the minimum value for a diffusion time can never be less than 0. Therefore it is not possible to set **Min** for **tauD1** to a negative value. On the other hand, if the user is confident that the **tauD1** for his sample is greater than for example $10\ \mu\text{s}$, he can set the corresponding **Min** cell to $10\ \mu\text{s}$, and help the fit program by squeezing the range to search the best-fit value.

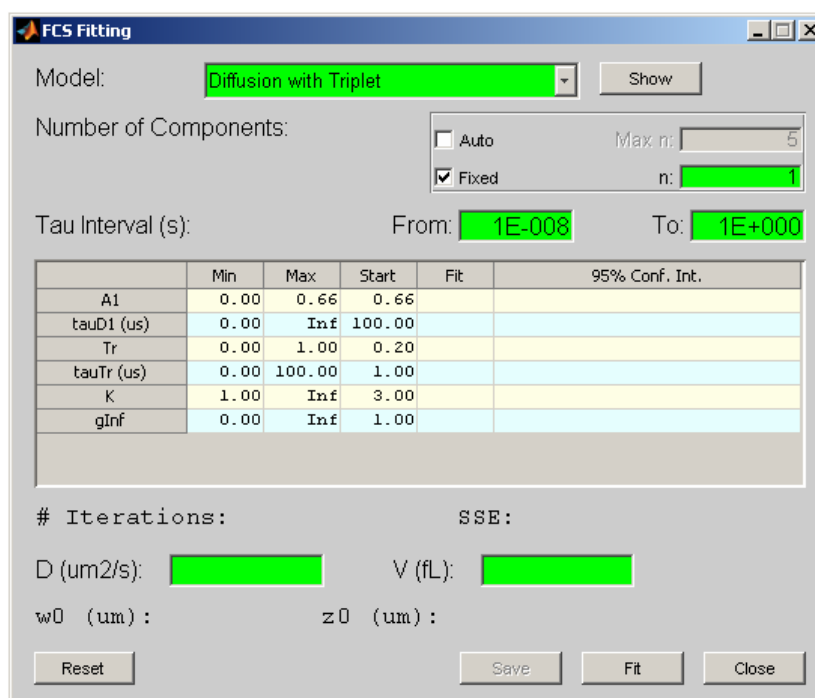


Figure A.31: FCS Fitting window.

- **# Iterations** and **SSE** information: Following a fit, the number of iterations and sum of squared errors are displayed here, to provide the user a feedback in comparing performances of fits with different preferences.
- **D** edit box: Following a fit with 1-component model, if the diffusion coefficient **D** of the species is known, this value can be entered here in $\mu\text{m}^2/\text{s}$, to get the volume **V** (in fL's), diameter **w0** (in μm 's), and length **z0** (in μm 's) of the corresponding detection ellipsoid.
- **V** edit box: Following a fit with 1-component model, if the volume of the detection ellipsoid is known, this value can be entered here in fL, to get the diameter **w0** (in μm 's), and length **z0** (in μm 's) of the detection ellipsoid, and the diffusion coefficient **D** (in $\mu\text{m}^2/\text{s}$) of the species.
- **w0** and **z0** information: Following a fit with 1-component model, when either of the **D** or **V** edit boxes is entered, the calculated diameter **w0** (in μm 's), and length **z0** (in μm 's) of the detection ellipsoid are displayed here.

- **Reset** pushbutton: Resets all the elements in the *FCS Fitting* window to their default configuration.
- **Save** pushbutton: Saves the fit with name FCSFIT (for example FCSFIT001), and closes the *FCS Fitting* window. Saved fit is displayed on the *main panel*. **Save** pushbutton becomes active following the first fit to the data.
- **Fit** pushbutton: Fits the FCS curve with selected configuration, and displays the fit and the residuals on the *main panel*. *FCS Fitting* window remains open for further trials.
- **Close** pushbutton: Closes the *FCS Fitting* window without saving, and switches the main panel from FCS FIT interface back to FCS retrieval interface. The “close window” button on the upper right corner of the *FCS Fitting* window is equivalent to this pushbutton.

The *FCS Fitting* window is shown in Figure A.32, after fitting a 1-component model to the data, and entering $280 \mu\text{m}^2/\text{s}$ to the **D** edit box.

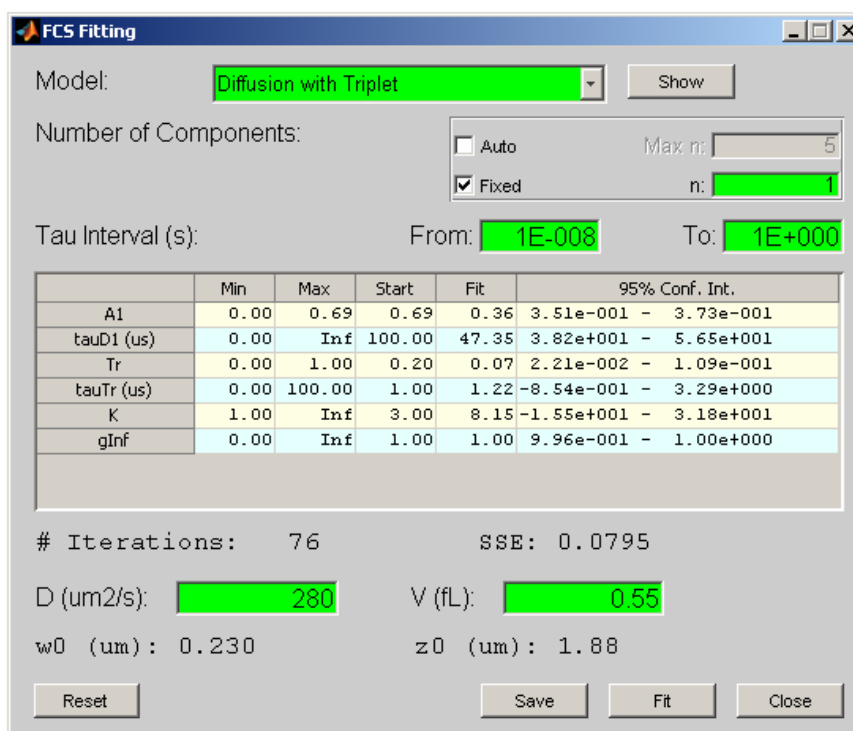


Figure A.32: The *FCS Fitting* window after fitting the data, and entering $280 \mu\text{m}^2/\text{s}$ to the **D** edit box.

Appendix B

DERIVATIVES OF THE LOG-LIKELIHOOD FUNCTION

B.1 First Order Derivatives

The general expression for the first order partial derivatives of the log-likelihood function, with respect to the components of Θ was given in eq. (4.9).

For x_0 component, this derivative becomes:

$$\frac{\partial L(\Theta)}{\partial x_0} = \sum_{k=1}^N \left(\frac{m_k}{\Lambda_k(\Theta)} - 1 \right) \lambda_0 \int_0^T \frac{\partial p_k(\tau)}{\partial x_0} d\tau, \quad (\text{B.1})$$

where

$$\begin{aligned} p_k(\tau) &= \int_{y_{k1}}^{y_{k2}} \int_{x_{k1}}^{x_{k2}} g(x - x_0 - v_x \tau, y - y_0 - v_y \tau) dx dy \\ &= \int_{y_{k1} - y_0 - v_y \tau}^{y_{k2} - y_0 - v_y \tau} \int_{x_{k1} - x_0 - v_x \tau}^{x_{k2} - x_0 - v_x \tau} g(x, y) dx dy. \end{aligned} \quad (\text{B.2})$$

Then the partial derivative of $p_k(\tau)$ with respect to x_0 can be written as

$$\begin{aligned} \frac{\partial p_k(\tau)}{\partial x_0} &= \int_{y_{k1} - y_0 - v_y \tau}^{y_{k2} - y_0 - v_y \tau} \frac{\partial}{\partial x_0} \left(\int_{x_{k1} - x_0 - v_x \tau}^{x_{k2} - x_0 - v_x \tau} g(x, y) dx \right) dy \\ &= \int_{y_{k1} - y_0 - v_y \tau}^{y_{k2} - y_0 - v_y \tau} [g(x_{k1} - x_0 - v_x \tau, y) - g(x_{k2} - x_0 - v_x \tau, y)] dy. \end{aligned} \quad (\text{B.3})$$

If the point spread function is Gaussian with parameter σ , i.e.,

$$g(x, y) = \frac{1}{2\pi\sigma^2} e^{-\frac{x^2 + y^2}{2\sigma^2}} = \frac{1}{\sigma^2} G\left(\frac{x}{\sigma}\right) G\left(\frac{y}{\sigma}\right), \quad (\text{B.4})$$

where $G(a) = \frac{1}{\sqrt{2\pi}} e^{-\frac{a^2}{2}}$, the probability $p_k(\tau)$ can be written as

$$p_k(\tau) = Q_{kx}(\tau)Q_{ky}(\tau), \quad (\text{B.5})$$

where

$$\begin{aligned} Q_{kx}(\tau) &= \int_{\frac{x_{k1}-x_0-v_x\tau}{\sqrt{2\sigma}}}^{\frac{x_{k2}-x_0-v_x\tau}{\sqrt{2\sigma}}} \frac{e^{-x^2}}{\sqrt{\pi}} dx \\ &= \frac{1}{2} \left[\operatorname{erf}\left(\frac{x_{k2}-x_0-v_x\tau}{\sqrt{2\sigma}}\right) - \operatorname{erf}\left(\frac{x_{k1}-x_0-v_x\tau}{\sqrt{2\sigma}}\right) \right] \end{aligned} \quad (\text{B.6})$$

as

$$\operatorname{erf}(a) = \frac{2}{\sqrt{\pi}} \int_0^a e^{-t^2} dt.$$

Similarly

$$Q_{ky}(\tau) = \frac{1}{2} \left[\operatorname{erf}\left(\frac{y_{k2}-y_0-v_y\tau}{\sqrt{2\sigma}}\right) - \operatorname{erf}\left(\frac{y_{k1}-y_0-v_y\tau}{\sqrt{2\sigma}}\right) \right]. \quad (\text{B.7})$$

Thus

$$\frac{\partial p_k(\tau)}{\partial x_0} = \frac{\partial Q_{kx}(\tau)}{\partial x_0} Q_{ky}, \quad (\text{B.8})$$

where

$$\begin{aligned} \frac{\partial Q_{kx}(\tau)}{\partial x_0} &= \frac{1}{\sqrt{2\pi}\sigma} \left(e^{-\frac{(x_{k1}-x_0-v_x\tau)^2}{2\sigma^2}} - e^{-\frac{(x_{k2}-x_0-v_x\tau)^2}{2\sigma^2}} \right) \\ &= -\frac{1}{\sqrt{2\pi}\sigma} e^{-\frac{(x_{k1}-x_0-v_x\tau)^2}{2\sigma^2}} \left(e^{\frac{2\Delta_x(x_0+v_x\tau-x_{k1})-\Delta_x^2}{2\sigma^2}} - 1 \right). \end{aligned} \quad (\text{B.9})$$

For y_0 component, the derivations are the same as above with the obvious replacement of x with y , and y with x .

For v_x component, eq. (4.9) becomes:

$$\frac{\partial L(\Theta)}{\partial v_x} = \sum_{k=1}^N \left(\frac{m_k}{\Lambda_k(\Theta)} - 1 \right) \lambda_0 \int_0^T \frac{\partial p_k(\tau)}{\partial v_x} d\tau, \quad (\text{B.10})$$

where

$$\frac{\partial p_k(\tau)}{\partial v_x} = \tau \int_{y_{k_1} - y_0 - v_y \tau}^{y_{k_2} - y_0 - v_y \tau} [g(x_{k_1} - x_0 - v_x \tau, y) - g(x_{k_2} - x_0 - v_x \tau, y)] dy. \quad (\text{B.11})$$

Note that

$$\frac{\partial p_k(\tau)}{\partial v_x} = \tau \frac{\partial p_k(\tau)}{\partial x_0}. \quad (\text{B.12})$$

For v_y component, the derivations are the same as v_x with the obvious replacement of x with y , and y with x .

For λ_0 and λ_{bg} components, eq. (4.9) becomes:

$$\frac{\partial L(\Theta)}{\partial \lambda_0} = \sum_{k=1}^N \left(\frac{m_k}{\Lambda_k(\Theta)} - 1 \right) \int_0^T p_k(\tau) d\tau, \quad (\text{B.13})$$

and

$$\frac{\partial L(\Theta)}{\partial \lambda_{bg}} = \sum_{k=1}^N \left(\frac{m_k}{\Lambda_k(\Theta)} - 1 \right) T = T \sum_{k=1}^N \frac{m_k}{\Lambda_k(\Theta)} - TN. \quad (\text{B.14})$$

B.2 Second Order Derivatives

The general expression for the second order partial derivatives of the log-likelihood function, with respect to the components of Θ was given in eq. (4.10). The algorithm will be using only the diagonal terms of the Hessian matrix. So only the $\Theta_i = \Theta_j$ case will be considered here.

For x_0 component, the second order partial derivative of $L(\Theta)$ becomes:

$$\frac{\partial^2 L(\Theta)}{\partial x_0^2} = \sum_{k=1}^N \left[-\frac{m_k}{\Lambda_k^2(\Theta)} \left(\frac{\partial \Lambda_k(\Theta)}{\partial x_0} \right)^2 + \left(\frac{m_k}{\Lambda_k(\Theta)} - 1 \right) \frac{\partial^2 \Lambda_k(\Theta)}{\partial x_0^2} \right], \quad (\text{B.15})$$

where

$$\frac{\partial^2 \Lambda_k(\Theta)}{\partial x_0^2} = \lambda_0 \int_0^T \frac{\partial^2 p_k(\tau)}{\partial x_0^2} d\tau. \quad (\text{B.16})$$

If the point spread function is Gaussian with parameter σ , one can write

$$\frac{\partial^2 p_k(\tau)}{\partial x_0^2} = \frac{1}{\sqrt{2\pi}\sigma^3} \left[(x_{k_1} - x_0 - v_x \tau) e^{-\frac{(x_{k_1} - x_0 - v_x \tau)^2}{2\sigma^2}} - (x_{k_2} - x_0 - v_x \tau) e^{-\frac{(x_{k_2} - x_0 - v_x \tau)^2}{2\sigma^2}} \right] Q_{ky}(\tau). \quad (\text{B.17})$$

The second order partial derivative with respect to y_0 is the same as eq. (B.16) except for the obvious replacement of x with y , and y with x .

For v_x component, the second order partial derivative of $L(\Theta)$ becomes:

$$\frac{\partial^2 L(\Theta)}{\partial v_x^2} = \sum_{k=1}^N \left[-\frac{m_k}{\Lambda_k^2(\Theta)} \left(\frac{\partial \Lambda_k(\Theta)}{\partial v_x} \right)^2 + \left(\frac{m_k}{\Lambda_k(\Theta)} - 1 \right) \frac{\partial^2 \Lambda_k(\Theta)}{\partial v_x^2} \right], \quad (\text{B.18})$$

where

$$\frac{\partial^2 \Lambda_k(\Theta)}{\partial v_x^2} = \lambda_0 \int_0^T \frac{\partial^2 p_k(\tau)}{\partial v_x^2} d\tau. \quad (\text{B.19})$$

If the point spread function is Gaussian with parameter σ , one can write

$$\frac{\partial^2 p_k(\tau)}{\partial v_x^2} = \tau^2 \frac{\partial^2 p_k(\tau)}{\partial x_0^2}. \quad (\text{B.20})$$

The second order partial derivative with respect to v_y is the same as that of v_x except for the obvious replacement of x with y , and y with x .

The second order partial derivatives with respect to λ_0 and λ_{bg} components are:

$$\frac{\partial^2 L(\Theta)}{\partial \lambda_0^2} = -\sum_{k=1}^N \frac{m_k}{\Lambda_k^2(\Theta)} \left(\int_0^T p_k(\tau) d\tau \right)^2, \quad (\text{B.21})$$

and

$$\frac{\partial^2 L(\Theta)}{\partial \lambda_{bg}^2} = -T^2 \sum_{k=1}^N \frac{m_k}{\Lambda_k^2(\Theta)}. \quad (\text{B.22})$$

respectively.

BIBLIOGRAPHY

1. B. C. Stipe, M. A. Rezaei, and W. Ho, *Science* **279**, 1907 (1998).
2. S.-W. Hla, L. Bartels, G. Meyer, and K.-H. Rieder, *Phys. Rev. Lett.* **85**, 2777 (2000).
3. L. Grill, M. Alemani, K.-H. Rieder, F. Moresco, G. Rapenne, C. Joachim, M. V. Peters, and S. Hecht, *J. Scann. Probe Microsc.* **2**, 19 (2007).
4. Y. Roiter, and S. Minko, *J. Am. Chem. Soc.* **127**, 15688 (2005).
5. L. Gross, F. Mohn, N. Moll, P. Liljeroth, and G. Meyer, *Science* **325**, 1110 (2009).
6. E. Betzig, and R. J. Chichester, *Science* **262**, 1422 (1993).
7. X. S. Xie, *Acc. Chem. Res.* **29**, 598 (1996).
8. N. F. van Hulst, J.-A. Veerman, M. F. Garcia-Parajo, and L. Kuipers, *J. Chem. Phys.* **112**, 7799 (2000).
9. K. Kneipp, Y. Wang, H. Kneipp, L. T. Perelman, I. Itzkan, R. R. Dasari, and M. S. Feld, *Phys. Rev. Lett.* **78**, 1667 (1997).
10. E. C. Le Ru, and P. G. Etchegoin, *Annu. Rev. Phys. Chem.* **63**, 65 (2012).
11. D. A. Skoog, F. J. Holler, and S. R. Crouch, *Principles of Instrumental Analysis*, chapter 15, Thomson Brooks/Cole, 2007, Molecular Luminescence Spectrometry.
12. W. P. Ambrose, Th. Basché, and W.E. Moerner, *J. Chem. Phys.* **95**, 7150 (1991).
13. S. Kummer, S. Mais, and Th. Basché, *J. Phys. Chem.* **99**, 17078 (1995).
14. S. Kummer, F. Kulzer, R. Kettner, Th. Basché, C. Tietz, C. Glowatz, and C. Kryschi, *J. Chem. Phys.* **107**, 7673 (1997).
15. Th. Basché, W.E. Moerner, M. Orrit, and H. Talon, *Phys. Rev. Lett.* **69**, 1516 (1992).
16. B. Kozankiewicz, J. Bernard, and M. Orrit, *J. Chem. Phys.* **101**, 9377 (1994).
17. A. Walser, A. Renn, S. Götzinger, and V. Sandoghdar, *Chem. Phys. Lett.* **472**, 44 (2009).

18. S. Kummer, Th. Basché, and C. Bräuchle, *Chem. Phys. Lett.* **229**, 309 (1994).
19. A. A. L. Nicolet, C. Hofmann, M. A. Kol'chenko, B. Kozankiewicz, and M. Orrit, *ChemPhysChem* **8**, 1215 (2007).
20. A. A. Gorshelev, A. V. Naumov, I. Yu. Eremchev, Y. G. Vainer, L. Kador, and J. Köhler, *ChemPhysChem* **11**, 182 (2010).
21. W.E. Moerner, T. Plakhotnik, T. Irngartinger, M. Croci, V. Palm, and U. P. Wild, *J. Phys. Chem.* **98**, 7382 (1994).
22. Y. Durand, A. Bloess, J. Köhler, E. J. J. Groenen, and J. Schmidt, *J. Chem. Phys.* **114**, 6843 (2001).
23. A. Kiraz, M. Ehrl, C. Bräuchle, and A. Zumbusch, *J. Chem. Phys.* **118**, 10821 (2003).
24. A. Kiraz, M. Ehrl, C. Hellrieger, C. Bräuchle, and A. Zumbusch, *ChemPhysChem* **6**, 919 (2005).
25. A. Kiraz, M. Ehrl, C. Bräuchle, and A. Zumbusch, *Appl. Phys. Lett.* **85**, 920 (2004).
26. A. Kiraz, M. Ehrl, Th. Hellerer, Ö.E. Müstecaplıođlu, C. Bräuchle, and A. Zumbusch, *Phys. Rev. Lett.* **94**, 223602 (2005).
27. A. Kiraz, M. Ehrl, Th. Hellerer, Ö.E. Müstecaplıođlu, C. Bräuchle, and A. Zumbusch, *JPCS* **36**, 67 (2006).
28. R. Lettow, V. Ahtee, R. Pfab, A. Renn, E. Ikonen, S. Götzinger, and V. Sandoghdar, *Opt. Express* **15**, 15842 (2007).
29. J. B. Trebbia, P. Tamarat, and B. Lounis, *Phys. Rev. A* **82**, 063803 (2010).
30. V. Ahtee, R. Lettow, R. Pfab, A. Renn, E. Ikonen, S. Götzinger, and V. Sandoghdar, *J. Mod. Optic.* **56**, 161 (2009).
31. R. Lettow, Y. L. A. Rezus, A. Renn, G. Zumofen, E. Ikonen, S. Götzinger, and V. Sandoghdar, *Phys. Rev. Lett.* **104**, 123605 (2010).
32. B. Lounis, and M. Orrit, *Rep. Prog. Phys.* **68**, 1129 (2005).
33. J. McKeever, A. Boca, A. D. Boozer, R. Miller, J. R. Buck, A. Kuzmich, and H. J. Kimble, *Science* **303**, 1992 (2004).

34. A. Kuhn, M. Hennrich, and G. Rempe, *Phys. Rev. Lett.* **89**, 067901 (2002).
35. M. Keller, B. Lange, K. Hayasaka, W. Lange, and H. Walther, *Nature* **431**, 1075 (2004).
36. Z. Yuan, B. E. Kardynal, R. M. Stevenson, A. J. Shields, C. J. Lobo, K. Cooper, N. S. Beattie, D. A. Ritchie, and M. Pepper, *Science* **295**, 102 (2002).
37. C. Chen, P. Chu, C. A. Bobisch, D. L. Mills, and W. Ho, *Phys. Rev. Lett.* **105**, 217402 (2010).
38. L. Fleury, B. Sick, G. Zumofen, B. Hecht, and U. P. Wild, *Mol. Phys.* **95**, 1333 (1998).
39. F. Kulzer, F. Koberling, T. Christ, A. Mews, and T. Basché, *Chem. Phys.* **247**, 23 (1999).
40. B. Lounis, and W. E. Moerner, *Nature* **407**, 491 (2000).
41. L. Fleury, J. M. Segura, G. Zumofen, B. Hecht, and U. P. Wild, *Phys. Rev. Lett.* **84**, 1148 (2000).
42. C. Hofmann, A. Nicolet, M. A. Kolchenko, and M. Orrit, *Chem. Phys.* **318**, 1 (2005).
43. A. A. L. Nicolet, P. Bordat, C. Hofmann, M. A. Kol'chenko, B. Kozankiewicz, R. Brown, and M. Orrit, *ChemPhysChem* **8**, 1929 (2007).
44. J. B. Trebbia, H. Ruf, P. Tamarat, and B. Lounis, *Opt. Express* **17**, 23986 (2009).
45. C. Toninelli, Y. Delley, T. Stöferle, A. Renn, S. Götzinger, and V. Sandoghdar, *Appl. Phys. Lett.* **97**, 021107, (2010).
46. Y. Dumeige, F. Treussart, R. Alléaume, T. Gacoin, J.-F. Roch, and P. Grangier, *J. Lumin.* **109**, 61 (2004).
47. T. Gaebel, I. Popa, A. Gruber, M. Domhan, F. Jelezko, and J. Wrachtrup, *New J. Phys.* **6**, 98 (2004).
48. J. H. Hsu, W. D. Su, K. L. Yang, Y. K. Tzeng, H. C. Chang, *Appl. Phys. Lett.* **98**, 193116 (2011).
49. M. De Vittorio, F. Pisanello, L. Martiradonna, A. Quattieri, T. Stomeo, A. Bramati,

- and R. Cingolani, *Opto-Electron. Rev.* **18**, 1 (2010).
50. A. J. Shields, *Nat. Photonics* **1**, 215 (2007).
 51. A. Kiraz, S. Fälth, C. Becher, B. Gayral, W. V. Schoenfeld, P. M. Petroff, Lidong Zhang, E. Hu, and A. Imamoglu, *Phys. Rev. B* **65**, 161303 (2002).
 52. M. Steiner, A. Hartschuh, R. Korlacki, and A. J. Meixner, *Appl. Phys. Lett.* **90**, 183122 (2007).
 53. K. G. Lee, X. W. Chen, H. Eghlidi, P. Kukura, R. Lettow, A. Renn, V. Sandoghdar, and S. Götzinger, *Nat. Photonics* **5**, 166 (2011).
 54. C. Becher, A. Kiraz, P. Michler, W. V. Schoenfeld, P. M. Petroff, L. Zhang, E. Hu, and A. Imamoglu, *Physica E* **13**, 412 (2002).
 55. J. Vuckovic, D. Fattal, C. Santori, G. S. Solomon, and Y. Yamamoto, *Appl. Phys. Lett.* **82**, 3596 (2003).
 56. A. J. Bennett, D. C. Unitt, P. Atkinson, D. A. Ritchie, and A. J. Shields, *Opt. Express* **13**, 50 (2005).
 57. V. B. Verma, M. J. Stevens, K. L. Silverman, N. L. Dias, A. Garg, J. J. Coleman, and R. P. Mirin, *Opt. Express* **19**, 4182 (2011).
 58. C. A. Werley, and W. E. Moerner, *J. Phys. Chem. B* **110**, 18939 (2006).
 59. D. Wöll, H. Uji-i, T. Schnitzler, J. Hotta, P. Dedecker, A. Herrmann, F. C. De Schryver, K. Müllen, and J. Hofkens, *Angew. Chem. Int. Ed.* **47**, 783 (2008).
 60. M. Yorulmaz, A. Kiraz, and A. L. Demirel, *J. Phys. Chem. B* **113**, 9640 (2009).
 61. E. Betzig, G. H. Patterson, R. Sougrat, O. W. Lindwasser, S. Olenych, J. S. Bonifacino, M. W. Davidson, J. Lippincott-Schwartz, and H. F. Hess, *Science* **313**, 1642 (2006).
 62. M. J. Rust, M. Bates, and X. Zhuang, *Nat. Methods* **3**, 793 (2006).
 63. M. Wahl, F. Koberling, M. Patting, H. Rahn, and R. Erdmann, *Curr. Pharm. Biotechnol.* **5**, 299 (2004).
 64. R. A. L. Vallee, M. Van der Auweraer, W. Paul, and K. Binder, *Phys. Rev. Lett.* **97**, 217801 (2006).

65. D. Nettels, I. V. Gopich, A. Hoffmann, and B. Schuler, *Proc. Natl. Acad. Sci. USA* **104**, 2655 (2007).
66. R. J. Pfab, J. Zimmermann, C. Hettich, I. Gerhardt, A. Renn, and V. Sandoghdar, *Chem. Phys. Lett.* **387**, 490 (2004).
67. M. Böhmer, F. Pampaloni, M. Wahl, H.-J. Rahn, R. Erdmann, and J. Enderlein, *Rev. Sci. Instrum.* **72**, 4145 (2001).
68. J. C. Thomas, *Proc. SPIE*, **1430**, 2 (1991).
69. P. Sengupta, K. Garai, J. Balaji, N. Periasamy, and S. Maiti, *Biophys. J.* **84**, 1977 (2003).
70. K. Modos, R. Galantai, I. Bardos-Nagy, M. Wachsmuth, K. Toth, J. Fidy, and J. Langowski, *Eur. Biophys. J.* **33**, 59 (2004).
71. S. A. Sukhishvili, Y. Chen, J. D. Müller, E. Gratton, K. S. Schweizer, and S. Granick, *Macromolecules* **35**, 1776 (2002).
72. H. Zettl, U. Zettl, G. Krausch, J. Enderlein, and M. Ballauff, *Phys. Rev. E* **75**, 061804 (2007).
73. A. Michelman-Ribeiro, H. Boukari, R. Nossal, and F. Horkay, *Macromolecules* **37**, 10212 (2004).
74. A. Best, T. Pakula, and G. Fytas, *Macromolecules* **38**, 4539 (2005).
75. J. Widengren, Ü. Mets, and R. Rigler, *J. Phys. Chem.* **99**, 13368 (1995).
76. T. Wohland, R. Rigler, and H. Vogel, *Biophys. J.* **80**, 2987 (2001).
77. M. J. Culbertson, and D. L. Burden, *Rev. Sci. Instrum.* **78**, 044102 (2007).
78. M. Wahl, I. Gregor, M. Patting, and J. Enderlein, *Opt. Lett.* **11**, 3583 (2003).
79. D. Magatti, and F. Ferri, *Appl. Opt.* **40**, 4011 (2001).
80. K. Schätzel, M. Drewel, and S. Stimac, *J. Mod. Opt.* **35**, 711 (1988).
81. K. Schätzel, and R. Peters, *Proc. SPIE*, **1430**, 109 (1991).
82. P.-O. Gendron, F. Avaltroni, and K. J. Wilkinson, *J. Fluoresc.* **18**,:1093 (2008).
83. H. Zettl, W. Häfner, A. Böker, H. Schmalz, M. Lanzendörfer, A. H. E. Müller, and G. Krausch, *Macromolecules* **37**, 1917 (2004).

84. R. Liu, X. Gao, J. Adams, and W. Oppermann, *Macromolecules* **38**, 8845 (2005).
85. J. Jasny, J. S. T. Irngartinger, M. Traber, A. Renn, and U. P. Wild, *Rev. Sci. Instrum.* **67**, 1425 (1996).
86. Sigma Aldrich online catalog.
87. F. Treussart, A. Clouqueur, C. Grossman, and J.-F. Roch, *Opt. Lett.* **26**, 1504 (2001).
88. M. Pärs, V. Palm, M. Rähn, N. Palm, and J. Kikas, *J. Lumin.* **128**, 838 (2008).
89. C. Toninelli, K. Early, J. Breimi, A. Renn, S. Götzinger, and V. Sandoghdar, *Opt. Express* **18**, 6577 (2010).
90. M. A. Kol'chenko, B. Kozankiewicz, A. Nicolet, and M. Orrit, *Opt. Spectrosc.* **98**, 681 (2005).
91. A. Nicolet, M. A. Kol'chenko, B. Kozankiewicz, and M. Orrit, *J. Chem. Phys.* **124**, 164711 (2006).
92. E. ten Grotenhuis, J. C. van Miltenburg, and J. P. van der Eerden, *Chem. Phys. Lett.* **261**, 558 (1996).
93. G. S. Harms, T. Irngartinger, D. Reiss, A. Renn, and U. P. Wild, *Chem. Phys. Lett.* **313**, 533 (1999).
94. J. T. Fourkas, *Opt. Lett.* **26**, 211 (2001).
95. R. Camacho, D. Thomsson, D. Yadav, and I. G. Scheblykin, *Chem. Phys.* (2012), <http://dx.doi.org/10.1016/j.chemphys.2012.03.001>.
96. P. Zhang, J. Deng, X. Zeng, Z. Liu, Y. Qiu, H. Zhong, Y. Fan, J. Huang, J. Zhang, and K. Xu, *J. Cryst. Growth* **311**, 4708 (2009).
97. S. Jo, H. Yoshikawa, A. Fujii, and M. Takenaga, *Appl. Surf. Sci.* **252**, 3514 (2006).
98. A. Molski, *J. Chem Phys.* **114**, 1142 (2001).
99. C. Jung, B. K. Müller, D. C. Lamb, F. Nolde, K. Müllen, and C. Bräuchle, *J. Am. Chem. Soc.* **128**, 5283 (2006).
100. M. K. Cheezum, W. F. Walker, and W. H. Guilford, *Biophys. J.* **81**, 2378 (2001).
101. R. E. Thompson, D. R. Larson, and W. W. Webb, *Biophys. J.* **82**, 2775 (2002).

102. S. M. Anthony, and S. Granick, *Langmuir* **25**, 8152 (2009).
103. R. J. Ober, S. Ram, and E. S. Ward, *Biophys. J.* **86**, 1185 (2004).
104. C. S. Smith, N. Joseph, B. Rieger, and K. A. Lidke, *Nat. Methods.* **7**, 373 (2010).
105. A. V. Abraham, S. Ram, J. Chao, E. S. Ward, and R. J. Ober, *Opt. Express.* **17**, 23352 (2009).
106. A. V. Abraham, S. Ram, J. Chao, E. S. Ward, and R. J. Ober, *Proc. SPIE*, **7570**, 757004 (2010).
107. S. M. Kay, *Fundamentals of Statistical Signal Processing, Volume 1: Estimation Theory*, chapter 7, Prentice Hall, 1993, Maximum Likelihood Estimation.
108. T. Kailath, A. H. Sayed, and B. Hassibi, *Linear Estimation*, chapter 9, Prentice Hall, 2000, The Kalman Filter.
109. EM-CCD Technical Note, Hamamatsu Photonics K. K., Systems Division (2009).
110. P. H. Wu, A. Agarwal, H. Hess, P. P. Khargonekar, and Y. Tseng, *Biophys. J.* **98**, 2822 (2010).
111. G. Hungerford, and D. J. S. Birch, *Meas. Sci. Technol.* **7**, 121 (1996).
112. K. Ng Kwok, *Complete Guide to Semiconductor Devices*, chapter 53, McGraw-Hill, 1995, Avalanche Photodiode (APD).
113. W. Becker, *Advanced Time-Correlated Single Photon Counting Techniques*, chapter 6, Springer, 2005, Detectors for Photon Counting.
114. H. Dautet, P. Deschamps, B. Dion, A. D. MacGregor, D. MacSween, R. J. McIntyre, C. Trottier, and P. P. Webb, *Appl. Opt.* **32**, 3894 (1993).

VITA

Mehdi Yavuz Yüce was born in 1980 in Istanbul Turkey. He received his B.S. degrees in Mechanical Engineering and in Physics, and his M.S. degree in Materials Science and Engineering from Koç University in 2004 and 2006 respectively. He worked as research assistant in Konstanz University, Germany from 2006 to 2008. He has been a doctoral student in Koç University Physics Department since 2009.

Journal Articles:

- M. Y. Yüce, A. Kiraz, "Single-Molecule Fluorescence of Terrylene Embedded in Anthracene Matrix: A Room Temperature Study", Chem. Phys. Lett., accepted.
- M. Y. Yüce, A. T. Erdoğan, A. Jonas, A. Kiraz, "Video-Based Tracking of Single Molecules Exhibiting Directed In-frame Motion", Microsc. Microanal., Vol. 18 (04), pp. 781-792 (2012).
- M. Y. Yüce, A. T. Erdoğan, A. Kiraz, "Velocity Estimation of Mobile Single Molecules for Improved Position Accuracy", OMN2011: 16th International Conference on Optical MEMS and Nanophotonics, pp. 225-226 (2011).
- Y. Karadağ, M. Gündoğan, M. Y. Yüce, H. Çankaya, A. Sennaroğlu, A. Kiraz, "Prolonged Raman Lasing in Size-Stabilized Salt-Water Microdroplets on a Superhydrophobic Surface", Opt. Lett., Vol. 35 (12), pp. 1995-1997 (2010).
- M. Y. Yüce, A. L. Demirel, "The Effect of Nanoparticles on the Surface Hydrophobicity of Polystyrene", Eur. Phys. J. B, Vol. 64 (3-4), pp. 493-497 (2008).
- A. Kiraz, A. Kurt, M. A. Dündar, M. Y. Yüce, A. L. Demirel, "Volume Stabilization of Single, Dye-doped Water Microdroplets with Femtoliter Resolution", J. Opt. Soc. Am. B, Vol. 24 (8), pp. 1824-1828 (2007).
- M. Y. Yüce, A. L. Demirel, F. Menzel, "Tuning the Surface Hydrophobicity of Polymer/Nanoparticle Composite Films in the Wenzel Regime by Composition", Langmuir, Vol. 21 (11), pp. 5073-5078 (2005).